SYNTHESIS, CHARACTERIZATION, OPTIMIZATION, AND ELECTROCHEMICAL ANALYSIS OF NOVEL MULTIMETAL OXIDE MATERIALS FOR ENERGY APPLICATIONS

A Thesis Submitted to
The Graduate School of
İzmir Institute of Technology
in Partial Fulfillment of the Requirements for the Degree of

DOCTOR OF PHILOSOPHY

in Chemistry

by
Ahmet AYTEKİN

July 2024
IZMIR

We approve the thesis of **Ahmet AYTEKİN**

Examining Committee Membres:

Prof. Dr. Sinan BALCI
Department of Photonics, Izmir Institue of Technology

Assoc. Dr. Ümit Hakan YILDIZ
Department of Chemistry, Izmir Institue of Technology

Prof. Dr. Fatma Nil ERTAŞ
Department of Chemistry, Ege University

Prof. Dr. Kadriye ERTEKİN
Department of Chemistry, Dokuz Eylül University

12.07.2024

Assoc. Dr. Engin KARABUDAK
Supervisor, Department of Chemistry, Izmir Institue of Technology

Prof. Dr. Gülşah ŞANLI MOHAMED
Head of the Department of Chemistry

Prof. Dr. Mehtap EANES
Dean of the Graduate School

LIST OF ABBREVIATIONS

AFC	:	Alkaline Fuel Cell
Ah	:	Amperhour
AI	:	Artifical Intelligence
CC/CV	:	Constant Current/Constant Voltage
CV	:	Cyclic Voltammetry
DMFC	:	Direct Methanol Fuel Cell
E_F	:	Fermi level energy
Eg	:	Band gap energy
FTO	:	Fluorine-doped Tin Oxide
GO	:	Graphene oxide
HOR	:	Hydrogen Oxidation Reaction
HTE	:	High-throughput experimentation
Li-MnO_2	:	Lithium manganese dioxide battery
$LiPF_6$	:	Lithium hexafluorophosphate
mA	:	miliamper
MCFC	:	Molten Carbonate Fuel Cell
$Ni(OH)_2$	:	Nickel hydroxide
Ni-Cd	:	Nickel Cadmium battery
Ni-MH	:	Nickel metal hydride
nm	:	nanometer
OER	:	Oxygen Evolution Reaction
ORR	:	Oxygen Reduction Reaction
PAFC	:	Phosphoric Acid Fuel Cell
PC	:	Polycrystal
PEMFC	:	Proton Exchanges Membrane Fuel Cell
SC	:	Single crystal
SDL	:	Self-driving laboratory
SEM	:	Scanning Electron Microscopy
SOC	:	State of charge
SOFC	:	Solid Oxide Fuel Cell
TCO	:	Transparent conducting oxide
TMO	:	Transition metal oxide
TW	:	Terawatt
Wh	:	Watthour
XPS	:	X-ray photoelectron spectroscopy
XRD	:	X-Ray Diffraction
λ	:	Wavelength
μm	:	micrometer

ACKNOWLEDGMENTS

Firstly, I would like heartily to thank my supervisor, Assoc. Dr. Engin Karabudak, for his patient guidance, encouragement, and mentoring.

I want to give special thanks to Prof. Dr. Sinan Balcı, Assoc. Prof. Ümit Hakan Yıldız, Prof. Dr. Fatma Nil Ertaş, and Prof. Dr. Kadriye Ertekin attending as committee members reviewing my work.

Also, I would like to thank Dr. Emre Yusuf Göl, Turgut Uğur, Koray Aydın, Yağmur Çördük, and Vahide Sertbaş, as members of the Karabudak research group.

I endlessly thank all members of my family (my mother, father, sisters, and brothers) for their love and support throughout my entire life.

ABSTRACT

SYNTHESIS, CHARACTERIZATION, OPTIMIZATION, AND ELECTROCHEMICAL ANALYSIS OF NOVEL MULTIMETAL OXIDE MATERIALS FOR ENERGY APPLICATIONS

Recently, researchers have focused on multimetal oxide materials to meet energy requirements and to improve their properties, such as electrochemical and areas of usage. Multimetal oxide materials are widely used in batteries such as Li-ion and Ni-MH, in semiconductors, in water splitting studies, in fuel cells, and in catalyst studies.

In this study, nickel hydroxide (alpha and beta form) was synthesized by using urea decomposition method. Co, Zn, Al, and Cu-doped $Ni(OH)_2$ were also synthesized via same method. Here, optimization and cell (battery) studies were done to improve the nikel hydroxide capacity. C rate, binder effect, and electrolytic effect were discussed as well.

In the study, BSCF, Ag-doped BSCF, and novel BSNF materials were synthesized by utilizing sol-gel method. Also, to determine their perovskite class, Goldschmidt tolerance factors were first calculated for BSCF, Ag-BSCF, and BSNF. It was found that, according to the Goldschmidt factor, all these materials were in the perovskite class.

In the thesis, Cr, Co, Fe, Mn, and Ni nitrate salts were used to prepare printable inks. All printable inks were also optimized to print on a substrate. By using the printable inks, multimetal oxide materials were fabricated on the FTO glass, which offers hydrogen and oxygen from water.

Last, $PbVO_3CI$ material was synthesized and characterized. We discussed various properties, such as semiconductor, electronic structure, dynamic stability (Born-phonon criteria), and perovskite class. The materials we discussed in the thesis, especially Ag-BSCF, BSNF, and $PbVO_3CI$ can be promising in solar cells, SOFCs, batteries, semiconductors, and electrocatalytic studies.

ÖZET

ENERJİ UYGULAMALARI İÇİN YENİ MULTİMETAL OKSİT MALZEMELERİN SENTEZİ, KARAKTERİZASYONU, OPTİMİZASYONU VE ELEKTROKİMYASAL ANALİZİ

Son zamanlarda, enerji ve enerjiye olan ihtiyaç gittikçe artmaktadır. Bu enerji ihtayacını karşılamak adına, araştırmacılar enerji ile ilintili malzemelerin elektrokimyasal özelliklerini ve kullanım alanlarını iyileştirmek için çalışmaktadırlar. Günümüzde, multimetal oksit malzemeler bataryada (lityum iyon batarya ve Ni tabanlı batarya), yarı iletkenlerde, suyu ayrıştırma çalışmalarında, yakıt hücrelerinde ve kataliz çalışmalarında geniş bir şekilde kullanılmaktadır.

Bu tezde nikel hidroksit (alfa ve beta formu), üre parçalanması metoduyla sentezlenmiştir. Kobalt, çinko, alüminyum ve bakır katkılı $Ni(OH)_2$ aynı metotla sentezlenmiştir. Bu katkılı nikel hidroksitlerin elektrokimyasal analizi yapılmış ve karakterize edilmiştir. Nikel hidroksit kapasitesini iyileştirmek için küçük bir hücre çalışması yapılmış ve optimizasyon çalışması yapılarak bazı etkiler (c rate, tutkal etkisi ve elektrolit etki) incelenmiştir. Ayrıca NMC katot malzemesi katı-hal yöntemi ile sentezlenmiş ve kapasite çalışması yapılmıştır.

Çalışmada BSCF, Ag-BSCF ve yeni BSNF malzemeleri sol jel yöntemi ile sentezlenmiş ve karakterize edilmiştir. Ayrıca, perovskite sınıfında olup olmadıklarını belirlemek adına Goldschmidt tolerans faktörleri hesaplanmış ve tartışılmıştır.

Tezde çeşitli metal tuzları (Cr, Co, Fe, Mn, Ni) kullanılarak basılabilir mürekkep hazırlanmıştır. Hazırlanmış olan basılabilir mürekkeplerin optimizasyon çalışması yapılmıştır. Bu mürekkeplerden yola çıkarak multimetal oksit katalizörleri sentezlenmiştir, bu da suyu ayrıştırarak hidrojen ve oksijen elde etme imkanı sunar.

Son olarak, $PbVO_3CI$ malzemesi sentezlenmiş ve karakterize edilmiştir. Yarı iletkenliği, elektronik yapısı, dinamik kararlılığı (Born-Phonon) ve perovskite sınıfı özelliği ele alınmıştır. Tezde, irdelenen bu malzemeler (özellikle Ag-BSCF, BSNF, $PbVO_3CI$) solar hücrelerde, katı hal yakıt hücrelerinde (SOFC), bataryalarda, yarı iletken ve katalizör çalışmalarında kullanılabilme potansiyeline sahiptir.

LIST OF CONTENTS

LIST OF FIGURES

Figures **Page**

Figures **Page**

Figures **Page**

Figures **Page**

Figures **Page**

LIST OF TABLES

Tables **Page**

CHAPTER 1

INTRODUCTION

1.1. Energy

Energy and energy related materials play essential role in human being life. Every single living organism need energy to survive on earth. Energy word, originally energeia, come from Greek language. Aristotle was first time to mention energy word in Nicomachean Ethics in the 4th century-BC (Joachim and Rees 1952, Reeve 1992).

Providing the sufficiency and sustainability of products is a main problem that must be solved in the time to come. Fossil fuels such as coal, petroleum and natural gas meet world of rougly %80 energy requirments. But such fuels, unfortunally, has a certain limit. Therefore it is requare to decrease the addiction of the fossil fuels. Nowadays, renewable sources, for example wind, solar, hydroelectric, biomass, and geothermal energy, become important day by day (Wang et al., 2013).

Today, the world face the worst impacts of climate change; high atmospheric carbondioxide (CO2) level, high temperature level, deforestation, the incerease of methane (CH4) and nitrous oxide (N2O), and the decrease of pH level in sea and ocean. It is possible face to face this bad scenario as long as the human population increase, and we contuniu to use the fossil fuel. It is expected that the demand of globe energy will be more than double from 13 TW to 28 TW at the middle of this century (Ginley and Cahen, 2011).

In 1859, Jonh Tyndall, an Irish scientist, began working on certain gases such as water vapor, carbon dioxide, ozone, and noticed that these gases absorb and re-emit heat, also investigated the role of water vapor on the globe surface temperature. In 1896, Svante Arrhenius, Swedish scientist realised that the usage of fuels caused greenhouse gas (GHG) emissions, and so would warm the earth. Guy Callendar, an British engineer, examined the measurements of carbon dioxide concentration between the years 1866 1956. He found that there was relationship between carbon dioxide concentration level and use of fossil fuels (Ginley and Cahen, 2011).

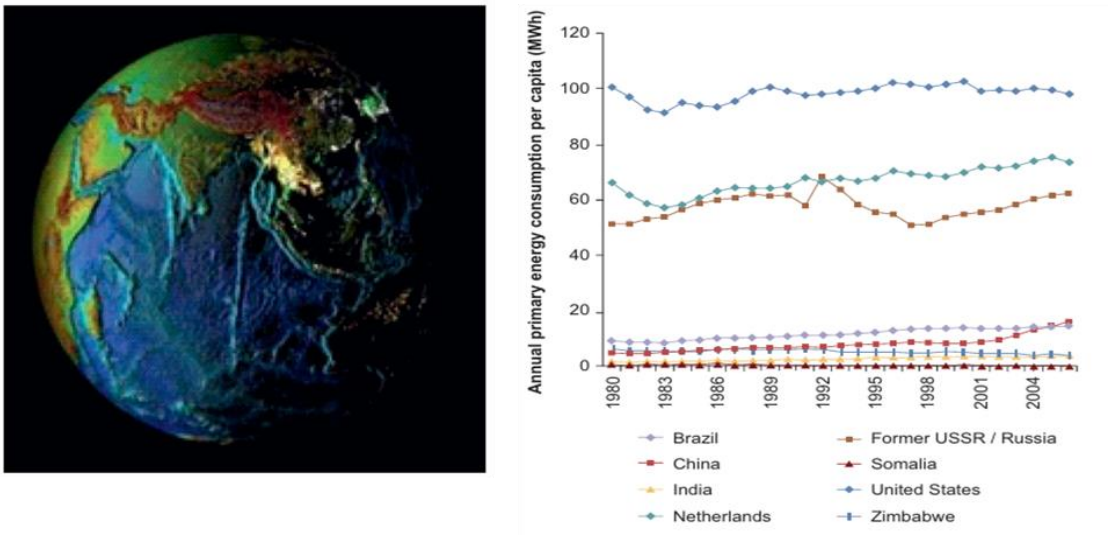

Figure 1. 1. Living blue globe (left image) and energy consumption (right image, between 1980 and 2006) (Ginley and Cahen, 2011).

1.2. Global Energy Landscape

A country's economic output and people's well-being directly affect the energy consumption of the country. As the world population and individual's standard living is increasing, naturally, the energy consumption will get more and more growth, and this show the society develop of a country. For instance, in 1800, before the full strating of the Industrial Revolution, the population of people lived on the earth was 1 billion, and the total annual energy consumption was 0.6 TW years. However, today, the world has about 8-9 billion people, with a total annual energy consumption of 14 TW years.

Growth in energy not only effect the population increase but also agricultural improvements, transportation networks, manufacturing increase, indivindual prosperity. Recently, cell phones, PC (computers), and video-conferencing devices have been symbols of significant tranformations. Despite improvements in energy efficiency, the manufacture and use of such lifestyle-enhancing equipments cause more energy consumption. However, good living standard and growth energy consumption have been not fairly shared among countries. (Ginley and Cahen, 2011). As shown in Figure 1.1 (right image).

CHAPTER 2

2.1. History of Battery

A battery is a tool that provides chemical energy, primarily based on reduction-oxidation reactions, to be converted into electricity. The scale of energy in a battery is able to vary from nonawatt hour to megawatt hour. The past of batteries is dated back to around 1790s, when "animal electricity" was discovered. There is some idea that the electrochemical battery was appeared with the discovery of so-called "Baghad Battery" in first century BC, but it is generally accepted that the studies of Luigi Galvani and Alessandro Volta, both of them italian scientists, started the modern electrochemistry battery at present time. The history of batteries is summarized in Table 2.1. (Wu, 2015; Root, 2011; Linden, 2002).

Table 2. 1. The past of batteries (Wu, 2015, *some sentences were shortened*)

Time	Events
1790	Luigi Galvani, the discover of "the animal electricity"
1800	Alessandro Volta, the first battery made from the discs of zinc and copper
1821	W.T Brande and Sir. H. Davy, by using lithium oxide, isolated lithium metal
1836	J.F. Daniell, British chemist, the Daniell cell, which made of a copper pot illed with a copper sulfate solution
1859	G. Planté; the Pb(lead)-acid battery.
1866	G. Leclanché, "dry battery" which contained zinc as negative electrode and a manganese dioxide as positive electrode in the ammonium chloride solution.
1887	Desmazures, Dun, and Hasslacher: studied on the possibility of using NiO in alkalin battery.
1890	Jungner and de Michalowski: investigated the preparation of NiOOH.
1899	W. Jungner, Sweden: the first Ni//Cd battery.
1901	W. Jungner and T. Edison: obtained patents for Cd-NiOOH and Fe-NiOOH rechargeable batteries
1942	HgO/KOH/Zn, Mercury battery
1970	Calcium MF Storage Battery, (USA) made commercial the lithium primary battery.
1976	Li//TiS_2 (Lithium-Titanium Sulfur) rechargeable battery, by M.S. Whittingham et al.
1980	R. Yazami: intercalation of lithium- graphite, J. Goodenough, $LiCoO_2$ positive active material, B. Scrosati; Rock-type lithium ion battery
1990	Sony and MoLi company: the lithium-ion battery.
1994	J.R. Dahn et al.: aqueous rechargeable lithium battery
1996	K.M. Abraham et al.: nonaqueous Li/air battery
1997	J. Goodenough: $LiFePO_4$ as a positive electrode
2009	H.S. Zhou et al.: studied on hybrid electrolytes for Li//$Ni(OH)_2$
2010	T. Zhang et al. Li-air battery
2012	Y.P.Wu. et al. High density equeous lithium ion battey
2013	Y.P.Wu. et al. Rechargable Li-Br_2 battery

2.2. Batteries Science and Their Fundamental Concepts

Here, battery active components, electrochemical cell potentials, electrochemical kinetics and the theoretical capacity of the battery will be shortly discussed and identified.

2.2.1. Battery Active Components

Three fundamental battery active components are anode, cathode, and electrolyte. These three components are required to perform a functional battery or a cell. All cells and batteries have the same function properties; converting chemical energy into electricity energy.

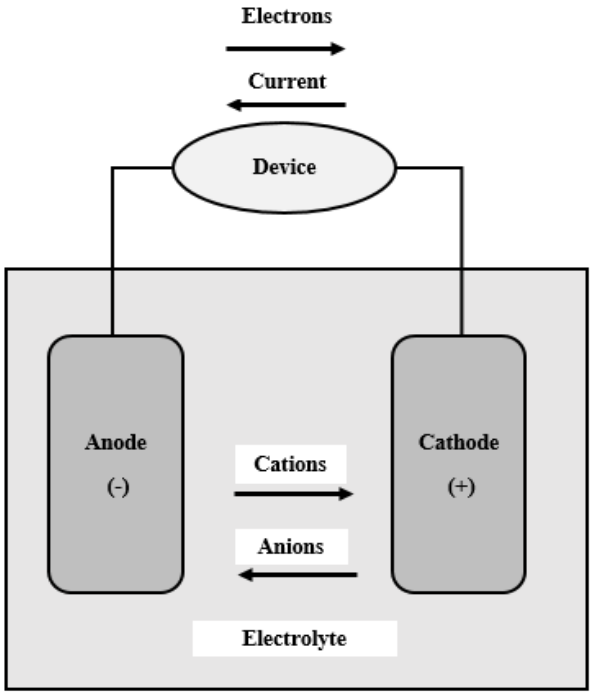

Figure 2.1. The Components of a Cell or Battery.

The general components of a cell are shown in Figure 2.1. While the anode (the negative side) releases electrons to the external device circuit, the anode (the positive side) gains electrons to the external device circuit. The electrolyte is a solution medium consisting of the mobile positive and negative ions. The ions in the electrolye solution have a function to complete the electrical circuit (Root, 2011).

2.2.2. Electrochemical Kinetic

A cell potential is the probability of an electrochemical reaction progressing spontaneously. There are a large number of factors that limit how fast an electrochemical reaction can develop. When the circuit powered by a battery turn on, a current starts to flow, and many complex steps simultaneously occur. The reactions that occur at the anode and cathode are forced away from equilibrium by a net charge transfer of electrons and ions at the electrode (Root, 2011).

When the Daniell cell (Zin-Cu) is considered at the equilibrium, net current is not occuring, and the half-cell reactions are also at equilibrium. For the copper electrode;

Cathodic reaction;

$$Cu_{(aq)} + 2e^- \rightarrow Cu \tag{2.1}$$

Equals anodic reaction;

$$Cu \rightarrow Cu_{(aq)} + 2e^- \tag{2.2}$$

The rate of electrochemical reactions are calculated by measuring current, because electrons generated or comsumed. So, at equilibrium, the anodic current is same as cathodic current

$$i_c - i_a = 0 \tag{2.3}$$

The magnitude of the cathodic current and anodic current can be called as i_0 ,the exchange current, so it can be written as;

$$i_c = i_a = i_0 \tag{2.4}$$

The exchange current depends upon the reaction kinetics of electrode involved, therefore the different exchange currents occur at different rates at which the different chemical reactions react. When the current is generated at the circuit, the anodic and cathodic currents are not equal. The kinetics of electrochemical reactions developing at each electrode are well expressed by the Butler-Volmer equation; (Root, 2011; and Dickinson and Wain, 2020).

$$i = i_0 \left\{ \exp\left[-\frac{\alpha F}{RT}(E - E^0) \right] - \exp\left[\frac{(1-\alpha)F}{RT}(E - E^0) \right] \right\} \quad (2.5)$$

Where, *R, T, E, E^0*, and α indicate the gas constant, temperature (kelvin), the electrode potential, the standard electrode potential, and the constant characteristic of the electrochemical reaction varying from 0 to 1, respectively. If the α value is unknown, it can be accepted as 0.5. The net current i is a fuction of the different between standard electrode potential and the electrode potential. As showen in the Figure 2.2.

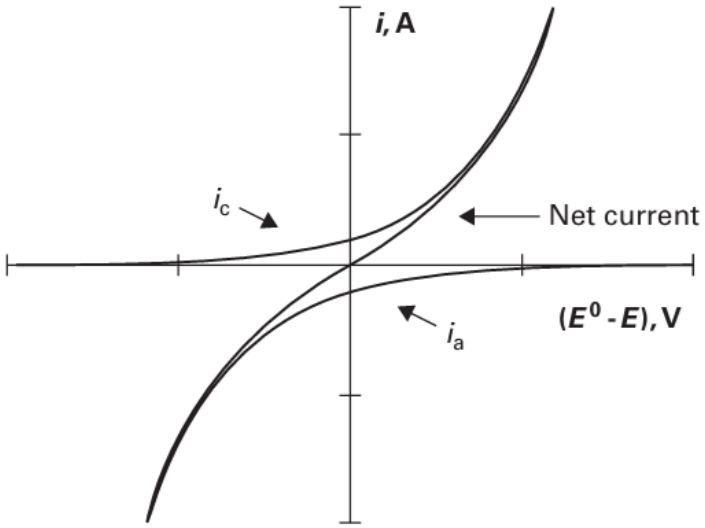

Figure 2.2. The slope of the Bulter-Volmer equation (i against E-E^0)
(Root, 2011)

The Bulter-Volmer equation is widely used in various fields, such as hydrogen/oxygen electrocatalytic processes (polymer electrolyte membrane fuel cell (PEMFC) and SOFC), voltammetric systems (catalytic phenomena), and energy storage device reactions (vanadium redox-flow battery and zinc-bromine) (Dickinson and Wain, 2020).

2.2.3. Electrochemical Cell Potential

The total reaction in the electrochemical cell can be expressed with two half-cell reactions; first the anode reaction, and second the cathode reaction. The metal and metal ions in the solution can be at equilibrium when no current moves between the two electrodes. This potential is called the equilibrium potential, or the open circuit potential in battery terms. For instance, copper (Cu) and zinc (Zn) half-cell reactions can be written like the following; (Root, 2011).

$$Cu^{2+}_{(aq)} + 2e^- \leftrightarrows Cu \text{ (reduction reaction)} \quad (2.6)$$

$$Zn \leftrightarrows Zn^{2+}_{(aq)} + 2e^- \text{ (oxidation reaction)} \quad (2.7)$$

An electrical potential difference along the cell electrodes can be measured. J. W. Gibbs, a chemist and physicist at the University of Yale, was the first to suggest thermodynamic relationships to chemical reactions. Energy, or work, in the electrochemical cell, can be defined in thermodynamic terms as the change in Gibbs free energy, shortened ΔG. The ΔG (J/mol) value state the measure of total chemical energy that is converted into electrical energy. The equation of Gibbs energy is given the following; (Root, 2011).

$$\Delta G = -nFE \quad (2.8)$$

In this equaiton, n is the number of electrons involved in the electrochemical energy, F is the Faraday constant, and E represents the cell potential. The ΔG value measure the tendency of electrochemical reaction to develop spontaneously. When the Δ*G* is lower than zero (0), the energy generated by the electrochemical reaction will be much more. To make an efficient battery, the chemical materials must properly be matched for spontaneous electrochemical reactions to develop. The ΔG value can be written according to the standard condition and the non-standard condition. (Root, 2011).

In the standard condition;

$$\Delta G^{\,0} = -nFE^0 \quad (2.9)$$

In the non-standard condition, the Nernst equation derived by using Gibbs formulas can be used here, because the concentration of the soluble ions becomes an important factor. So, it can be written down the Nernst equation for non-standard condition;

$$E = E^0 - \frac{RT}{nF}\ln(\frac{prodcuts\ concentration}{reactants\ concentration}) \quad (2.10)$$

Here, the terms such as E, E^0, R, T, n, and F were expressed before.

2.2.4. Capacity

The amount of the loading active materials in a battery is related to the capacity of the battery expressed as the total charging, or discharging. The capacity of verious active materials used in the battery can be calculated by performing Faraday's Law.

$$Q = nFM \quad (2.11)$$

Where, Q, n, F, and M state the capacity of active material, electrons involved in the reaction, Faraday constant, and the mol numbers of active material, respectively. This is only the theoritical capacity value, but there are verious factors reducing the capacity of the active materials. The quantity of electricity produced by a battery is related with its capacity, measured in unit of ampere-hours (Ah). The formula of a battery capacity can be written (Root, 2011).

Capacity (Ah)= current(A) x time (h) (2.12)

The capacity is measured by integrating the current produced by a battery. In matematical terms, it is expressed;

$$\text{capacity (Ah)} = \int_0^t i\,dt \quad (2.13)$$

When it is consideredn the Ohm's Law as

$$i=E/R \tag{2.14}$$

it can be again expressed here as;

$$\text{capacity (Ah)} = \frac{1}{R}\int_0^t E dt \tag{2.15}$$

So, this expression is indicated in the graphical form in Figure 2.3.

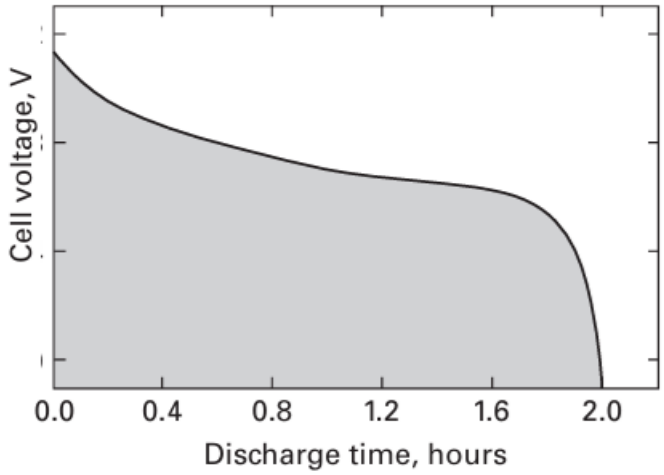

Figure 2. 3. The capacity of a battery.

The capacity of a battery can be graphically determined by gauging the field under a graph of discharge voltage against time (Root, 2011).

2.3. Batteries

Electricity plays a significant role in our daily life. “Life is all but impossible without it”. A battery or electrochemical cell is a device that converts electrochemical energy into electrical energy and stores energy. All chemical energy in the active battery materials depends on the reduction and oxidation reactions (Kiehne, 2003, Dell and Rand, 2001). In general, a battery can be classified into primary cells and secondary cells. The primary cell has the property of only one-time chargeable and disposable, while the secondary cell has more one time charge and discharge, that is, rechargeable. Zinc-carbon, alkaline, and zinc-silver are examples of the primary cells. For the secondary cells, it can be given the examples of lead-acid, nickel cadmium, nickel metal hidrür, and lithium ion battery (Winter and Brodd, 2004; and Kiehne, 2003).

2.3.1. Secondary Batteries

Ever since the introduction of the second batteries, it has passed approxemitaly 150 years. In 1859, Plante developed the lead acid battery. After, the nickel-iron battery was launched by Edisson in 1909. Nevertheless, this battery step by step lose its significant due to expensive and low specific energy. Nowadays, the lithium ion battery has altered the rechargeable battery market because of its high density and high specific energy. The nickel-metal hydride has also dominated the battery market (Shukla et al., 2001, Shen et al., 2018).

Secondary batteries such as silver-zinc, nickel-zinc, nickel hydrogen, and lithium ion batteries have recorded important developments in the battery market during the past few decades. The rechargeable nickel-cadmium (Ni-Cd) cell provides the gravimetric and volumetric density of 35 Wh/kg and 100 Wh /L, respectively. The rechargeable nickel-metal hydride (Ni-MH) battery indicate the gravimetric of 100 Wh/kg and the volumetric value of 430 Wh/L.

As for the lithium-ion battery, especially the advanced lithium-ion battery, can approximately reach between 200-240 Wh/kg as the gravimetric energy density and between 570-640 Wh/L as the volumetric energy density (Shukla et al., 2001, Shen et al., 2018).

2.3.1.1. Nickel-Hydrogen Battery

This battery system use hydrogen (H_2) as negative electrode and the NiOOH material as the active cathode. The system has especially been improved for aerospace applications. The overall reaction of Ni-H_2 cell is shown below;

$$1/2H_2 + NiOOH \rightarrow Ni(OH)_2 \quad (2.16)$$

This system has a better resistance to overcharge and reversal. During charging, oxygen is produced at the nickel electrode, then the oxygen creates water by reacting with hydrogen. On discharge, hydrogen is relased at the positive electrode (+) and used up at negative (-) electrode at the identical rate. Therefore, an increase in pressure and a change in the electrolyte concentration are not occurred.

The Ni-H_2 cell is composed of the components that hydrogen (H_2) formed of a Pt plate supported on a nickel substrate as an anode, potassium hydroxide solution as an electrolyte, and nickel powder as a cathode material are included. Here, porous zirconium oxide (ZrO2) ceramic is utilized as the membrane in this cell system (Shen et al., 2018).

2.3.1.2. Nickel-Zinc Battery

Nickel oxyhydroixde (NiOOH) as a positive cathode material and Zn (ZnO_2) powder or metal as a negative electrode are utilized in the nickel-zinc battery. In addition to this, potassium hydroxide (KOH) is used as an electrolyte in this cell system (Pistoia, 2008).

General reaction mechanism of the Ni-Zn cell is;

$$2NiOOH + 2H_2O + Zn \rightarrow Zn(OH)_2 + 2Ni(OH)_2 \quad (2.17)$$

Compared to the Ni-Cd battery, the Ni-Zn battery has higher energy density due to Zn's high specific energy density. What's more, the Zn material has some advantages in terms of low cost, good cycle life, and good rate stability. However, there are some issues related to the Zn anode such as the dendrite growth and solubility in the high-concentration KOH solution.

Calcium hydroxide as an additive agent, including even some other additives, can be used to alleviate the formation of dendrite on the Zn anode. In this cell system, a microporous polypropylene membrane is utilized, since this membrane exhibits a high stability in the alkaline medium (Linden, 2002, Pistoia 2008).

2.3.1.3 Nickel Cadmium Battery

A nickel-cadmium (Ni-Cd) battery is a secondary cell utilizing nickel oxy-hydroxide as the active cathode material and metal Cd as the anode. The Ni-Cd battery is chemistry well-understood and rather developed system, because it is known as the oldest rechargeable battery. This battery, with low energy density, is used when it comes into prominence with long life, cheap, and high-speed discharge. The aqueous potassium hydroxide (KOH) solution involving some lithium hydroxide (LiOH) and another metal hydroxide salt is used as the electrolyte in this battery system. There are various Ni-based batteries such as Ni-Cd, Ni-MH, Ni-H_2, Ni-Zn, and Ni-Fe (Pistoia, 2008). These batteries are already utilized in various areas such as biomedical devices, video camera, and electrical hand tools. One of the most significant disadvantages of The Ni-Cd battery is that it involves Cd metal which is harmful, toxic, and hazardous.

The Ni-Cd battery has relatively some advantages when compered to other secondary batteries. Because of thier properties such as safe, high-speed charge durability, and low temperature (-15^{o}C) run, Ni-Cd batteries are still used as wireless power sources. The memory effect, self-discharge, and low energy density are significant factors limiting the Ni-Cd batteries when the other secondary batteries are considered. The Ni-Cd cell provides 1.3 V (Pistoia, 2008, Shen et al., 2018, and Root, 2011).

The related reaction of the Ni-Cd battery is indicated below;

Anode reaction; $Cd(s) + 2OH^-(aq) \leftrightarrows Cd(OH)_2 + 2e^-$ (2.18)

Cathodereaction; $2NiOOH(s)+2H_2O(l)+2e^- \leftrightarrows 2Ni(OH)_2(s)+2OH^-$ (2.19)

The overall reaction; $Cd(s)+2NiOOH(s)+2H_2O(l)+2e^- \leftrightarrows 2Cd(OH)_2 + 2Ni(OH)_2(s)$ (2.26)

2.3.1.4. Nickel Metal Hydride Battery

Scientists first worked on the nickel metal hydride cell (Ni-MH) in the 1960s, and this battery replaced the Ni-Cd and the Ni-H_2 batteries. The Ni-MH battery exhibits advantages related to cheaper, higher volumetric energy density, and lower pressure compared to the Ni-Cd cell. While the Ni-MH cell shows a capacity of 2.7 Ah, the Ni-Cd cell provides approximately a capacity of 2.0 Ah. In recent times, the Ni-MH battery has found common use areas such as personal computers and other electronic tools, including hybrid vehicles. The Ni-MH battery is commonly accepted as eco-friendly since the used metals in this battery are not harmful to the environment (Zimmerman, 2009, and Shen et al., 2018). A Ni-MH battery is shown in Figure 2.4.

A hydrogen-alloy, beta-NiOOH, and KOH solution are important components used in the Ni-MH, and represent the anode, the active cathode material, and the electrolyte, respectively. In contrast to Ni-Cd batteries, the Ni-MH cell doesn't contain reactions involving H_2O on the electrode. Thus, the concentration and the conductivity of the electrolyte stay constant during charge and discharge. During charge and discharge, oxygen and hydrogen are involved at the positive, respectively. Then, these gases diffuse to the negative, reacting with MH, to form H_2O. In the Ni-MH cell, the positive and negative material should be used in the ratio of 2:1, respectively (Shen et al., 2018).

The overal reaction of Ni-MH battery is shown below;

$$MH + NiOOH \rightarrow Ni(OH)_2 + M \tag{2.20}$$

There are two types of alloy materials used as the negative electrode (anode) in the Ni-MH system; AB_5 and AB_2 (Pistoia, 2008). The AB_5 type is an example of $LaNi_5$. Instead of pure La metal, the alloy made of a mix of La (Lanthan), Nd (Neodym), Ce (Cerium), and Pr (Praseodym) metals is used in the Ni-MH system to improve the resistance to corrosion, and to decrease costs. Also, Ni metal can be replaced by Co, Mn, Al to hinder alloy pulverization, and enhance the capacity, and even improve the resistance to oxidation during the production (Morioka et al., 2001).

The AB_2 type alloy can be given as an example of ZrV_2 alloy. Such a type alloy has higher specific capacity than AB_5 type alloy. Nevertheless, the AB_5 type alloy exhibits a good performance in the wide temperature range. The self-discharge problems are less

likely seen in the AB_5 alloy system. Both AB_2 type alloy and AB_5 type alloy have some advantages such as high capacity, wider running temperature range, long cycle life, and high hydrogen diffision rate. Here the “A” letter represents Zr (Zirconium), Ti (Titan), and La metals, while the “B” letter indicates Ni and V (Vanadium) (Osaka and Datta, 2000, and Shen et al., 2018).

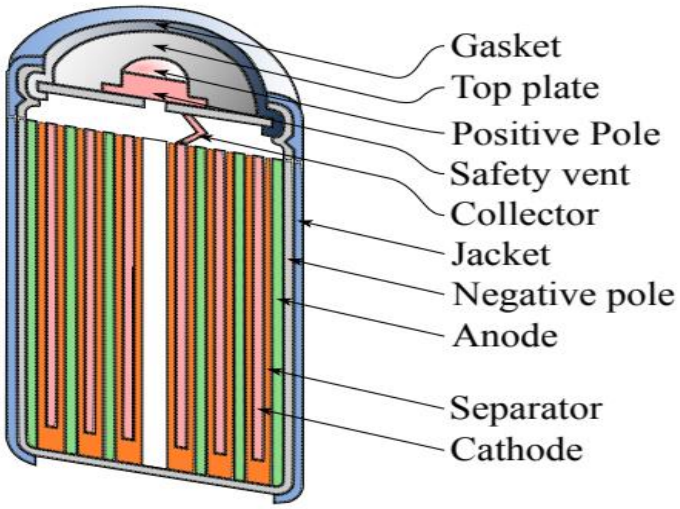

Figure 2. 4. General view of Ni-MH battery (Rodrigues et al., 2017).

2.3.1.5. Lithium Ion Battery

Towards the late twentieth century, high-energy density lithium-ion batteries appeared in the battery market. The lithium ion batteries are utilized in the military and space applications, since they have some advantages such as high power density, high energy density, lighter-weight. The lithium-ion batteries need nonaqueous electrolyte consisting of organic solvents, so choosing suitable solvents and salts for the electrolytes is crucial for getting higher capacity in such batteries. The nominal voltage of the Li-ion battery, of course depending on the cathode materials used, ranges from 1.5 V to 3.0 V (Pistoia, 2008; Shen et al., 2018).

During charge and discahrge process in these batteries, the lithium ions move between two electrodes, that is, the anode and the cathode. The active cathode is characteristically a layered structure like lithium cobalt oxide ($LiCoO_2$), or a tunneled structure like lithium manganese oxide ($LiMnO_2$). Sony utilized the first lithium cobalt oxide as the active cathode material to commercialize the lithium-ion battery. Also, there

are a great number of other cathode materials such as $LiMn_2O_4$, $LiFePO_4$, LiNi1-x-y, and $MnxCoyO_2$ (Shen et al., 2018).

The reaction related to the lithium-ion battery is step by step shown below;

Anode reaction: $LiMO2 \leftrightarrows Li_{1-x}MO2 + xLi^+ + xe^-$ (2.21)

Cathod reaction: $xLi^+ + xe^- + C_6 \leftrightarrows LixC_6$ (2.22)

The overall reaction: $LiMO_2 + C_6 \leftrightarrows LiC_6$ (2.23)

The lithium-ion battery reaction is depicted in Figure 2.5.

..

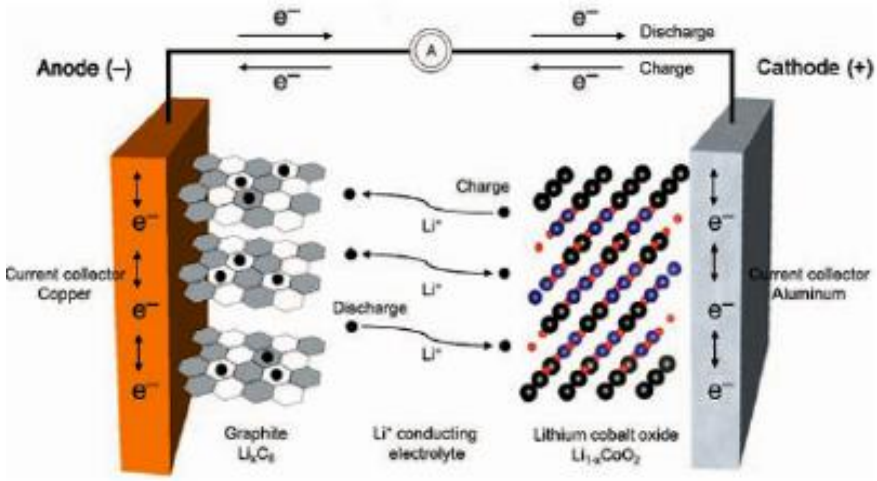

Figure 2. 5. Lithium-ion cell reaction (Diao et al. 2018).

Towards to mid-1990s, graphene-based anode, offering rougly 350 Ah/kg capacity, was used to solve the exfolation problem by using ethylene carbonate solvent instead of PC. In addition to this, that the graphene used as the anode that has a much lower surface area and higher density provides higher energy density and batter packing efficiency (Shen et al., 2018). The electrolyte consists of organic compound (such as ethylene carbonate and diethyl ether) and dissolved salts (such as $LiPF_6$ and $LiBF_4$) (Dahlin and Strøm, 2010, and Shen et al., 2018). Alumium foil sheet and copper thin foil sheet are utilized as a current collector for cathode and anode materials, respectively. It is the most significant advantages of lithium-ion battery that they has higher energy density between 150 and 200 Wh/kg, good charge-discharge properties, and high voltage

(3.6 V). Nevertheless, the most important issue is cost of the lithium-ion battery, that is, it is expensive (Shen et al., 2018).

2.3.1.6. Lithium-Sulfur Battery

Transport systems based on electric vehicles (EVs) that have low cost, suitable size, and safe driving rely on developing economic storage systems that have high energy density. The technology of new generation electrochemical energy storage provides a promising way to meet these requirements (Zhou et al., 2017). The Li-S cell, thanks to a high theoretical density of 1675-1673 mAh/g and a high theoretical energy density of 2500-2600 Wh/kg, is a suitable battery for meeting the electrical vehicles needs. The lithium sulfur battery is compese of there main components such as the active cathode, the anode and electrolyte, here the active cathode material is used as sulfur metal. In the Li-S cells, there are different chemistry mechanism from the lithium-ion cells (Chen and Shaw, 2014; Shen et al., 2018). In recent times, interest in the Li-S rechargeable cell has been increased owing to being a lot demands of high energy storage system. In addtion, the developments in the electrolyte, binder chemicals, even cell design bring about important advances in the area of this battery system within the past few years. Also, the sulfur (S) metal has some advantages such as its abundance, its unexpensive, its easy refining from mines (Chen and Shaw, 2014; Shen et al, 2018).

2.3.1.7. Lithium-Air Battery

A lithium-air battery based on lithium-oxygen system is a promising lithium battery in point of energy density, because the active cathode, the limiting ingredient (factor) in the other batteries, is not involved in this battery system. While conventional lithium ion batteries have approximatelly 150-200 Wh/kg energy density, the Li-air batteries can provide an energy density of 3582-3620 Wh/kg, that is, nearly 15 times more than the lithium-ion batteies. If the oxygen supply is not involved in the calculations, the Li-air battery potential can reach an energy density of 11000 Wh/kg. This is near to the value of 13000 Wh/kg offered by octane gasoline. Hence, in contrast to the other batteries, the Li-air battery has the potential to race with liquid fuels (Shen et al., 2018; Bruce et al., 2012).

2.4. Fuel Cell

A fuel cell is an electrochemical system that is designed to turn the energy of chemical reactions into electrical energy. Fuel cells use a source of liqiud or gaseous reactant in place of metal oxides or metals. Natural gas, petroleum, hydrogen, and water can be used as reactants for fuel cell. Fuel cells do not give off hazardous gases such as carbon monoxide (CO), sulfur dioxide (SO_2) and nitrogen oxide (NO) (Shen et al., 2018). Moreover, fuel cells comply with renewable sources and modern energy products (i.e H_2 gase) for sustainable developments. Fuel cells offer a cleaner and more efficient energy for conversion devices (Sharaf and Orhan, 2014). The first fuel cell was carried out by Sir. W. Grove in the year of 1839. A fuel cell comprises of three components; anode as a fuel electrode, cathode as an oxidant, and electrolye. General diagram of a fuel cell is illustrated in Figure 2.6.

Figure 2.6. shows that the fuel cell consists of various layers; BPP: bipolar plates, GDL: gase diffusion layers, catalyst layers, and PEM: polymer electrolyte membrane layer.

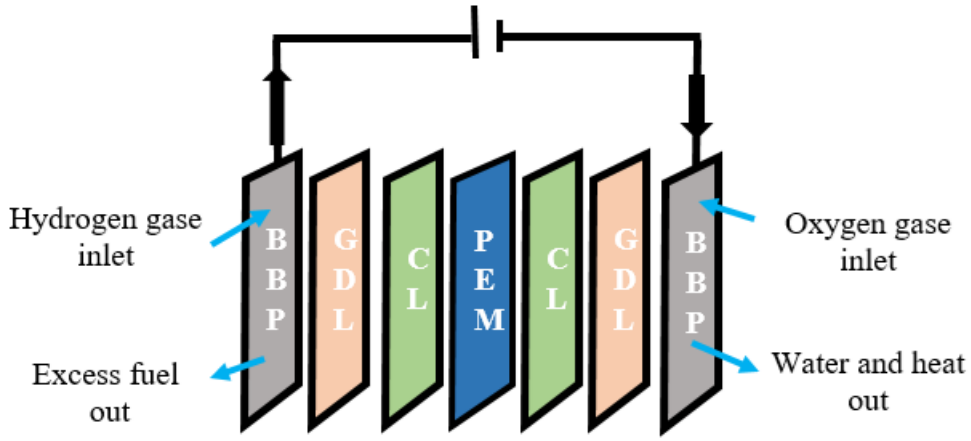

Figure 2.6. A fuel cell diagram.

The anode is fed by hydrogen as fuel, while the cathode is fed by oxygen gases, and then electrocatalytic reactions occur on every two sides in the fuel cell. Thanks to a catalytic, hydrogen gas converts to proton (H^+), then the generated protons by means of a membrane transfer to the cathode and combine with oxygen gase, finally water and heat occur (Saleh and Easton, 2013). The electricity is produced by the generated electrons by completing the circuit in the fuel cell. As shown in Figure 2.6.

The reactions are shown below in a fuel cell;

The Anode reaction: $H_2 \rightarrow 2H^+ + 2e^-$ (2.24)

The cathode reaction: $O_2 + 2H^+ + 2e^- \rightarrow H_2O$ (2.25)

Overall reaction: $\frac{1}{2}O_2 + H_2 \rightarrow H_2O$ (2.26)

Currently, there are various fuel cell types. These fuel cell types can be classified according to construction metarials and working agents. These are ; (Milewski et al. 2011)

1. Alkaline Fuel Cell (AFC)

2. Proton Exchanges Membrane Fuel Cell (PEMFC)

3. Direct Methanol Fuel Cell (DMFC)

4. Phosphoric Acid Fuel Cell (PAFC)

5. Molten Carbonate Fuel Cell (MCFC)

6. Solide Oxide Fuel Cell (SOFC) (Here, only this fuel cell will be discussed)

2.4.1. Solide Oxide Fuel Cell (SOFC)

Solid oxide fuel cell has a large scale of operating temperatures from 600^{o}C to 1000^{o}C (Wang et al. 2024). The highest energy efficiency among fuel cell types belongs to the SOFC fuel cell, also there are its various design types, for example, planar cell and basic tubular. The SOFC has three main components; the anode, the cathode, and electrolyte. The most well-known solid oxide electrolyte is yttria-stabilized zirconia (YSZ). The anode in this cell is made of nickel-cermet (ceramic-metal composite) materials. The particles of nickel uniformly spread in the solid electrolyte serve as an anode catalyst to improve the contact between the catalayts and electrolyte (Shen et al., 2018).

When hydrogen is used as fuel; the reactions is depicted below;

Anode; $H_2 + O^{2-} \rightarrow H_2O + 2e^-$ (2.27)

Cathode; $\frac{1}{2}O_2 + 2e^- \rightarrow O^{2-}$ (2.28)

Total Reaction $H_2 + \frac{1}{2}O_2 \rightarrow H_2O$ (2.29)

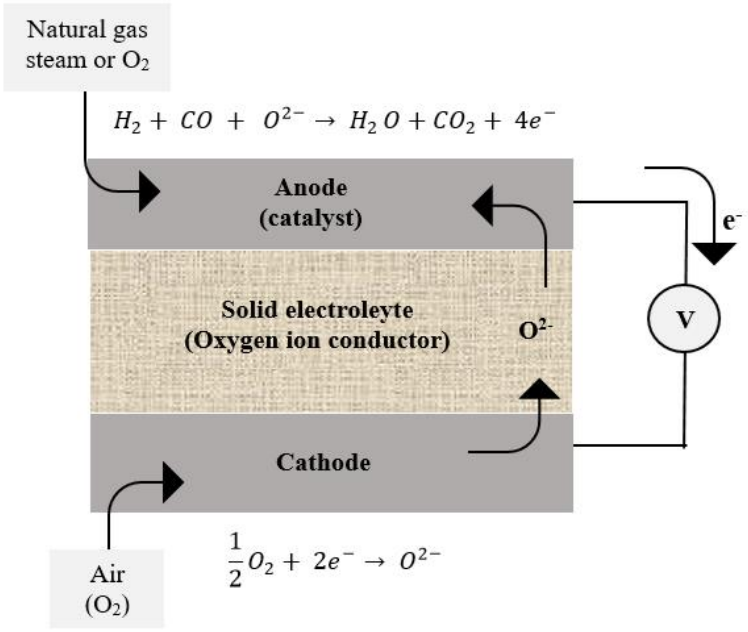

Figure 2. 7. Basic components of the SOFC.

Perovskites can be used in the SOFC as cathode and oxygen seperation membrane materials. These perovskites are ferrites-nickelates (LSFN) and Sr-doped La manganites (LSM). The formation of oxygen ions take place at the cathode, the generated oxygen ions transfer to the anode side by passing through the path of the electrolyte, then the oxygen ions (O^{-2}) react with fuels such as hyrogen gas (or CH_4) in order to produce electrons and water (Jawad et al. 2022). The basic components of a solid oxide fuel cell is shown in Figure 2.7. The SOFC gains a power interest because of its good energy conversion efficiency and fuel variety (e.i hydrogen, methane, CO, and biogas) (Tsipis et al. 2023).

2.5. Artificial Photosynthesis

There are a few definitions of artificial photosynthesis; Artificial photosynthesis is the ability to process solar energy to make cleaner energy via various chemicals (e.g., semiconductors) (Cogdell et al. 2010), or artificial photosynthesis is a designed system as an imitation of natural photosynthesis phenomena (Pradhan et al. 2022). The principle of artificial photosynthesis (AP) depends upon the use of a variety of organic or organic-metal compounds to harvest sun energy (sunlight), and then convert this energy to electrochemical potential (Abramavicius and Valkunas, 2016). It is known that solar

energy is accepted as a renewable energy in order to solve the global energy crisis (Sun et al. 2023) and environmental challenge (Pradhan et al., 2022). The conversion of carbon dioxide (CO_2) into high-value chemicals by using solar energy is crucial for a green and eco-friendly solution (Qu et al., 2024). Through photoelectrocatalytic reactions, solar energy can be transformed into several chemical fuels (CH_4, CH_3OH etc.). Artificial photosynthesis generates energy by mimicing the photosystem-II (PS-II) in the natural photosynthesis, and in this system, water molecules are split into oxygen and proton (H^+). The mechanisms of water splitting for artificial photosynthesis are shown below;

$H_2O + O_x \rightarrow O_2 + 2H^+ + Red$, (Ox: oxidation catalyst) (2.30)

$H_2O + H^+ + Red \rightarrow 2H_2 + O_x$, (Red:reduction catalyst) (2.31)

Total : $2H_2O \rightarrow O_2 + 2H_2$ (2.32)

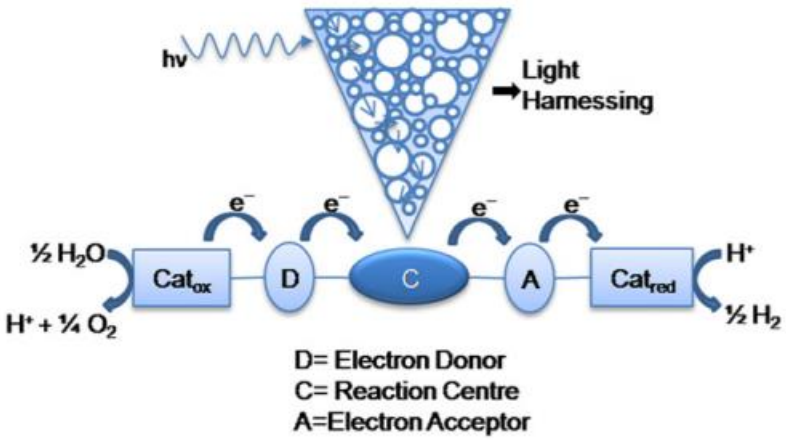

Figure 2. 8. Mechanism of an artificial photosynthesis (Arifin et al., 2012).

Artificial photosynthesis can be categorized in two systems; homogeneous and heterogeneous systems. Dye-sensitized solar cells (DSSCs) or Gratzel cells are classified in heterogeneous artificial photosynthesis system. A DSSC system contains a semiconductor and a dye compound to carry out light absorption and charge-carrier transfer. Homogeneous artificial photosynthesis consists of multi-electron process, and this system contains several components such as a light harnessing part, reaction center, oxidation and reduction (Redox) catalyst, and separator. As shown in Figure 2.8 (Arifin et al. 2012). The AP involves complicated reactions such as multiple electron and proton (H+) transfers, which make these reactions slow and cause high overpotential. To overcome the reaction barriers, powerful and effective catalysts are needed. Also, a lower

overpotential value and rapid reaction rate are needed. An effective artificial photosynthesis requires a low overpotential, a developed catalyst material, and a high catalytic rate (Zhang and Sun, 2019).

2.6. Photoelectrochemical Cell

The population growth of the world and industry sector consume a largo amount of fossil fuels, therefore they release a huge amount of carbon dioxide gas that cause global warming (Mushtaq et al. 2024). Also, recently global warming and energy crisis in the world has become a significant issue (Liu et al. 2024).

A photoelectrochemical cell depedens on a semiconductor as photoanode and a metal electrode as cathode. The important compenent of the PEC is semiconductor. Electrons generated by light goes to the metal electrode by means of conductive wire. The generated electrons produce hydrogen gas by reducing water molecules at the metal. The formed holes by incident light at the semicondutor side oxidize water to create oxygen gas.

Some recations related to water splitting are shown below;(in alkaline electrolyte)

$$4H_2O + 4e^- \leftrightarrow 2H_2 + 2OH^- \quad E^o_{red} = -0.828\,V\ vs\ NHE \tag{2.33}$$

$$2OH^- + 4h^+ \leftrightarrow 2H_2O + O_2\ E^o_{ox} = -0.401\,V\ vs\ NHE \tag{2.34}$$

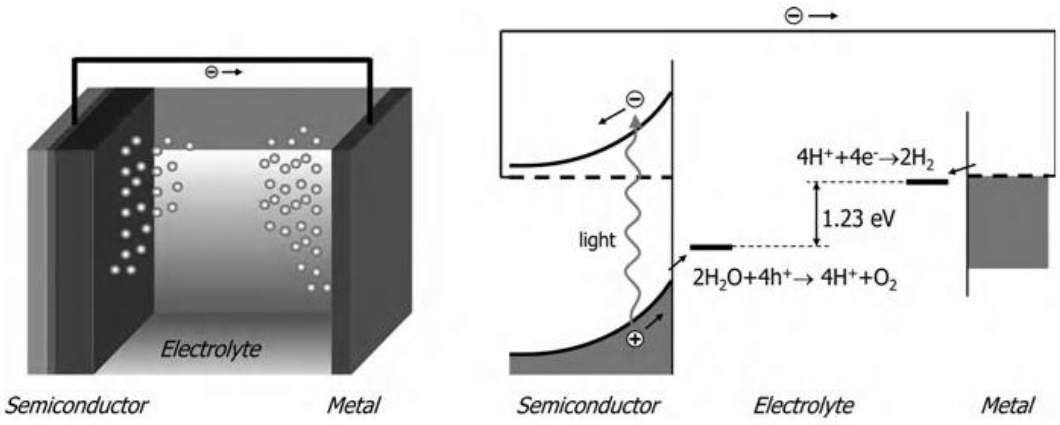

Figure 2.9. Components of a photoelectrochemical cell
(Van de Krol and Gratzel, 2012).

For an acid medium; the reactions are shown here;

$$4H^+ + 4e^- \leftrightarrow 2H_2 \qquad E^o_{red} = 0.0\ V\ vs\ NHE \tag{2.35}$$

$$2H_2O + 4h^+ \leftrightarrow 4H^+ + O_2 \qquad E^o_{ox} = -1.229\ V\ vs\ NHE \tag{2.36}$$

The fundamental concept of a photoelectrochemical cell and the mechanism of water splitting are illustrated in Figure 2.9. The general water splitting reaction can be expressed by Gibbs free energy equation.

$$\Delta G = -nF\Delta E \tag{2.37}$$

At standard temperature and concentration, the voltage of the PEC is -1.229. And Gibbs free energy equals to +237 kJ per mol. Thermodynamically, water splitting reaction is hard (Van de Krol and Gratzel, 2012).

2.6.1. Water splitting

Hydrogen is considered a promising energy source that replaces fossil fuels in the future energy concept. There are several advantages of hydrogen gas, such as clean, eco-friendly, non-hazardous, and renewable energy sources. Water splitting is significant process to generate hydrogen gas, because this process is accepted as a sustainable process that offers carbon-free fuel and storage of renewable energy. Various methods have been utilized to split water molecule, for example, photoelectrochemical cell, photocatalytic, photobiological, and thermal decomposition. A number of semiconductors have been developed by many studies to split effectively water molecules into hydrogen and oxygen (El Idrissi et al. 2024). In the year of 1972, Fujima and Honda depicted the first concept of water splitting photoectrochemical by using titanium oxide (TiO_2) that absorp Uv (ultroviolet) light.

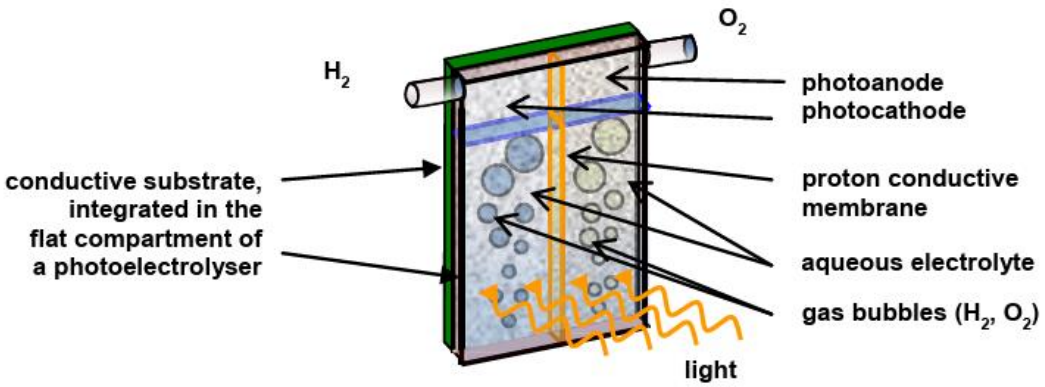

Figure 2.10. A water splitting device (Abramavicius and Valkunas, 2016).

A water splittig tool consists of an n-type and a p-type electrode. As shown in Figure 2.10. Interestingly, a study conducted by Khaselev and Turner in 1998 demonstrated photoelectrocatalytic water splitting using visible light (Vis-light), The photoelectrochemical cell used in their study was made of p-GaInP2 layer and GaAs p/n layer on a GaAs substrate (Bachmeier, 2016).

2.7. Solar Cell

A solar cell is a p-n junction tool; its operation is simple. However, a solar cell has a complex structure because it must minimize energy loss to be effective. Therefore, true information about optical process in the solar cell is crucial to figure out energy loss mechanism in the system. A solar cell can, in short, be defined as a device that uses solar light to generate electricity. The solar cell has an important place in solar energy technology. Moreover, the solar cell (photovoltaic) has recently become a significant device to meet ever-increasing energy requirement across the world (Jaun et al. 2015, Fujiwara and Collins, 2019). The principle of a solar cell depends on the p-layer as an absorber and the photocarriers generated in the semiconductor absorber layer. The conversion efficiency of a solar cell (photovoltaic) can be formuled below;

$$\% \, \eta = J_{sc} \, x \, V_{oc} \, x \;\; FF(\%)/0.1(\frac{W}{cm^2}) \tag{2.38}$$

Here, Ƞ, J_{sc}, V_{oc}, FF represents conversion efficiency, short-circuit current density, open-circuit voltage, and fill factor, respectively.

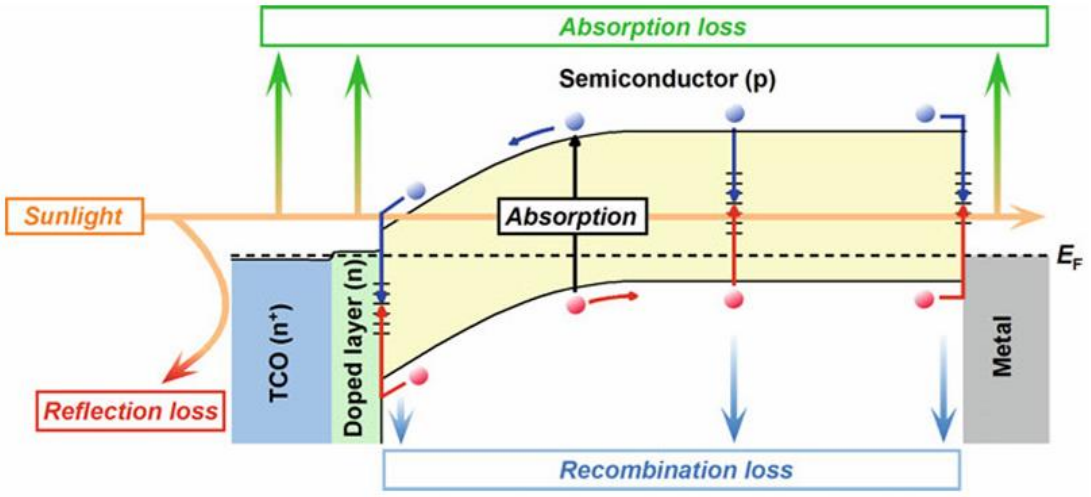

Figure 2. 11. Current loss in a solar cell: absorption loss, recombination loss, and reflection loss (Fujiwara and Collins, 2019).

When the solar cell is exposed to sunlight, various losses, such as absorption loss, recombination loss, and reflection loss can occur in the solar cell (seen Figure 2.11). These three phenomena lead to a decrease in the efficiency of the solar cell. To get high efficiency in the solar cell, these phenomena are necessary to remove or minimize (Fujiwara and Collins, 2019).

CHAPTER 3

3.1. Cathode Active Materials

Metal oxides or hydroxide are widely utilized as energy storage materials for batteries, capacitors, and fuel cells. Recently, scientists have profoundly worked on the oxides or hydroxides electrode materials, because these electrode materials have been promising for energy storage technology and energy related materials. To give an example, the oxide forms of transition metals in the periodic table such as cobalt (Srinivasan and Weilder, 2002), nickel (Kim et al., 2002), manganese (Suh-Cem Panga, 2000), and iron (Wang and Wu, 2003), have been commonly used as electrodes in supercapacitors, in catalyst works, and even in battery system. On the other hand, the hydroxide forms such as nickel hydroxide are widely used as cathode materials in the Ni-based batteries such as Ni-Cd and Ni-MH cell (Dahr et al., 1997).

Here, some important cathode materials will be discussed.

3.1.1. Nickel Hydroxide

Nickel hydroxide has four crystal forms: alpha-nickel hydroxide (α-$Ni(OH)_2$), beta nickel hydroxide (β-$Ni(OH)_2$), sigma nickel oxyhydroxide (γ-NiOOH), and beta oxyhydroxide (β-NiOOH). The hydroxide forms of them are situated in a hexagonal system. The α-$Ni(OH)_2$ form has a more disordered structure and large interlayer spacing. (Doyle et al., 2013).

Two phases of nickel hydroxide (alpha and beta forms) were indendified by Bode and his colleague for the first time (Bode et al., 1966). During charging and discharging, the phase transformations of nickel hydroxide are indicated in Figure 3.1.

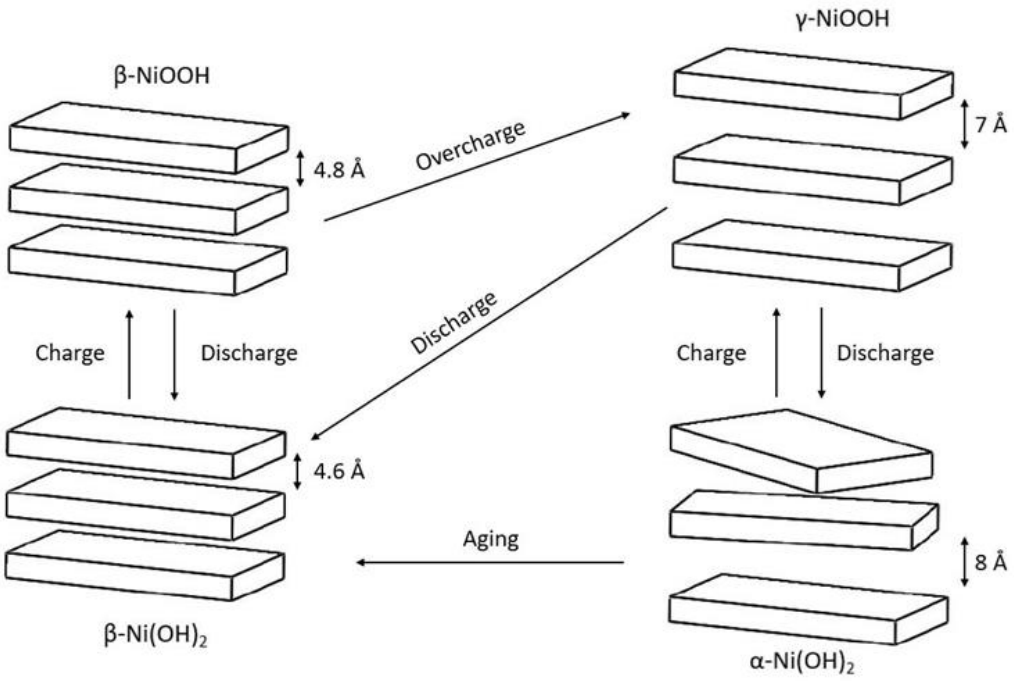

Figure 3.1. Phase transformation of nickel hydroxide
(Tsais and Chan,2013).

During charging process, the β-$Ni(OH)_2$ form changes into β-NiOOH form and the α-$Ni(OH)_2$ form transforms into the γ-NiOOH phase. When it comes to discharge, the reverse of these changes occurs. On overcharge process, the β-NiOOH phase transforms into the γ-NiOOH phase.

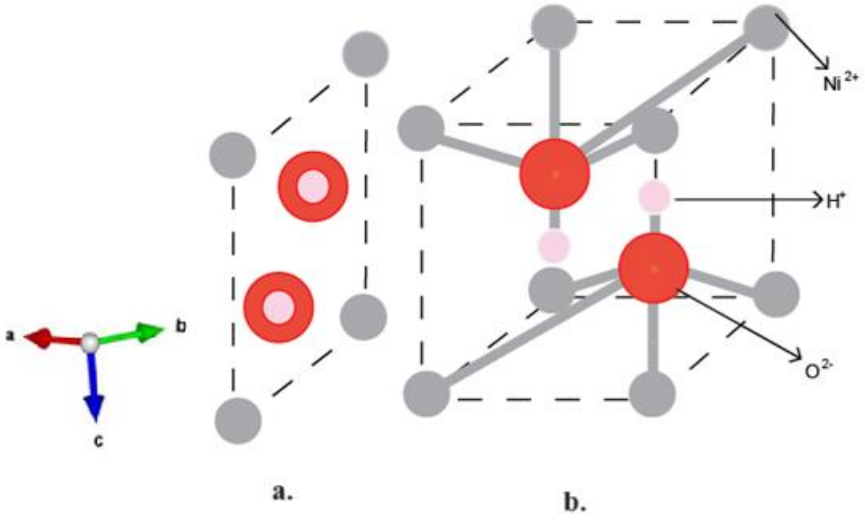

Figure 3.2. **a**. Cross-section **b**. β-$Ni(OH)_2$ crystal structure.

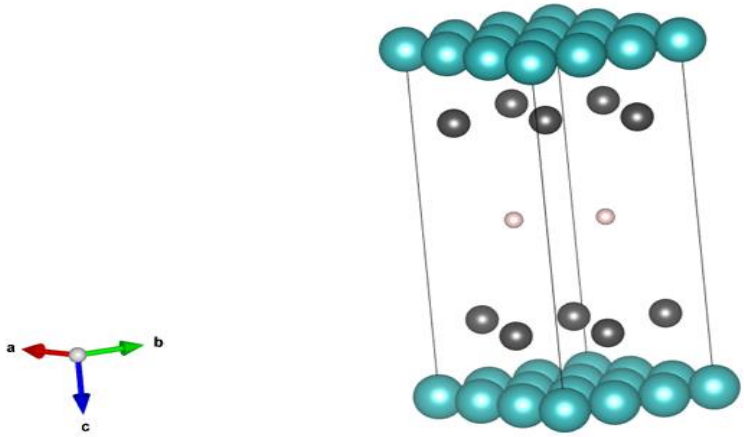

Figure 3.3. α-Ni(OH)$_2$ crystal structure (Ni:Green, O: Black ones, pink small balls represent intercalated water or anions) (Ilhan, 2022).

Nickel hydroxide (Ni(OH)$_2$) is an important cathode material. The Ni(OH)$_2$ has attracted much attention in electrochemical applications such as electrochemical sensors, supercapacitors, electrocatalysis, and nickel-based rechargeable alkaline batteries, because it provides good stability even under harsh conditions (Abbas et al., 2019).

Nickel hydroxide also has a good theoretical capacity (433 mA / g) and it is eco-friendly, abundant, and cheap (Tao et al., 2014). When the beta form of nickel hydroxide is compared to the alpha form of nickel hydroxide, the alpha form includes water molecules and some ions in the interlayer. That is why the interlayer gap of the alpha phase is more broad than the beta phase (Mavis and Akıncı, 2004). There are various nanostructures of alpha nickel hydroxide (α-Ni(OH)$_2$) such as coral-like (Li et al. 2013), pompon-like (Wang et al. 2013) flower-like (Bastakoti et al, 2012), and ultra-thin (Jiang et al. 2011)

The β-Ni(OH)$_2$ phase is in the structure of brucite-like. The β phase is more stable in the base medium and also it has a lower specific capacity (289 mAh/g) (Lee et al., 2001) when it is compared to the specific capacity of the alpha phase (433 mAh/g) (Hu and Noreus, 2003).

During the charging process, Ni in the α-Ni(OH) is oxidized Ni^{+2} to Ni^{+4}, but Ni in the β-Ni(OH)$_2$ phase changes from Ni^{+2} to Ni^{+3}. In addition, the oxidation states of Ni in the alpha phase have a +4 charge, but only two electrons are not involved in the reactions. Some studies demonstrate that the oxidation states of nickel in the alpha phase can be +3.5 and +3.68 values (Desilvestro et al., 1988).

Some of the anions, such as carbonate (CO_3^{-2}), sulfate (SO_4^{-2}), hydroxide (OH^-), nitrate (NO_3^-), and chloride (CI^-), enhance oxygen evolution potential. The OER causes recombination reactions, so the oxygen from the anode goes to the anode material, and the oxygen deteriorates the anode electrode by oxidizing. This event can be seen in the Ni-Cd and Ni-MH battery types. Cell voltage starts to drop when the recombination reactions occur and this is called as “negative delta voltage”. To repress the oxygen evolution reaction, lithium hydroxide (LiOH) salt, by adding to the electrolyte, is used (Shangguan et al., 2020).

3.1.2. NMC/NCA Cathode Materials

Recently, researchers have intensively studied lithium-ion cells due to the decrease in fossil fuels and the development of electric vehicles (EVs). The supply of a good active cathode for the Li-ion batteries is a significant issue to meet the needs in the technological developments and in the battery sectors. NMC and NMC-derivatives are some of the most important cathode active materials that are utilized in most Li-ion batteries and next-generation batteries. NMC material has a high theoretical capacity, low toxicity, and good thermal resistance. Also it posseses high energy density. The NMC cathodes have about 234 mAh per gram of specific capacity (Elong et al., 2023).

Compared to $LiMO_2$(here, M represents Ni, Co, and Mn atoms), NMC-based active cathode materials consist of three transition metals in which Ni atom offers high capacity, whereas cobalt and manganese atoms provide high integrity and layered structure (Li et al., 2020).

For prospective studies in the NMC chemical compounds, there are various ways to improve the NMC performance such as enhancing the nickel amount stoichiometrically in its formula and changing the crystal structure of the NMC cathode. These improvements offer a broad voltage range for the NMC active cathode. The traditional nickel-rich NMC active cathode materials have a polycrystal (PC) structure, but unfortunately, Ni-rich NMC cathode materials, because of this polycrystal property, suffer from cracks in the crystal, side reactions, intercalation process, and volume changes. Some studies have been conducted on a familiy of single-crystal (SC) of Ni-rich NMC active cathode, which offers ultralong cycling life, high electrochemical stability, and high capacity retention, such as 92 % of 4700 cycles at 3-4.3 voltage. However, The PC structure of nickel-rich NMC displays low cycling life and lower retention rate; for

example, there are studies showing that the PC structure of the NMC cathode has only 92 % capacity retention after 200 cycles. It is clear that single-crystal NMC structure is remarkably superior to polycrystal NMC one (Sun et al., 2022).

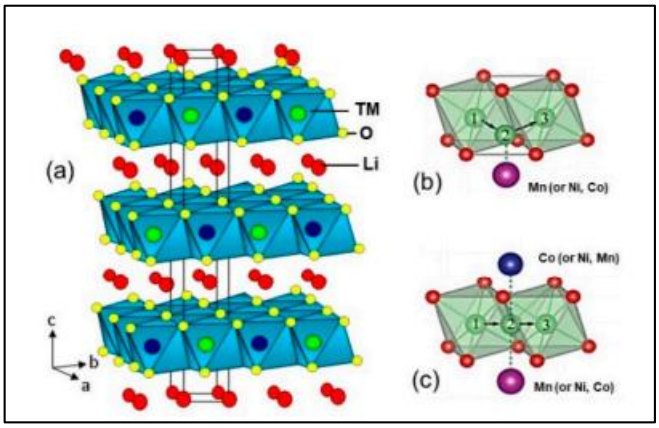

Figure 3.4. a. Layered NMC structure. Colors; Green:Li atom, red: O atom, silver: Ni atom, purple: Mn atom, and Blue: Co atom. b Tetrahedral site pathway. c.Oxygen pathway for lithium ion (Juilen and Mauger, 2020).

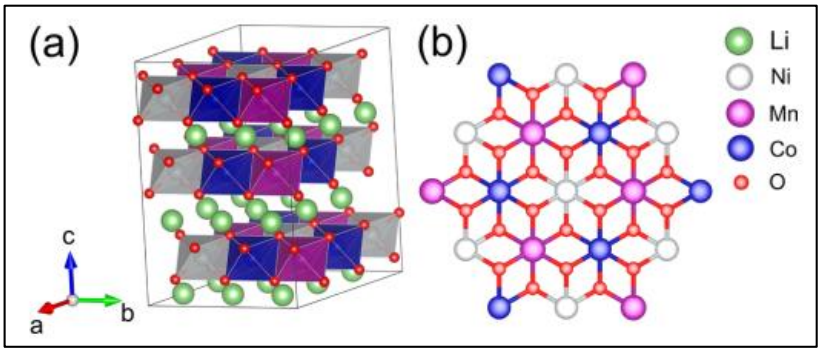

Figure 3.5. a. NMC111 bulk structure. b. Ion arrangment in NMC111 (Garcia et al., 2017).

The bulk structure of the NMC111 is illustrated in Figure 3.5a. The NMC111 structure has *R3m* space group. Every transition metal in the structure of NMC11 is surrounded by six ions, as shown in Figure 3.5b (Garcia et al. 2017). The Figure 3.4. shows that Li ions are encircled by the oxygen layers in octahedral form. Here, hexagonal cell unit contains three sets of cobalt and lithium layers (Juilen and Mauger, 2020). On the other side, there is active cathode material, which contains nickel, cobalt, and aluminum, or shortly is named as NCA. The NCA is a promising and an important cathode material, because it provides high energy density and high power density for

lithium-ion cells. The NCA has 180-200 Wh per kg of specific energy at high voltages, such as 3-4.2 V. The NCA active material can be produced by using sol-gel, co-precipition, solid state, and spray pyrolysis methods. Although carbonate co-precipition method is less popular, this method offers good particle size, better morhology, and lower retetion time. The co-precipition methods have some advantages such as spherical morphology and good tap density compared to the other methods (Ekawati el al. 2018). The NCA is especially a significant cathode material for sulfide (S)-based solid state battery (Jiang el al 2024). Moreover, the NCA capacity is better than the other cathode materials such as NMC333, lithium cobalt oxide, and lithium iron phosphate (Singh et al., 2022).

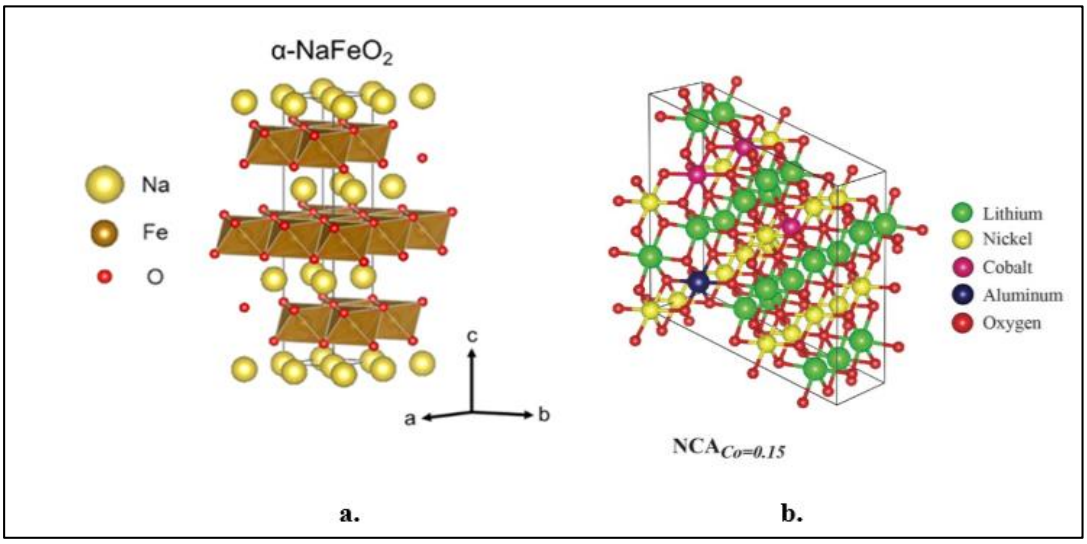

Figure 3.6. a. Alpha-$NaFeO_2$ crystal (McAuliffe et al. 2023). b. NCA crystal structure (Ghatak et al., 2017).

The NCA and the NMC materials are similar crystal structure. The NCA is in the *R3m* space group, just like layered alpha-$NaFeO_2$ crystal structure, as shown in Figure 3.6. Although the NCA and the NMC material have the same nickel content and similar atom radius (Al^{+3} 53.5 pm, Mn^{+4} 53 pm), these active materials can exhibit different behaviors. For example, it has been shown in various studies that the NCA structure has lower structural stability but has high electrochemical performance (Ren et al. 2023).

3.2. Other Energy Related Materials

3.2.1. Semiconductors

Semiconductors have recently become an important key because of various technological developments such as artifical intelligence (AI), robots, and autonomous cars, etc. Semiconductors are profoundly used in the sensor and communication components sector (Cho and Ju, 2023). A great many semiconductors are utilized in electronic devices, such as LED, detectors, sensors, photovoltaic solar cell, photoreceptor, and so on.

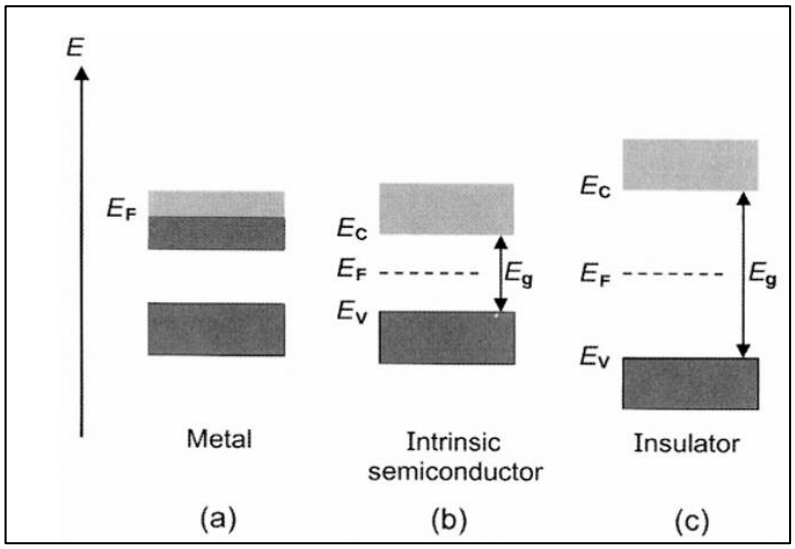

Figure 3.7. Band diagrams of Metal (a), Semiconductor (b), and Insulator (c). (Yacobi, 2003).

Metals, semiconductors, and insulators have different electronic band properties. In Figure 3.7. E_g indicates the energy band gap between the conductive band and the valence bands. In semiconductors, this value (Eg) ranges from 0 to 4 eV. Also semiconductors have approximately $10^{-3} – 10^{9}$ Ω.cm resistivity. In an insulator, there are no electrons in its conduction band, but its valence band is completely full of electrons. In this case, when an electric field is performed, any current does not occur, these are called "insulator material". An insulator has very large resistivity and very small conductivity. On the other hand, semiconductors have few electrons in the conduction band (allowed energy band), but its valence band is full with electrons. The band gap energy of semiconductors is smaller than the band gap energy value Eg of insulators.

Here, when an electric field is applied, the electrons can move to higher energy level. As shown in Figure 3.7 (Yacobi, 2003 and Neamen, 2003). Metals indicate very low resistivity and very good conductivity. The conduction band overlaps the valence band in metal materials. So, the electrons can easly move to higher energy levels in metals. The *Fermi level* (Fermi energy) E_F is a reference energy that shows the possibility of occupation of electron states (Yacobi, 2003 and Neamen, 2003).

Some semicomductor types and their properties are summarized in Table 3.1.

Table 3.1. Semiconductor types. (Yacobi, 2003, summarized and tabularized)

Semiconductor Types	Examples	Properties (usage etc)
Elemental	Si, Ge, Diamond (C), B, Se, Te, P	In various electronic device applications
Compound	**III-V Group:** GaAs, GaP, GaN, AlAs, InAs, InSb, InP	LED Technologies, optoelectronic device,
	II-VI Group: ZnSe, ZnS, CdS, CdTe, ZnTe	ZnTe is p-type, the others are n-type (electronic devices)
	IV-VI Group: PbS, PbSe, PbTe.	High carrier mobility, high dielectric constant
	I-III-VI_2 Group: $CuAlS_2$, $CuInS_2$, $CuGaS_2$, $CuInSe_2$	Photovoltaic solar cell
Layred compound	MoS_2, ZrS_2, HgI_2, PbI_2, GaSe, InSe	Nuclear detection, covalent-Van der Waals bonds dominant, exhibit quantum effects.
Narrow energy-gap	InSb, InAs, PbSe, PbTe, PbS	<0.5 eV, IR detector, optoelectronic device etc.
Wide energy gap	C, SiC, AlN, GaN, ZnSe, ZnS,	Electronic devices, RF, microwave, thermal stability
Oxide	ZnO, SnO_2, CuO_2, Bi_2O_3, $BaTiO_3$, $SrTiO_3$, $LiNbO_3$.	Sensor, resistor, PTC thermistor, veristors, MOS structures, electro-optic modulators
Magnetic	FeO, NiO, EuO, EuS	Offer large magneto-optical effect, optical modulators
Amorphous	alpha-Si:H, alpha-Se, alpha-As_2Se_3, alpha-Se	Photoreceptors, electrophotographical copier
Organic	anthracene, polyacetylene, $C_{14}H_{10}$, p-phenylene vinylene (PPV), polyimid.	Photoreceptors, photoconductor, low-cost, LED, solar cell, non-linear optical materials

3.2.2. Perovskite Materials

Perovskite was discovered by Gustow Rose in 1839, but the name of the perovskite comes from Russian mineralogist L. A. Pervoski. Perovskite is in the class of the calcium titanate ($CaTiO_3$) mineral. General structure of perovskite can be symbolized as ABX_3 (Ahmad et al., 2021). Types of insulator, semiconductor, and superconductor perovskite are known. Moreover, the perovskite materials especially in certain temperatures demonstrate piezoelectric, pyroelectric, ferroelectric, antiferroelectric, and paramagnetic properties. The crystal structure of these materials in the lattice can be cubic, monoclinic polymorphs, trigonal, tetragona, and orthorhombic based on the tilting and rotation of BX_3 (Park et al., 2016; Pan and Zhu, 2016).

The perovskite compound consists of A^{2+} (divalent) cations and B^{4+} (tetravalent) cations. In the structure, the A cation is located at the corner of the cubic shape, whereas the B cation is placed in the middle of the cubic. The B cation is surrounded by six X^{2-} anions in the face-centered of the cubic unit cell (Pan and Zhu, 2016) (See Figure 3.8).

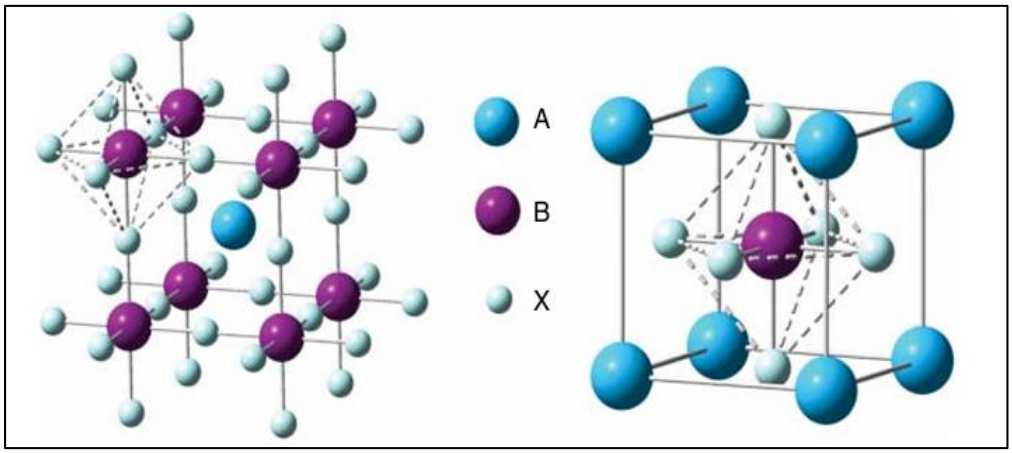

Figure 3.8. General structure of perovskite (Ahmad et al., 2021).

In the perovskite materials, one of the most important expressions is Goldschmidt tolerance factor, and the factor is symbolized by the “t” letter. The tolerance factor exhibits the stability of perovskites. In the ideal conditions, the tolerance factor of perovskite cubic structure is 1. Therefore, to get a high stability perovskite, the tolerance factor should be closer to 1. The mathematical expression of Goldschmidt is given below.

$$t = \frac{r_A + r_O}{\sqrt{2}(r_B + r_O)} \quad (3.1)$$

Here, r_A, r_B, and r_O represent the radius of A cation, B cation, and oxygen, respectively (Saikia et al., 2022)

There are some factors that affect the stability of perovskites: ion migration, chemical stability, thermal stability, and light stability. Ion migration brings about delayings in photoelectronic responses and unstable behavior in some electronic devices such as microscopy and spectroscopy techniques. When ions move across defects in the structure, these ions enter the crystal structure of perovskite. This phenomenon leads to a change in the electronic conductivity of the perovskite. Moreover, the phenomenon produces negative capacitance and irreversible degradation in the perovskite materials, even deteriorates LEDs, LCDs (liquid crystal display), and photovoltaic cell.

In the chemical stability, perovskite materials absorb easily moisture from the environment due to their ionic characteristic. For instance, when $MAPbI_3$ (MA: methylammonium) gets water vapor, it transforms into $MAPbI_3.H_2O$ (hydrate form). After a while, especially in excess water, this perovskite is deteriorated. Tin (Sn)-based perovskite material is destabilized by oxidation ($Sn^{2+} \rightarrow Sn^{4+}$). In thermal stability, some perovskites such as $MAPbX_3$ under high thermal stress can decompose into different chemical species. Inorganic perovskites endure up to 580^{o}C and can remain stable. Light affects the sturcture of perovskite. For example, the incident light lead to generate more electron and holes in perovskite, and this phenomenon may reduce activity of perovskite and can deteriorate structure of perovskite (Fu et al., 2022). The perovskite compounds can be categorized into inorganic perovskites, alkaline halide perovskites, organic halide perovskites (Assirey, 2019).

BSCF perovskite contains Ba (Barium), Sr (Strontium), Co (Cobalt), and Fe (Iron) elements. The BSCF is promising perovskite material that is used low temperature solid oxide fuel cells (SOFCs). The BSCF belongs to ABO_3 (A and B cations O: oxygen) perovskite class. The ABO_3 is a significant cathode material to improve SOFCs. The BSCF exhibits high electrocatalytic activity at low temperature systems. Also, recently, the BSCF compounds are used to seperature oxygen and oxide methane. Owing to its high performance, especially at low temperatures, the BSCF is accepted the next generation cathode material for SOFCs (Subhashini and Rajesh, 2023). Figure 3.9 shows three-dimention (3D) porous of the BSCF structure and crystal structure of the BSCF.

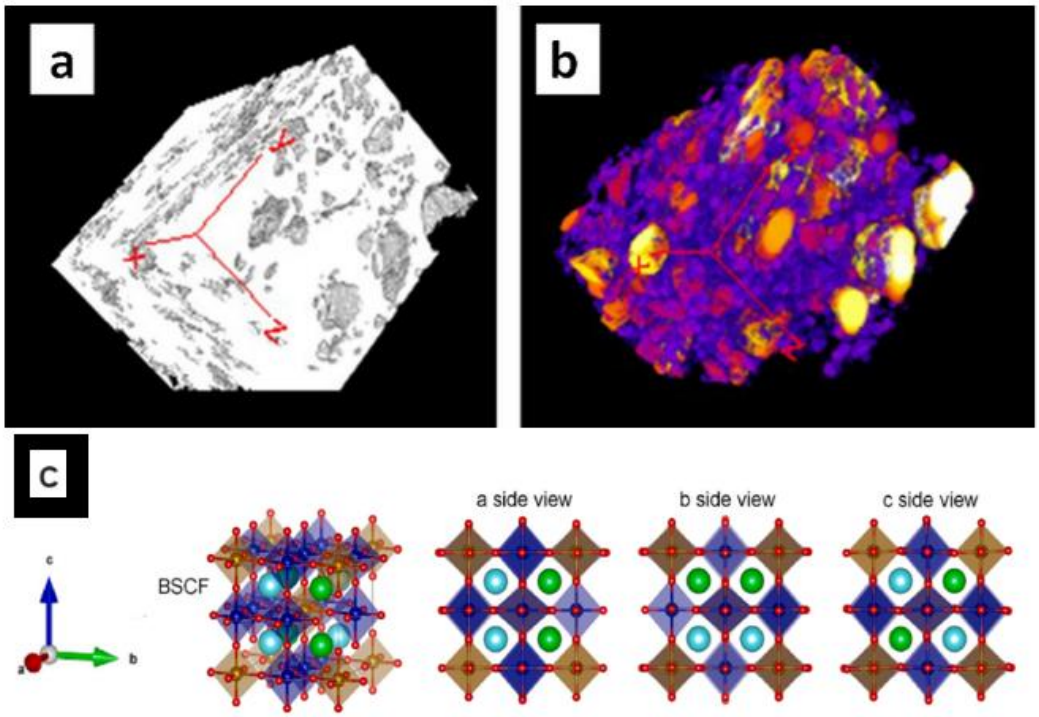

Figure 3.9. 3D porous structure of BSCF a (surface) b (internal) (Rachadel et al., 2017) c. BSCF structure (Ba, Sr, Co, Fe, and O represent light-blue color, green color, dark-blue color, yellow color, and red color, respectively) (Yang et al., 2024).

The BSCF is a type of mixed ionic and electronic conducting perovskite compound and gains much attraction due to its perfect catalytic property for reduction-oxidation reactions. Moreover, the BSCF is utilized as an anode material because it exhibits a high surface exchange coefficient and oxygen diffusion coefficient. Some studies have figured out that the BSCF cathode material can be used for carbon dioxide electrocatalysis. However, under a CO_2 atmosphere, the BSCF is chemically a non-stable compound and easily decomposes to some chemical species. The various dopants, especially high valence ions, such as titanium (Ti^{4+} and Ti^{5+}) are used to improve the stability of the BSCF (Liu et al., 2021).

3.2.3. Metal Oxides

Recently, multi-metal oxides have been significant materials across the world. These materials are widely utilized in many fields, such as electronic devices, capacitors, and catalytical applications. Also, metal oxide materials are used to split water into

hydrogen and oxygen for energy. Moreover, some of them can be used as pigment for paints and as additives in foods (Harunsani, 2013).

Transition metal oxides (TMOs) are found in various forms, for instance, binary oxide (bimetal oxide), ternary oxide, and quarternary oxide (Pan and Zhu, 2016). Metal oxide materials are commonly used as catalyst in petroleum, chemical, and environmental studies. Also, The TMOs exhibit some important properties such as multielectron transfer, various elementals, and various structures (Yang et al., 2020 and Fierro, 2005). TMOs offer high energy density because of their good conducitvity and structural stability, also they are used in pseudo capacitors. Some metal oxides like MnO_2, NiO, Fe_2O_3, Cr_2O_3, Co_2O_3, TiO_2, RuO_2, ZnO are well known (Yesuraj et al., 2024). Iron, cobalt, manganese, nickel molybdenum are profoundly studied on their catalytical activities to split water. For example, the oxide forms of Co, Zn, Ni, Mn play a good role in the electrocatalaytic activities of HER and OER (Kannan et al., 2024).

Copper (II) oxide (CuO) is a metal oxide of semiconductor (p-type), cheap, stable, and earth-abundant. Also, the CuO is used to improve photoelectrochemical performance.

Zinc(II) oxide (ZnO) has a 3.3 eV band gap energy and is an n-type semiconductor that is stable, unexpensive, and non-hazardous. Moreover, the ZnO has a good optical band gap to generate hydrogen and oxygen from H_2O (Kakavandi et al., 2024). Rock salt, wurtzite, and zinc (Zn) blende are a variety of forms of zinc oxide. Wurtzite form is more stable than both of the other forms at room temperature and pressure (see Figure 3.10) (Ding et al., 2018).

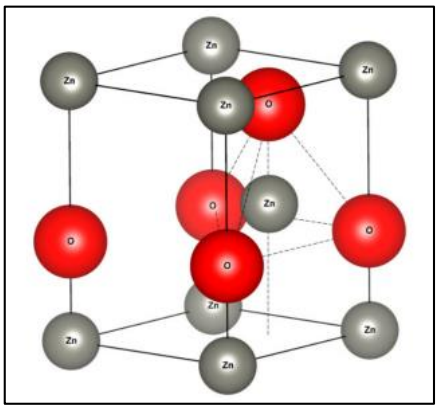

Figure 3.10. Wurtzite zinc oxide form (Ding et al., 2018).

Nickel oxide (NiO) is a photocathode material and it is used in the electrochromic tools. Also, The NiO has a large band-gap (between 3.6-4eV) (Alibabaei et al., 2013).

Moreover, the NiO has co-catalyst properties for hydrogen evolution (Kudo and Miseki 2009). The NiO is a p-type semiconductor and is used as anode for lithium ion batteries.

Iron in the iron oxide has 2+ and 3+ charges. Iron (Fe) is common element on the earth. Due to its this property, oxide form of Fe can be easily produced and are commonşy found around us. Iron oxide has a ability to absorp sunligth (solar irradiation),also it is an important material for solar energy conversion. There are a few forms of iron oxide, for instance, α-Fe_2O_3 (alpha-hematite form) and γ-Fe_2O_3 (sigma-maghemite form). The most significant form of iron oxide is alpha-Fe_2O_3 or hematite. The Hematite form is used to generate hydrogen via solar irradiation. The hematite form has hardness and thermal-chemical stability. The crystal structure of α-Fe_2O_3 is idendical to corundum (Al_2O_3) crystal structure that is R $\bar{3}$c space group. It has been reported that the bandgap of α-Fe_2O_3 is 1.9-2.2 eV (Van der Krol and Gratzel, 2018) and the absorption profile of alpha-Fe_2O_3 is between 625-564 nm (Sankir and Sankir, 2018). Moreover, the iron oxide (alpha-Fe_2O_3 and Fe_3O_4) is utilized as next generation anode material for Li-based batteries. The iron oxide is cheap and non-toxic material and has a high theoritical capacity and a high electrochemical performance (Nanda and Augustyn, 2022).

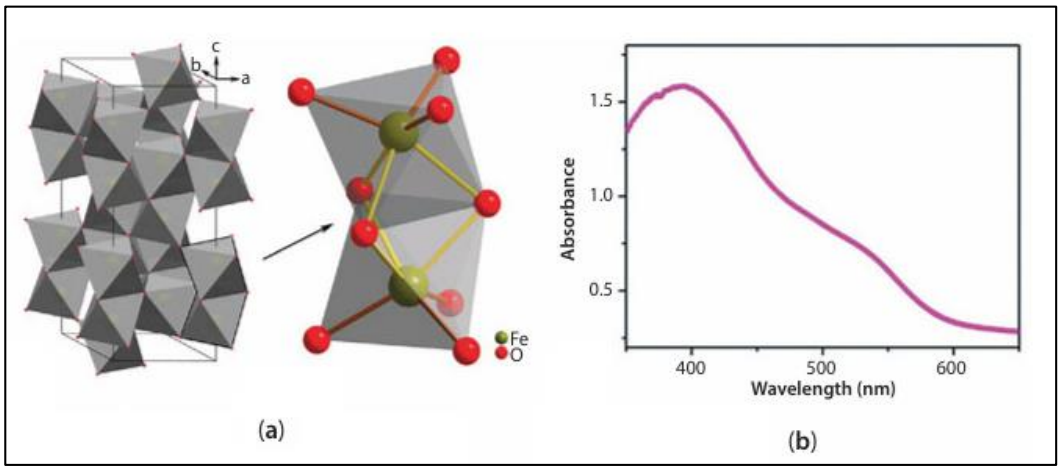

Figure 3.11. a. Hematite (α-Fe_2O_3) structure and b. Light absorption range (Sankir and Sankir, 2018).

Mangenese dioxide is profoundly utilized in primary Li-based batteries, and can reach up to about 210 mAh/g as capacity. There ara various polymorphs of manganese oxide, for example, γ, α, ε, β, δ and λ phases. Alpha, beta, and gamma phases are depicted in Figure 3.12. Among these phases, γ, α, and β forms shows one-dimention structure. Beta-manganese dioxide is the most stable among the other phases (Wu et al., 2011). The

MnO_2 is used as anode material because of its abundancy on the earth, economic, low-redox potentail and high theoretical capacity (Nanda and Augustyn, 2022). Alpha-MnO_2 is widely performed as cathode material for magnesium batteries and aluminium rechargeble batteries (Chiku et al., 2023). Manganese oxides has catalyst property to purificate water and are used oxidant in some applications, for instance, elimination arsenic (Younas et al., 2024).

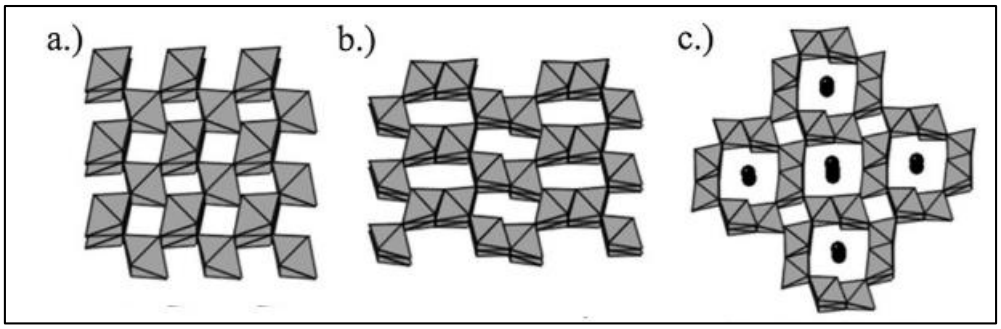

Figure 3.12. beta(a), gamma(b), and alpha(c) phases of manganese dioxide (Miao et al., 2019).

Chromium oxides can be different structures like monochromate (CrO_4), dimer(Cr_2O_7), trimer (Cr_3O_{10}), and tetramer (Cr_4O_{13}) (Fierro, 2005). Chromium dioxide has half-metallic ferromagnet properties and is used in application of magnetic tunnelling devices. Chrome dioxide has a metastable structure, and easily decomposes into Cr_2O_3 form (Wu et al., 2011). Also, chrome oxide is widely utilized as green pigment for ceramics, printing, gum elastic, and plastics (Li et al., 2009), including catalyts (Xu et al., 2006), because of its high resistance to chemicals and corrosion (Li et al., 2009).

3.3. Literature Review

Most of modern society has required the discovery and development of advanced materials for science, engineering, and health. Now, functional materials are developed to meet some needs such as energy conversion, energy storage, health care, water purification, and even societal fields. Recently, it has been expected that the discovery of material can increase significantly by the combination of artificial intelligence (AI) and automated experimentation systems. This combination is called “self-driving laboratory”.

High-throughput experimentation (HTE) methode, already available in modern research centers and laboratories, has been widely used to discover advanced materials.

The HTE method helps synthesize and characterize materials, and accelerates the production and discovery of material. The HTE offers low cost, reproducibility, and time-saving. Also, the HTE has been predominantly utilized in catalysis, biological studies, and storage materials.

Self-driving laboratory (SDL) comes from the combination of AI and automated experimentation. The SDL is widely utilized in the field of chemistry application and material, in the electronic structure predection, drug design, synthesis, and optimization studies.

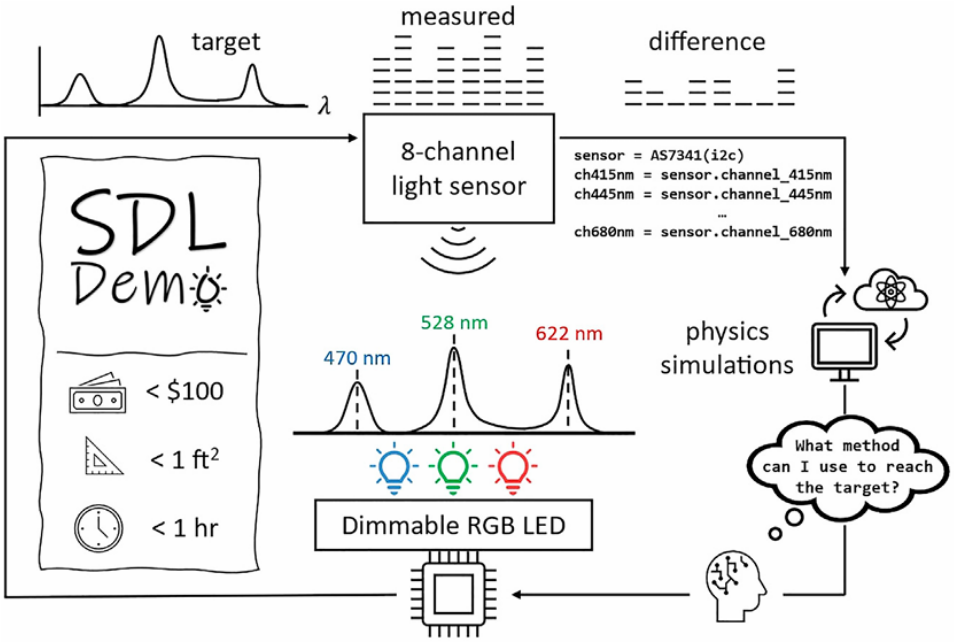

Figure 3.13. Summary of the SDL (for controlling the brightness of red, green, and blue light from LED) (Baird and Sparks, 2022).

Baird and Sparks have shown that the SDL is low cost, time-saving, and less occupying place. At different wavelength, by using the SDL, the controlling brightness from red, blue, and green ligth was demonstrated in Figure 3.13 (Baird and Sparks, 2022).

Scientists, at Carnegie Mellon University, have reported an AI named Coscientist that indicates the power of large language model (a kind of computer algorithm) for chemistry science research. Students or users have directed some question to Coscientist to learn reaction procedure and a needed reaction, and to execute the required chemical experiment (See Figure 3.14). The Study has shown that Coscientist can design, plan, and perform chemistry experiments (Boiko et al., 2023).

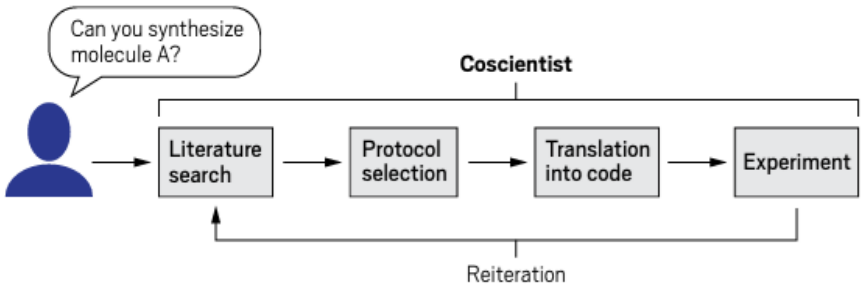

Figure 3.14. Learing cycle of Coscientist (Patel, 2024).

LNMCO is a Li-rich cathode material with a heterostructure for lithium-ion cells. The surface modification of the LNMCO was studied by Zhang and colleagues by using hydrazine vapor at different temperatures. Some studies have shown that when the LNMCO cathode material was treated by 0.4 percent hydrazine solution, Li ions were removed via the hydrazine solution from the Li_2MnO_3 phase in the LNMCO material, which enhances electrochemical performance of the cathode material (Zhang et al.,2015 and Oh et al., 2014).

The study conducted by Zhang and colleagues was performed at different temperatures, 120, 300, 500, and 700^oC, respectively. The study has shown that at 300^oC, by hydrazine vapor, a spinal phase $Li_{1-x}Mn_2O_4$ has occurred on the surface of the LNMCO cathode. That the surface modification provided a good electrochemical performance and capacity to the LNMCO material has been demonstrated by the conducted analysis. The electrochemical analysis is shown in Figure 3.15 (Zhang et al., 2015).

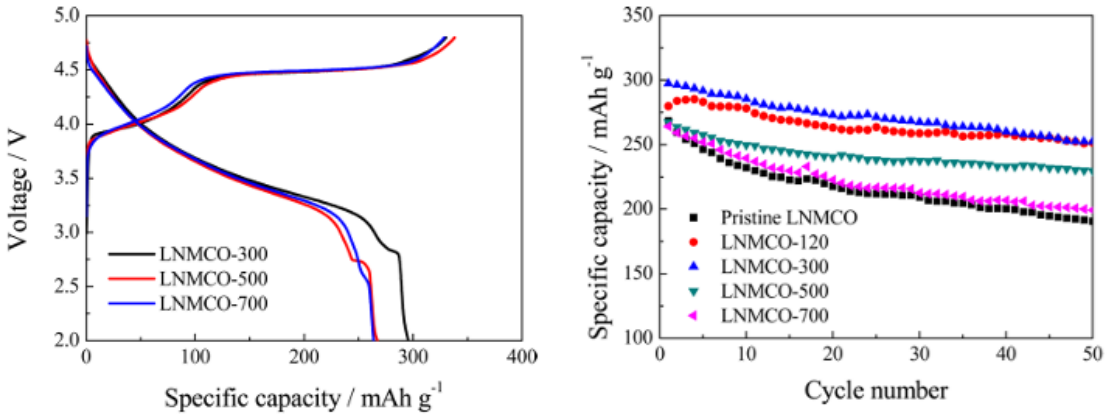

Figure 3.15. Surface modification of LNMCO cathode material (by hydrazine vapor and at different temperatures) (Zhang et al., 2015).

Graphene is a two dimensional (2D) material with sp^{2}-hybridization. It has a good electronic structure and high crystal structure. these properties differentiate it from other materials. Graphene is predominantly utilized in novel applications, especially in science and technology. Moreover, it has a great many properties such as high surface area, high thermal conductivity, good electrical conductivity, strong, and good electron transfer capability. The development of the energy conversion application and energy stroge system depends on graphene, as shown in Figure 3.25, (Gautam et al., 2023). Graphene is converted into graphene oxide (GO) by chemical oxidation. GO is widely used many applications such as battery materials, capacitors, and fuel cells etc. (Gautam et al., 2023). Ni-rich NMC cathode is an important material used in the area of lithium-ion cells owing to its high energy density and long life stability. Normally, the traditional Ni-rich NMC cathode is in the form of polycrystal structure. However, nowadays, Li et al. synthesized a large familiy of single-crystal Ni-rich NMC (Li et al., 2018).

Sun and colleagues have discussed polycrystal form NMC and single crystal form NMC, and they have compared their electrochemical properties like capacities and stabilities. The study executed by Sun et al. has shown that single crystal NMC form has a good electrochemical performance, especially this form reachs a high stability at high cut off voltage.

Figure 3.16 indicates that single crystal NMC (SC-NMC) has high stability and no degredation process at high cycle numbers in normal voltage (2,9-4,35V). Also it gets high stability, even at high voltage such as 4.9 V in Figure 3.16a (Sun et al., 2022)

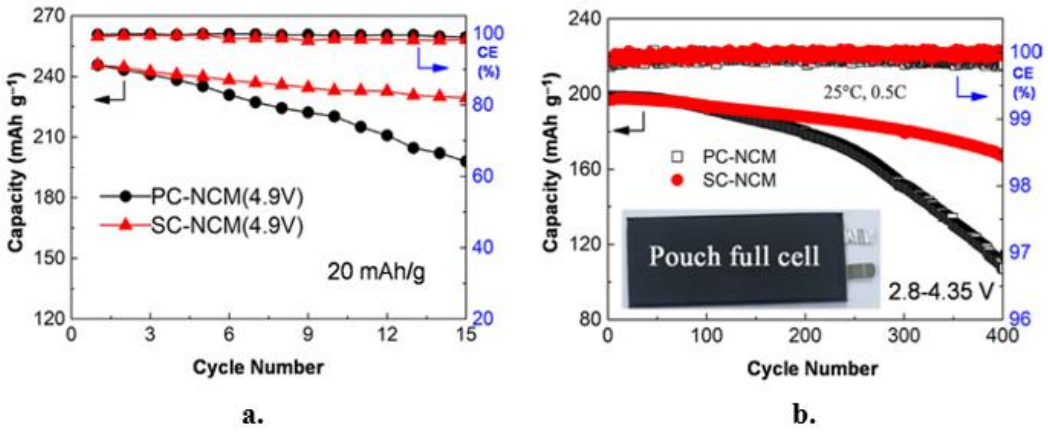

Figure 3.16. Stability comperation of polycrystal and single crystal NMC at high Voltage (a. High voltage and b. Normal voltage) (Sun et al., 2022).

Amorphous $Fe_3Co_3Ni_2$-oxy hydroxide catalyst was found to has a good electrochemical performance with Tafel slope of 49 mv/dec. Chen and colleagues, by using high-throughput aerogel synthesis, has investigated the electrochemical properties of $Fe_4Co_4Ni_2$-oxy hydroxide for oxygen evolution reaction (OER). OER catalyst, especially non-noble one, is significant for water splitting. Chen et al has found that the aerogel $Fe_4Co_4Ni_2$-oxy hydroxide exhibits a better electrochemical performance than film $Fe_4Co_4Ni_2$-oxy hydroxide. Tafel slope values of aerogel form and film form are approximetally 47.5 mv/dec and 45.3 mV/dec, respectively. Also, in the lineer sweep voltammetry (LSV) analysis, the current density of aerogel $Fe_4Co_4Ni_2$-oxy hydroxide is better when compared to film $Fe_4Co_4Ni_2$-oxy hydroxide catalyst. (See Figure 3.17) (Chen et al., 2022).

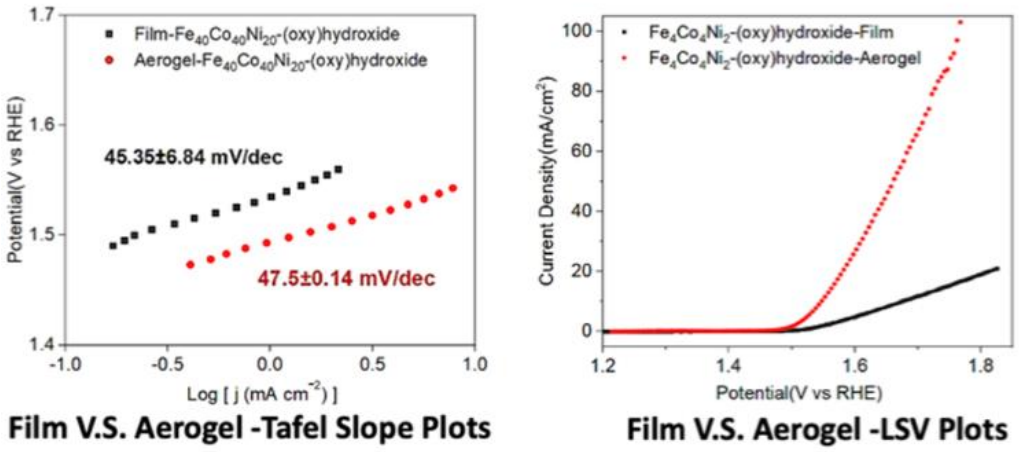

Figure 3.17. Electrochemical performance of film form and aerogel form catalyst (Chen et al., 2022).

BSCF is a significant cathode and membrane material widely used for oxygen evolution reaction and solid oxide full cells. To improve the electrochemical perfomance of BSCF, especially for SOFC, a varity of dopping agents such as Ni, Y, Zr, La, Nb, Fe, Ti, and Zn were carried out in the literature (Subhashini and Rajesh, 2023, and Wang et al., 2023).

In the literature, BSCF cathode material was synthesized by Yusoff and colleagues at different pH values. In the study, it was found that the optimum pH value to synthesize BSCF material is at pH=9 (See Table 3.2) and the optimum concentration

is 5µL (See Figure 3.18). "*The phase formation behavior of BSCF is a complex process and different in every pH tested".*was expressed by Yusoff et al.(Yusoff et al., 2013).

Table 3. 2. At different pH value for BSCF (Yusoff et al., 2013).

pH of adsorbent	S_{BET} (m^2g^{-1})	Pore size, D_w (nm)	Adsorption pore diameter (nm)	Desorption pore diameter (nm)	Pore volume (cm^3g^{-1})	Langmuir surface area (m^2g^{-1})
5	6.1	7.4	3.0	2.3	0.011	35.6
7	6.5	7.6	2.3	2.2	0.012	48.9
9	14.4	4.5	1.8	1.4	0.016	42.6

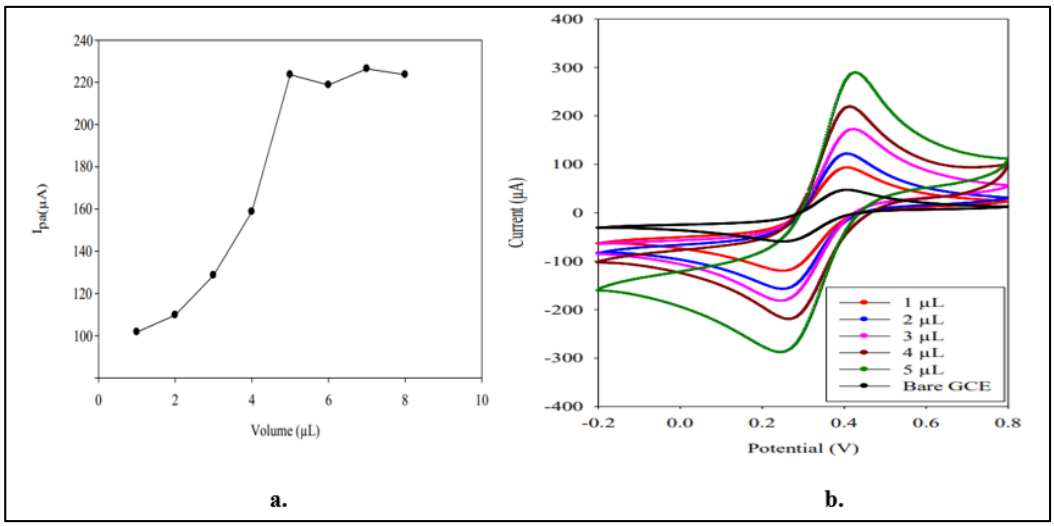

Figure 3.18. a. Anodic current at different vol. b. CV measurement at 50 mV/sec. (Yusoff et al., 2013).

However, Müller et al., by using electron microscopy, investigated that secondary phase formation in BSCF material occurred at lower 900°C. Tha phase formation is depicted in Figure 3.19. The study executed by Müller and colleagues demonstrated that the BCO (B: Barium C: Cobalt O: oxygen) type phase, the secondary phase, was precipitated from BSCF material, and the secondary phase was characterized by electron microscopy (SEM), TEM, and energy dispersive X-ray spectroscopy (EDXS) (Müller et al., 2013).

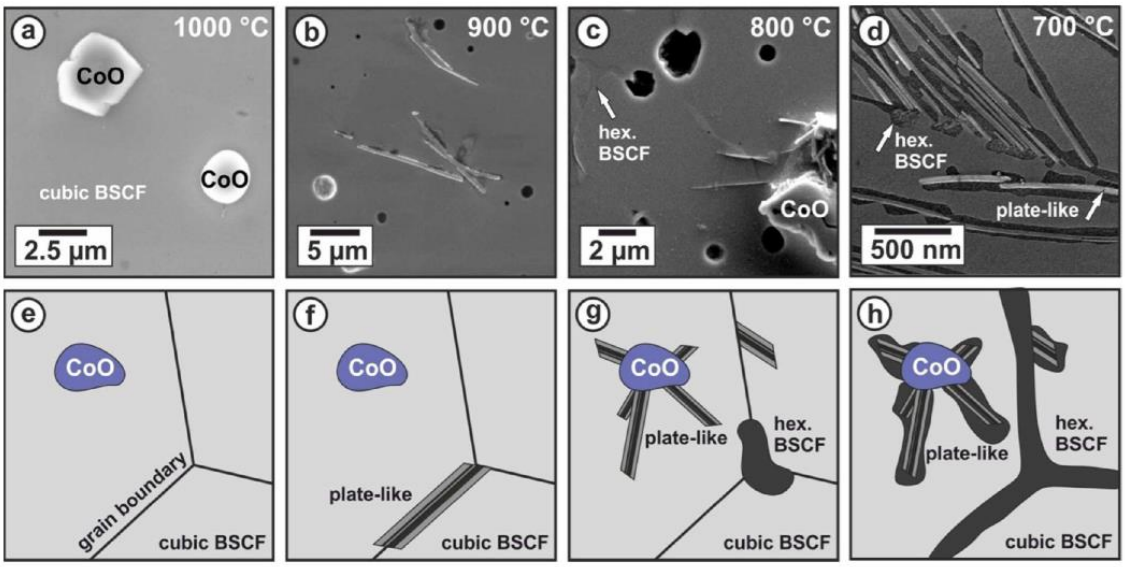

Figure 3.19. Secondary phase formation at different temperatures (SEM image) (Müller et al., 2013).

Another important topic is catalyst. A catalyst is a substance that can accelerate chemical reactions. This catalyst substance can be an atom, a molecule, an enzyme, or a zeolite. There are three catalyst types: homogeneous, heterogeneous, and bio-catalyst. Some synthesis methods like sol-gel, precipitation, impregnation, hydrothermal method, and plasma spray are used to prepare catalyst. Among traditional methods, 3D (3 Dimensional) printing method provides versatile micro and macrostructure catalsyts. Zhao and colleagues have investigated the recent development of 3D printable catalysts and have discussed the possible applications such as carbon dioxide capture and wastewater treatment (Zhao et al., 2024).

In the literature, by using 3D printing method, various catalysts were synthesized and were discussed by Zhao et al. Some examples: $NiMnO_2$ catalyst (Konarova et al., 2017), V_2O_5, ZnO_2, Cr_2O_3, Ga_2O_3 doped zeloite catalysts (Lawson et al., 2021), Ga_2O_3, Cr_2O_3, CuO, ZnO, MoO_3, and Y_2O_3 depod ZSM-5 zeolite catalysts (Magzoub et al., 2019), Cr, Cu, Ni, Y-doped H-ZSM-5 zeolite catalysts (Li et al., 2018).

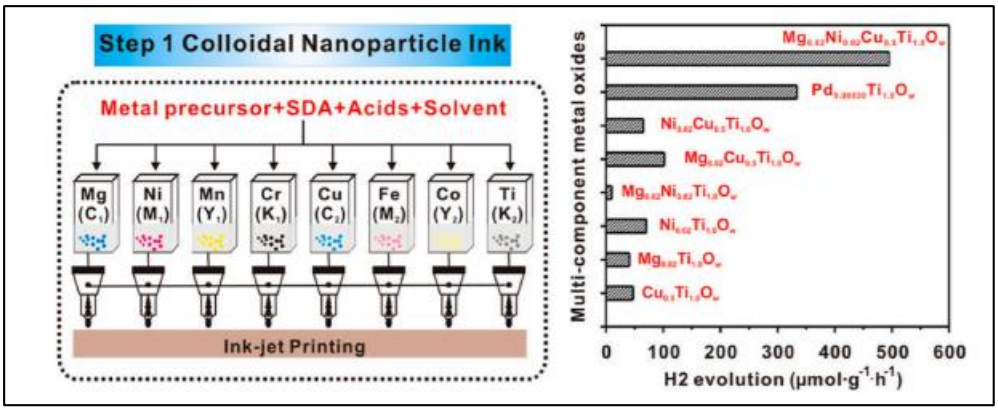

Figure 3.20. Multicomponent metal oxide synthesis (left image) and catalyst examples (right image) (Zhao et al., 2024).

Liu et al. described eight component metal oxide catalsyst synthesis, by using inject printing high-throughput technique, at a rate of 1 million per hour. Synthesis of eight-component metal oxides formulations and examples are shown in Figure 3.20 (Zhao et al., 2024 and Liu et al.,2012).

Metal oxides are widely utilized in a great amount of application, for example, batteries, photochemistry, photovoltaics, sensing and electronics. Nickel hydroxide ($Ni(OH)_2$) is prefered because of its multifunction and its practicalness in many application. Both $Ni(OH)_2$ and NiO are predominantly used in batteries, photovoltaics, water splitting, electrocatalysis, also energy storage and supercapacitors. $Ni(OH)_2$ is a semiconductor, it has 3.7-4.1 eV band gap energy. The $Ni(OH)_2$ is able to oxidise some molecules such as glucose, glycine, and methanol, also it can be used as glucose sensor in Figure 3.32 (Sánchez et al., 2023). In addition to the study of Sanchez and colleagues, Ramakrishnappa et al. have also demonstrated that nickel oxy-hydroxide is able to be used for sulfide sensing (Ramakrishnappa et al., 2024).

CHAPTER 4

EXPERIMENTAL SECTION

4.1. Required Instrumentals

4.1.1. Cyclic Voltammetry

Cyclic voltammetry is an effective technique for investigating electrochemical processes. Cyclic voltammetry is widely used in various applications like organic chemistry, electrochemistry, natural science, material science, and sensors. Cyclic voltammetry provides important information on the reduction-oxidation process, the kinetic thermodynamic parameters, and the adsorption process. In this regard, CV is often used in an electroanalytical application. CV consists of reference electrode, working electrode, and counter electrode (Chou et al., 2011).

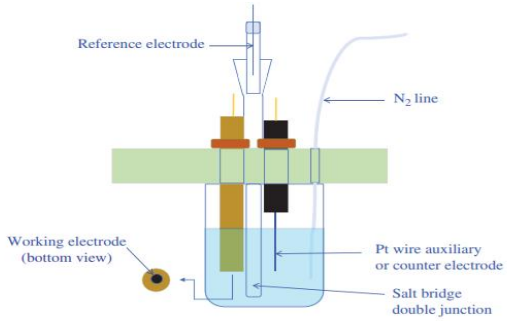

Figure 4.1. Electrochemical three cell setup (Mabbott, 2020).

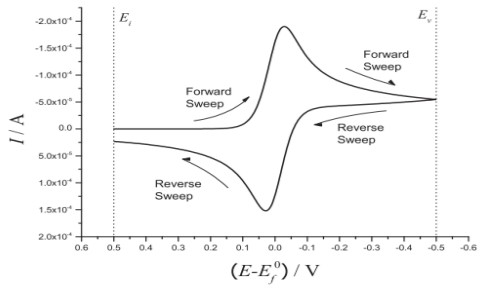

Figure 4.2. A typic voltammogram (Compton et al., 2014).

All electrochemical analyses were executed by using Metrohm CV Model:50486 in Figure 4.3. Voltamogram of oxidation and reduction peaks are shown in Figure 4.2.

Figure 4.3. Cyclic Voltammetry

The CV is a helpful tool for chemical reactions which contain electron transfer. In addition to the CV technique, there are some electrochemical techniques like differential pulse voltammetry (DPV) and square wave voltammetry (SWV) (Nainggolan et al., 2024). The SWV is used in analytical applications, electrode measures, and electrokinetic studies. The DPV is an appropriate method for investigating *in vivo* studies. The DPV method has also high affectability and selectivity (Mabbott, 2020).

The most used three cell setup for electrochemical analysis is indicated in Figure 4.1. After this, reference electrode, working electrode, and counter electrode will be abbreviated R.E, W.E, and C.E, respectively.

4.1.2. Battery Tester

Charging process is generally regulated performing a constant voltage (CV) or a constant current (CC). Sometimes both of them can be performed to regulate charging process. In the CC step, the current is mentained at a constant level (Root, 2011), see the Figure 4.4a (Althurthi et al., 2024). The CC method is commonly used in the charging protocol. In the step of CC, the galvanostatic control or current control is utilized to make easy coulomb counting for state-of-charge (SOC) (Guo et al., 2015). In the constant voltage (CV), the voltage or potential remains constant during the period of charging (See Figure 4.4b) (Root, 2011).

The CV method is widely used in the Lead-acid cells. The CV is also utilized to prevent overcharging (Guo et al., 2015). A low rate CC charging technique is suitable for Ni-based batteries such as NiCd, but not suitable for Li-based cells (Root, 2011)

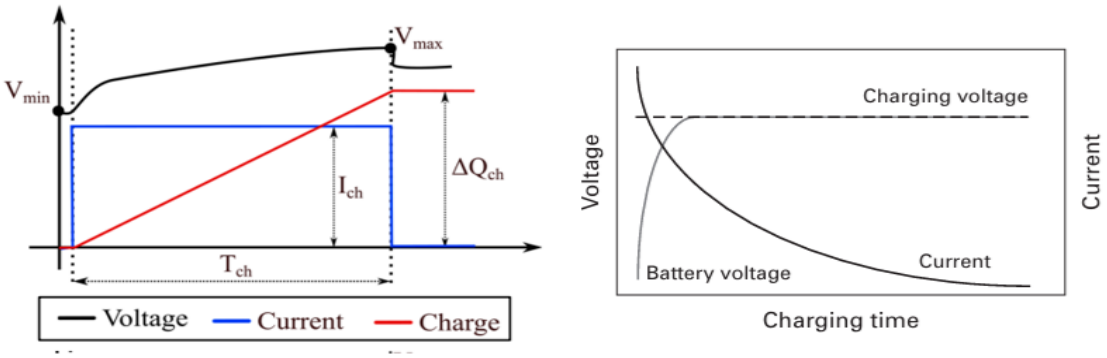

a. **b.**

Figure 4.4. Patterns of Constant Current (CC) method (a) (Althurthi et al., 2024) and Constant Voltage (CV) (b) (Root, 2011).

By combinating the CV step and the CC step, the CC-CV charging protocol method is obtained. The CC-CV method is a standard charging protocol for lithium ion batteries. The CC-CV charging technique offers nearly full battery capacity, yet this method requires more time to charge the battery (Monem et al., 2015). However, the CC-CV technique is simple and practical. Also the CC-CV protocol has been commonly utilized in many battery sector because of its convenience and practical applications (Guo et al., 2015). The CC-CV method is depicted in Figure 4.5 (Huang et al., 2020). In the CC-CV charging strategy, the battery or cell gets charged at a constant current until the voltage of battery reaches maximum value or upper limit (Keil and Jossen, 2016).

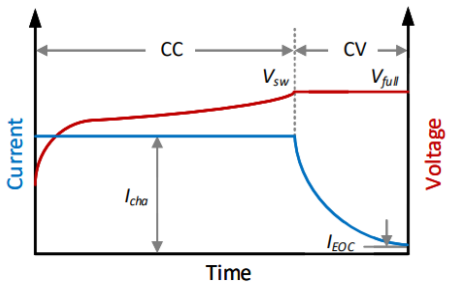

Figure 4.5. CC-CV (Constant Current-Constant Voltage) charging protocol (Huang et al., 2020).

There are the other charging protocols as well, such as multistage constant current (MSCC), pulsed charging (PC), constant current+pulsed charging (CCPC), boost charging (BC). For example, the MSCC protocol decreases application costs and do not need any software algorithms for regulation voltage (Keil and Jossen, 2016).

Capacities of all active cathode materials were tested by CT8100 5V-50mA Neware Battery Tester in Figure 4.6. Battery tester was purchased from Neware Technology Limited, China.

Figure 4.6. Battery Tester.

4.1.3. Scanning Electron Microscopy

Scanning electron microscopy (or shortly SEM) is a device which enlarges small objects to make them visible. Today, the SEM can magnify an object up to one million times from its normal size in the eyes of a human beings. Also, the SEM tool can reach 1 nm resolution power. The SEM is utilized for material characterization which gives information about surface, composition, defects in material (Ul-Hamid, 2018), the size shape or morphology, chemical composition, and crystallography. Max Knoll, a German electric engineer, showed the principle of the SEM in the year of 1935, and Ardanne developed first true/real the SEM instrument in 1938. In 1950-1960s, modern SEM tool was commercialized. (Goldstein et al., 2017). The Beam energy in the SEM is 0.1-30 kVe. To get an imaje by SEM, an electron beam, which comes from the electron gun, hits the surface of a specimen, and then the various scatterings such as an elastic or non-elastic scattering may be occurred. As results of these, a variety of signals like secondary electron, backscattered electron, Auger electron, characteristic X-ray, and photons are developed. See Figure 4.8. In an elastic scattering, the electrons are deflected in a new direction but they do not loss their kinetic energy. However, in non-elastic scattering, the

electrons are deflected in new direction and they lose and transfer their kinetic energy by interacting the specimen (Ul-Hamid, 2018). Both of them are shown in Figure 4.7.

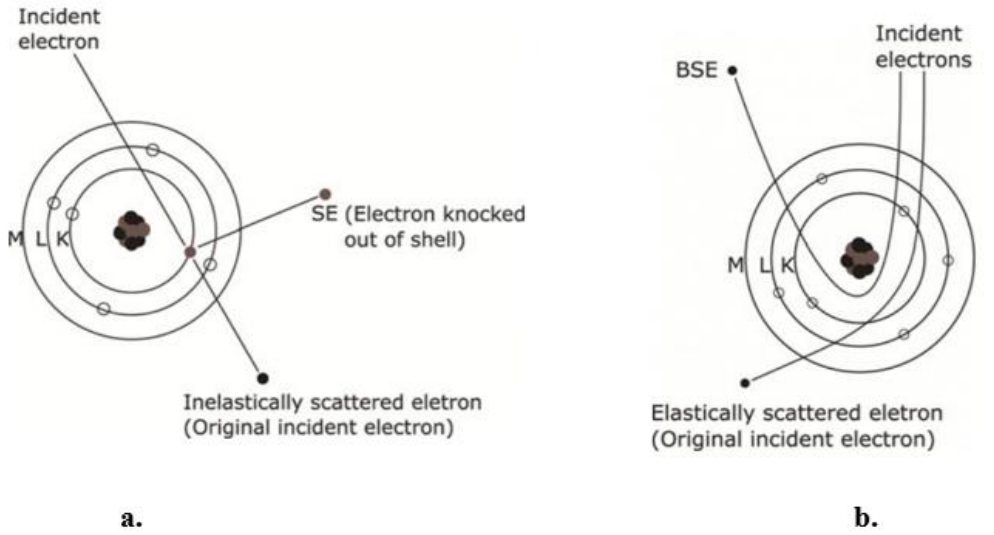

Figure 4.7 a. Non-elastic scattering model, b. Elastic scattering model in the SEM (Ul-Hamid, 2018).

A fundamental schematic flow diagram of the SEM is illustrated in Figure 3.40. The SEM contains electron gun, various lenses, detectors, processing, and computer. W (tungsten), LaB_6, and ZrO_2/W (field emission) are used as electron sources in the SEM. These electron guns or sources can be utilized for different aims and tasks to get the satisfied image (Ul-Hamid, 2018 and Goldstein et al., 2017). The cathode material and energy related materials (NMC, $Ni(OH)_2$, perovskites, semiconductors etc) are characterized and determinated their morphology by the SEM technique.

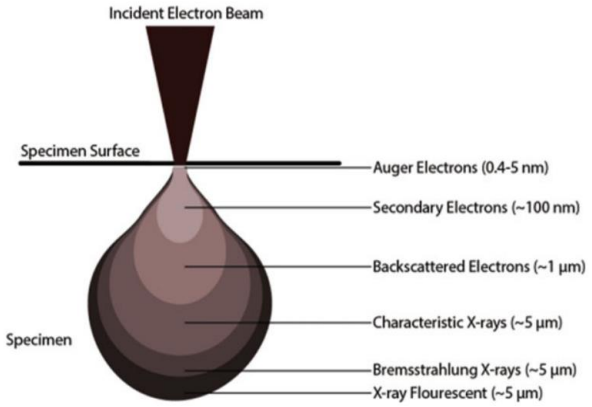

Figure 4.8. Illustration of beam electrons and specimen interactions (Ul-Hamid, 2018).

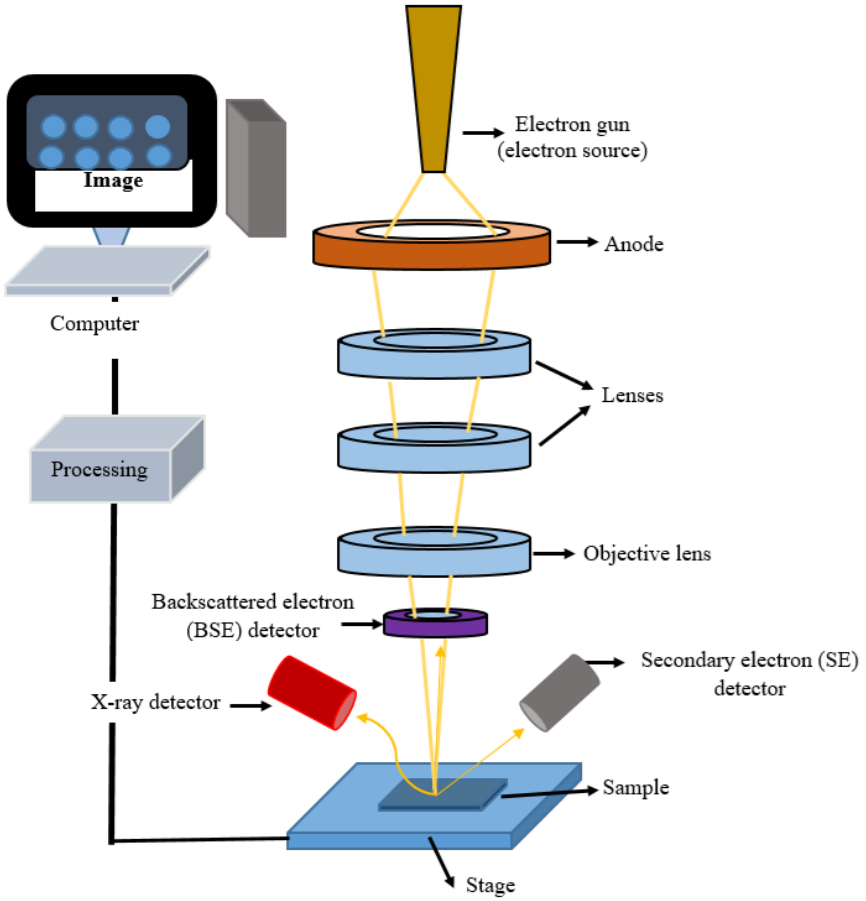

Figure 4.9. Basic block diagram of a SEM.

EDX and SEM analysis were obtained by Carl ZİESS LS20 Model SEM, resolution:5 nm, in Figure 4.10.

Figure 4. 10. General view of SEM.

4.1.4. X ray Diffraction

X-rays were first utilized by Max von Laue to determine the arrangement of atoms in crystal. He suggested that there is relationship between the ordered atoms in a crystal and an X-ray, that is, X-rays are diffracted by crystal. In 1912, W.H Bragg and W. L. Bragg expressed a new and simple formula as mathematical. They, father and son, indicated that some crystals generated intense peaks reflected by X-ray. These are called Bragg peaks (Lee, 2017). Bragg equation is given at 3.2 (equation no).

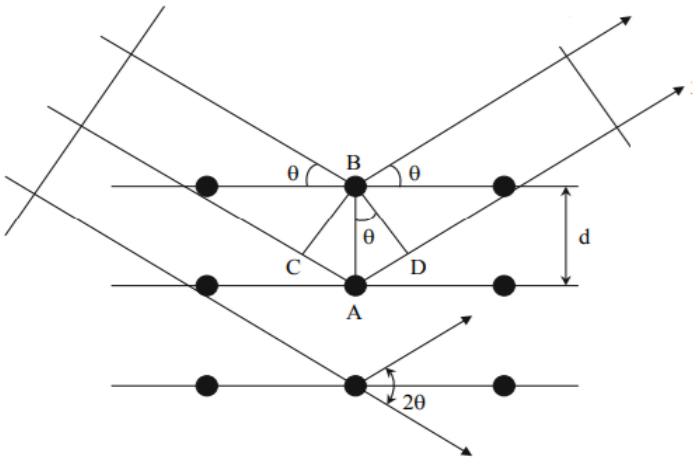

Figure 4.11. Diffraction of X-rays from crystal lattice (Lee, 2017).

$$n\lambda = 2d\sin\theta \tag{3.2}$$

here, n is an integer, d is the interplanar distance, and λ is the X-ray wavelength.

The XRD technique is utilized to investigate structure of solids (cathode material, semiconductor, perovskite etc) and collect information from the size and symmetry of solids. It can be used for the determination of phase purity of samples. By determining the peak positions in a diffraction design or motif, the shape and size of the unit cell can be figured out (Harunsani, 2013). A basic diagram of X-ray diffraction is shown in Figure 4.12.

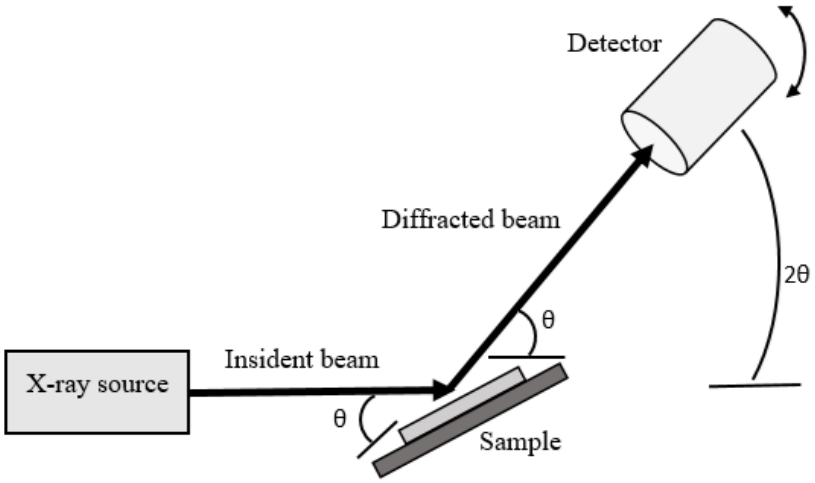

Figure 4.12. General concept of X ray diffraction (XRD).

The X ray diffraction tool has a great many application areas, for instance, in medicine, security, industrial space, and characterization and analysis of materials. Moreover, it can be applied in the food industry to analyse organic contents such as fat, organic impurities, and plastic, and even in the pharmaceutical industry (Greenberg, 2018). Another application field of the XRD is thin layer analysis studies, which is especially important for optoelectronic devices, optic devices, semiconductors, insulators, and the electronic industry (Lee, 2017).

All the samples were analysized by Philips X'Pert Pro XRD instrument at 2θ, 0.1°/s middium scan rate (photo, by permission of IZTEC Research Center)

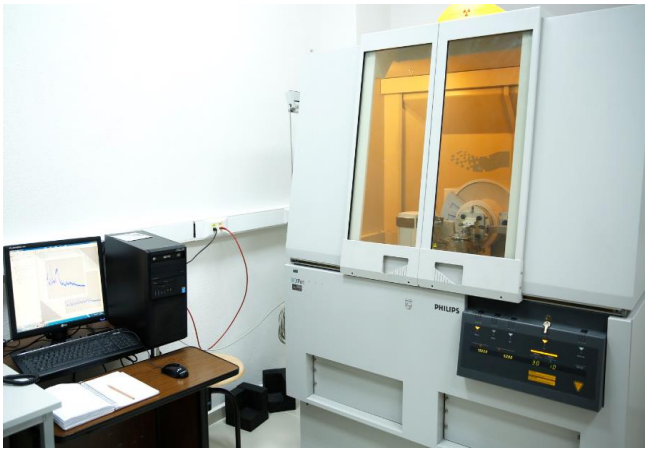

Figure 4.13. XRD instrument.

4.1.5. Another Supporting Analysis

Inductively coupled plasma optical emission spectrometry (ICP-OES) is used as a supporting tool to analyse cathode materials in the Li-based cell. For example, the analysis and the concentration of active cathode material in the lithium ion batteries have been determined by Almeida et al via ICP-OES (Almeida et al., 2019). Zhang et al. has recycled lithium from cathode material used in the Li-based cells. Formic acid-acetic acid (FA-AA) and cathode powder have been leached to get extracted all metal ions (Co, Ni, Li, Mn). All the metal ions contect in the solution have been detected by using atomic absorption spectroscopy (AAS), and they were able to successfully extract more than 95 % of lithium selectively from the cathode material (Zhang et al., 2024).

X-ray photoelectron spectroscopy (XPS) can offer the composition information of the surface of material and chemical mappings such as surface nucleation or aggregation. Shutthanandan et al.investigated the solid electrolyte interphase layer growing during charging and discharging in the lithium batteries by utilizing the XPS technique (Shutthanandan et al., 2019). Moreover, in another study, the XPS technique has been used to analyse the change of electronic structure of MoCoNi hydroxide at different voltage value (Zhu et al., 2022).

The instruments required for material characterization are summarized in Figure 4.14.

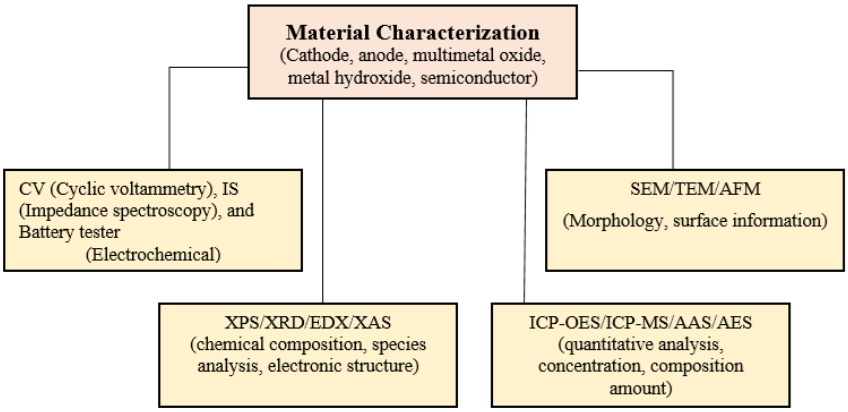

Figure 4.14. Schema analysis of material characterization.

We want to summarize instruments as supporting analysis used for characterization of materials. For example, we used ICP-OES to determine composition of NMC622, also

AAS instrument can be used to do same things. Instruments used in the material characterization are summarized in Figure 4.14.

Figure 4.15. The used viscosimeter for optimization of the printable inks.

Viscosities of printable inks were analyzed by using NDJ-1 mark viscometer in Figure 4.15. NDJ-1 is a mechanical rotational viscometer. It can be widely utilized to analyze viscosity of oil grease, paint, plastics, food, medicine, adhesive, and inks. It has the measurement range of 1-100000 mPa.s.

Figure 4.16 The used tensiometer for optimization of the printable inks.

For surface tension measurement of the printable inks, Kruss K10 ST mark tensiometer gadget was used. The used tensiometer is shown in Figure 4.16.

4.2. Required Chemicals and Materials

All chemicals were purchased from ZAG Industrial Chemicals in Türkiye, Sigma Aldrich in Germany, and some from Xiamen Aot Electronics Co. LTD, China. The list of chemicals is below;

$Ba(NO_3)_2$, $Sr(NO_3)_2$, $Ni(NO_3)_2$, $Fe(NO_3)_2$, $Cu(NO_3)_2$, $Co(NO_3)_2$ $Mn(NO_3)_2$ and $Cr(NO_3)_2$, $PbCI_2$, $Ca(OH)_2$, ZnO, $NaVO_3$, conc.HCI, acetic acid, $B(OH)_3$, EDTA(chelating, ethylenediaminetetraacetic acid, $C_{10}H_{16}N_2O_8$), citric acid (chelating agent, $C_6H_8O_7$), and ammonia (25 % w/w), F127 (surfactant, SigmaAldrich), ZnO, Zn strip (1 mm thickness), Ni foam (100PPI), urea (ZAG chemistry), KOH (Labor chemistry), ethanol (organic solvent), glycerol, PVDF, PVA, PVP, Nafion (binder, SigmaAldrich), carbon black, CMC (binder), LiPF6 (electrolyte, SigmaAldrich), and Li chips (Xiamen Aot Electronics, China).

The list of the materials is;

Ag/AgCI (reference electrode, from Xiamen Aot, China), CR2032 (coincell, from Xiamen Aot, China), PE (seperator), PP (membrane), Celgard3501 (membrane), Pt mesh (counter electrode), and some custom made aparatus.

Tap Dense-TD101 (Pharmag Instruments) tap density tester was used to determine the tap density of nickel hydroxide.

4.3. Aim and Motivation

Perovskite is in the class of the calcium titanate ($CaTiO_3$) mineral. General structure of perovskite can be symbolized as ABX_3. Perovskite can be insulator, semiconductor, and superconductor. Moreover, perovskite materials can exhibit piezoelectric, pyroelectric, ferroelectric, antiferroelectric, and paramagnetic properties. The crystal structure of these materials in the lattice can be cubic, monoclinic polymorphs, trigonal, tetragona, and orthorhombic. The BSCF play significant role in reduction-oxidation reactions. Moreover, the BSCF is utilized as an anode material. Some studies have showed that the BSCF cathode material can be used for carbon dioxide electrocatalysis. However, the BSCF can be chemically a non-stable compound under different conditions. There are different types perovskite such as BSCF, BSNF, BSZF, and BSFCu. In this part of the thesis, we have fabricated the BSCF, the silver doped-BSCF, and the novel BSNF using sol-gel method. All the characterization studies were done by using CV, SEM, XRD. For each of these compounds, the Goldschmidt tolerance factors (t) was calculated and campared. The tolerance factor (t) was first time calculated in this thesis for the Ag-BSCF and the novel-BSNF. As far as I know, there is no infromation the Goldschmidt factors (t) of both compounds in the literature.

Perovskites demonstrate piezoelectric, pyroelectric, ferroelectric, membrane, photovoltaic, antiferroelectric, and paramagnetic properties, which can offer a large study area for academic research. Especially, the Ag-BSCF and the novel-BSNF perovskites can be promising material for energy applications, such as SOFC, solar cell etc. These properties can be a motivation source to investigate these compounds.

Where, now we will discussed below headlines;

- Synthesis and Characterization of BSCF material
- Synthesis and Characterization of Ag-doped BSCF material
- Electrochemical analysis of BSCF and Ag-doped BSCF
- Result and Discussion
- Calculation Goldschmidt tolerance factor of BSCF and Ag-doped BSCF
- Synthesis and Characterization of novel-BSNF material
- Calculation Goldschmidt tolerance factor of novel-BSNF
- Result and Discussion

4.3.1 Synthesis and Characterization of Perovskite Materials

Here, metal salts: $Ba(NO_3)_2$, $Sr(NO_3)_2$, $Co(NO_3)_2$, $Fe(NO_3)_2$ and $AgNO_3$ Chelating agents: EDTA, Citric acid ($C_6H_8O_7$), and ammonia (25 % W/W). All chemicals were purchased from ZAG Industrial Chemicals in Türkiye and Sigma Aldrich in Germany.

4.3.1.1 Synthesis of BSCF Material

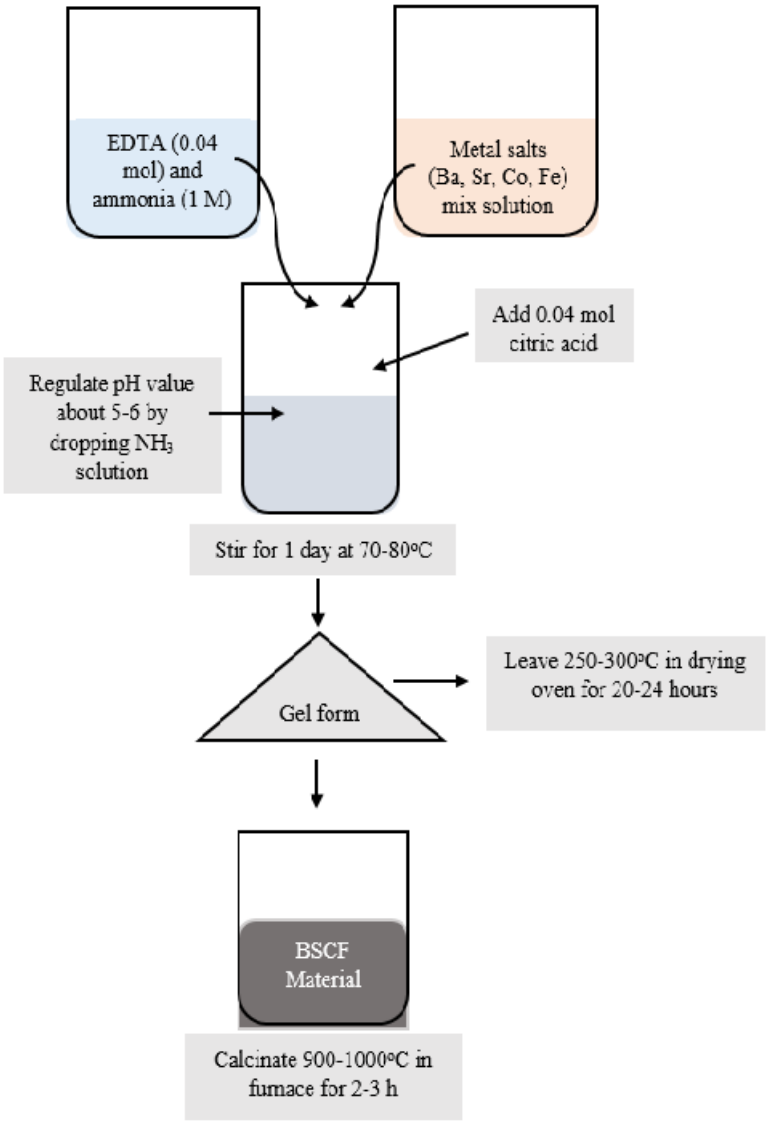

Figure 4.17. Synthesis of BSCF

$Ba(NO_3)_2$ (0.02 mol), $Sr(NO_3)_2$ (0.02 mol), $Co(NO_3)_2$ (0.03 mol), $Fe(NO_3)_2$ (0.008 mol) were prepared in 0.1 L (I. Solution). Approximately 0.04 mol EDTA was dissolved in 1 M 40 ml of ammonia solution (II. Solution). Both of the solutions were mixed, and citric acid was added. The mixed solution was regulated at pH=5-6 by dropping conc. ammonia solution. Then, the mixed solution was heated at 70-80^oC and stirred for 24 h until obtaining gel formed. Finally, the gel form was burned at 900-1000^oC at atmospheric conditions. The synthesis steps are illustrated in Figure 4.17.

4.3.1.2. Synthesis of Silver-doped BSCF Material

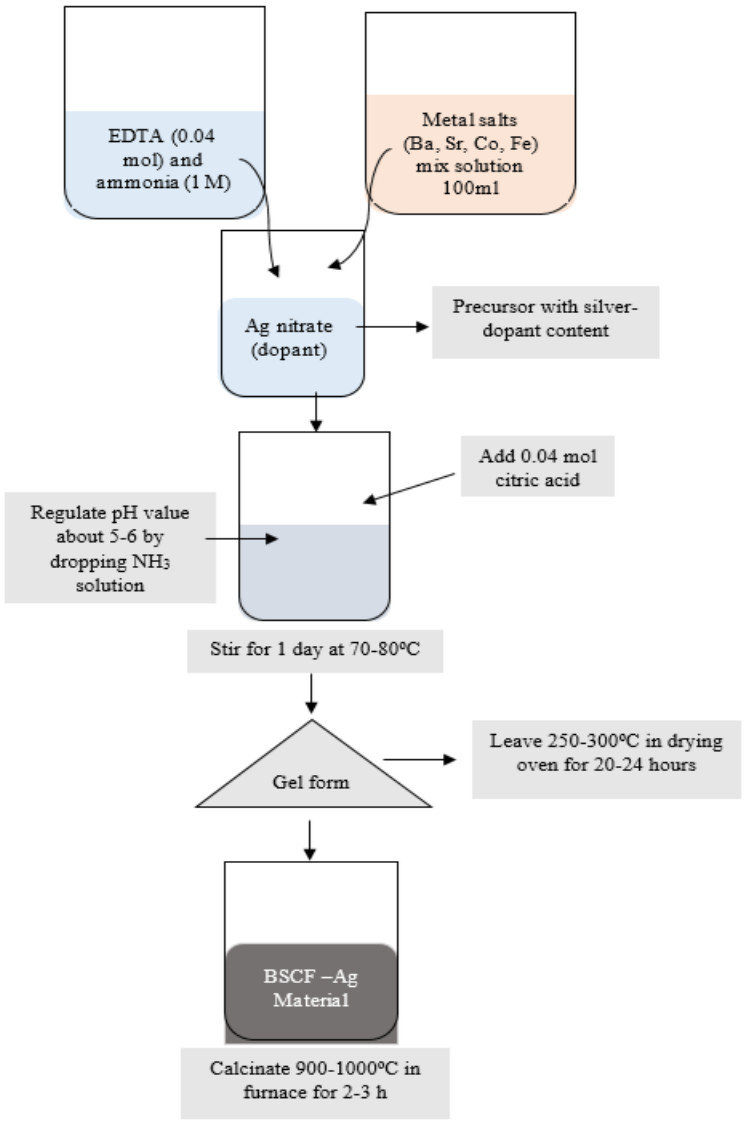

Figure 4.18. Synthesis of silver-doped BSCF.

$Ba(NO_3)_2$ (0.02 mol), $Sr(NO_3)_2$ (0.02 mol), $Co(NO_3)_2$ (0.03 mol), $Fe(NO_3)_2$ (0.008 mol) were prepared in 0.1 L (I. Solution). Approximately 0.04 mol EDTA was dissolved in 1 M 40 ml of ammonia solution (II. Solution). Both of the solutions were mixed by adding desired amount $AgNO_3$ as Ag-dopant agent, and citric acid was slowly added. The mixed solution was regulated at pH=5-6 by dropping conc. ammonia solution. Then, the mixed solution was heated at 70-80^oC and stirred for 24 h until obtaining gel formed. Finally, the gel form was burned at 900-1000^oC at atmospheric conditions. The product is silver-doped BSCF ($Ba_{0.5}Sr_{0.5}Co_{0.8}Fe_{0.2}$ $O_{3-\delta}$). The synthesis steps are illustrated in Figure 4.18.

4.3.1.3. Electrochemical and Characterization of BSCF and Silver-doped BSCF Material

For cyclic voltammetry analysis, Nafion resin solution as a binder, BSCF, and carbon black (CB) were weighed 87 mg (~100μL), 10-15 mg, 6 mg (approximately 7:3 w/w BSCF:CB), respectively. Ni foam (FTO can be used) was utilized as substrate. BSCF ink was performed on the Ni foam substrate, then dried at 80-100^oC in the oven. All electrochemical analysis was executed in 0.10 M potassium hydroxide (KOH) solution. Ag/AgCI as reference electrode (RE), Pt mesh as counter electrode (CE), and BSCF ink-Ni foam substrate as working electrode (WE) were used. The same procedure was executed for Ag-doped BSCF to perform electrochemical analysis.

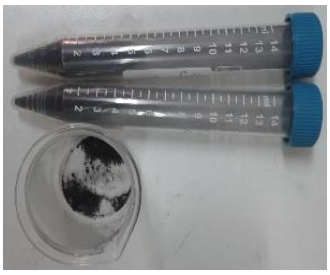

Figure 4.19. BSCF and Ag-doped BSCF samples.

The synthesized BSCF and silver-doped BSCF powder examples are seen in Figure 4.19. CV analysis setup of BSCF and Ag-doped BSCF is illustrated in Figure 4.20.

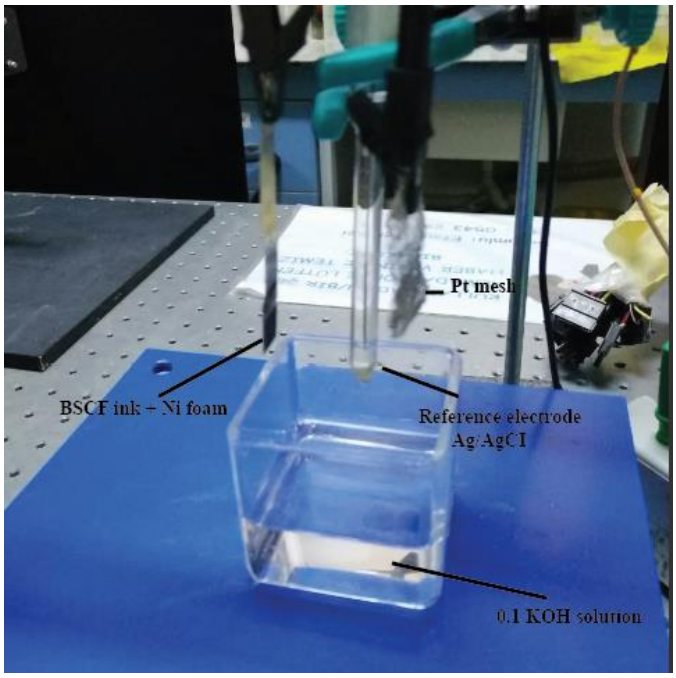

Figure 4.20. CV measurment setup of BSCF/Ag-doped BSCF material.

4.3.1.4. Result and Discussion

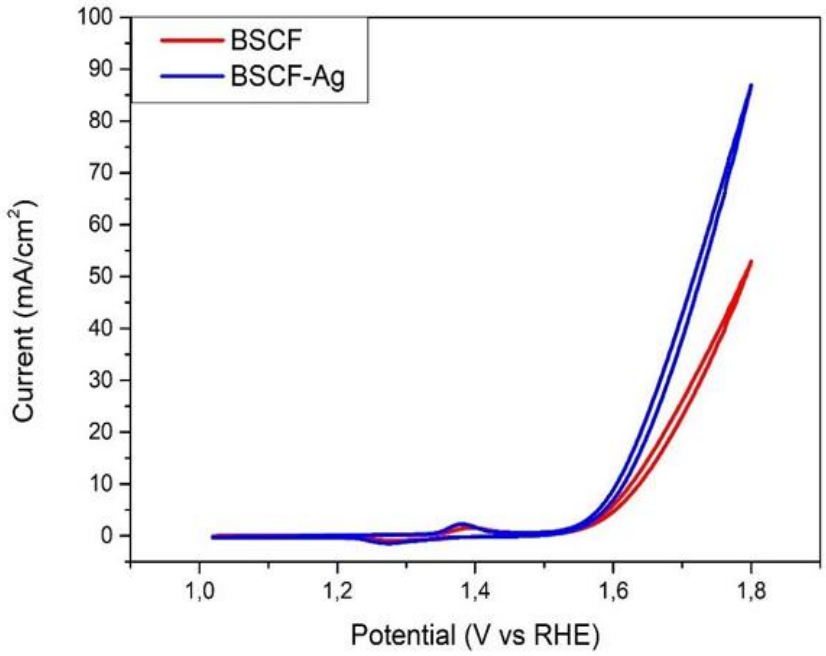

Figure 4.21. CV measurement of silver doped-BSCF (blue color) and BSCF (red color).

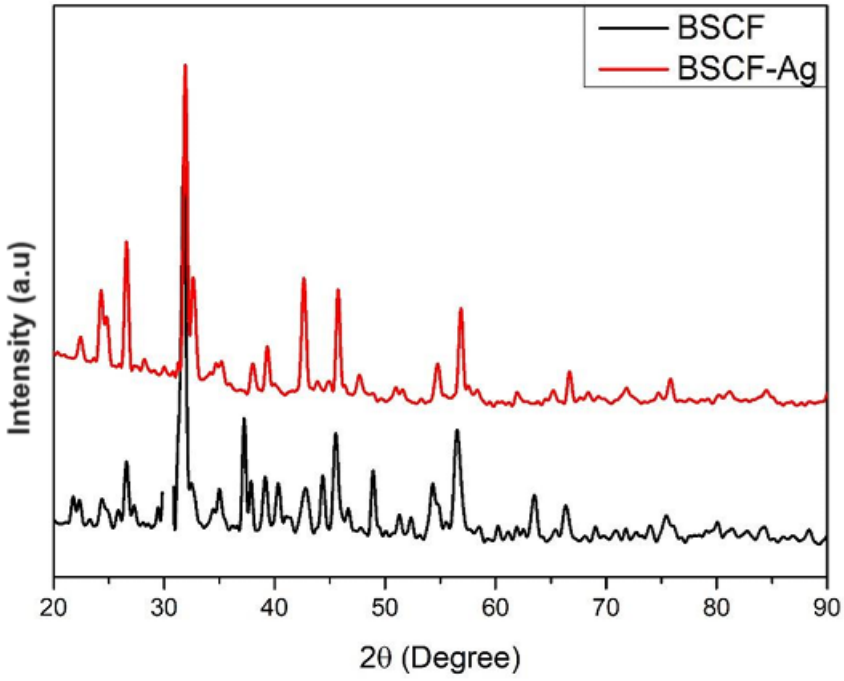

Figure 4.22. XRD patterns of silver doped-BSCF (red color) and BSCF (black color).

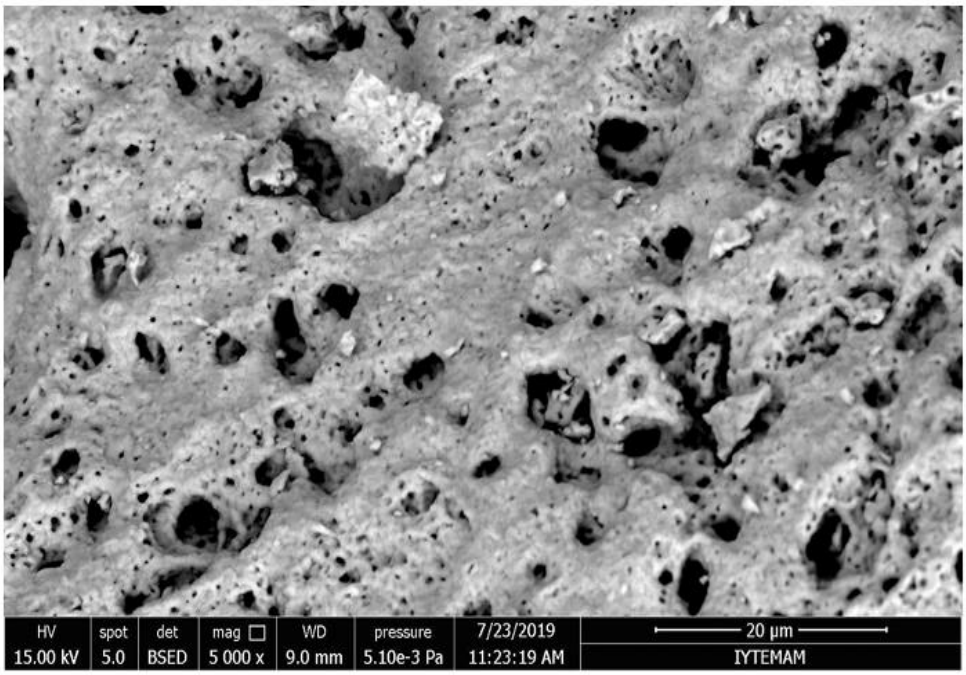

Figure 4.23. BSCF SEM image (20 µm).

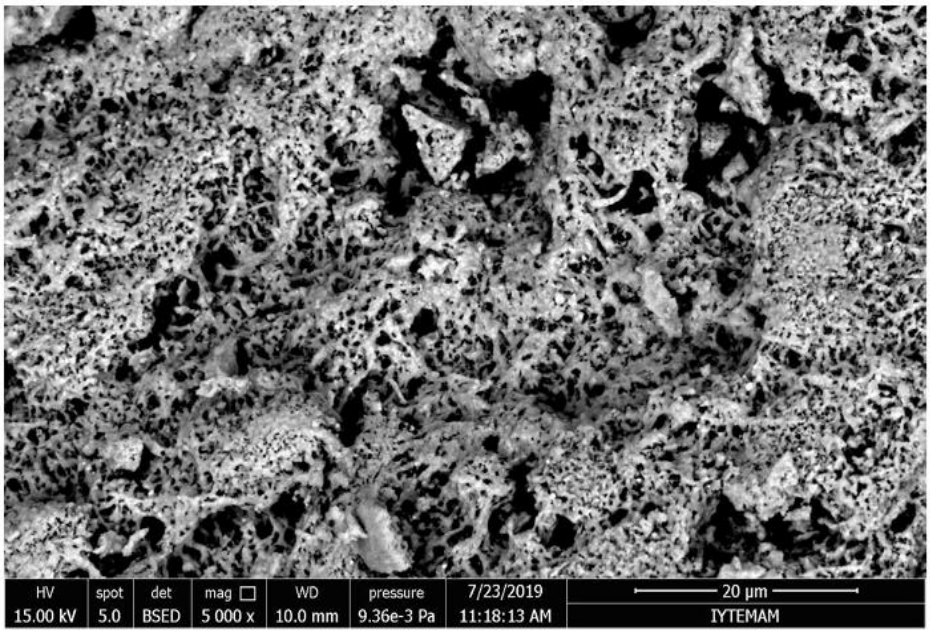

Figure 4.24. Silver doped-BSCF SEM image (20 µm).

4.3.1.4.1. Calculation Goldschmidt Tolerance Factor for BSCF and Silver-doped BSCF

Table 4. 1. A and B site ionic radius values

A side	r_A (Å)	B site	r_B (Å)	X	r_O (Å)
Sr^{2+}	1.58	Fe^{+2}	0.75	O^{2-}	1.21
Ba^{2+}	1.75	Co^{2+}	0.83	-	-
Ag^{+}	1.29	-	-	-	-

Goldschmidt Formula is given below; r_A, r_B, and r_O represent A site cations radius, B site cations radius, and oxygen ion radius, respectively.

$$t = \frac{r_A + r_O}{(r_B + r_O)\, x\, \sqrt{2}} \qquad 4.1$$

Table 4.2. BSCF and Silver doped BSCF tolarance factor values

Material	Goldschmidt tolerance factor (t)
BSCF	1.006
Ag-doped BSCF	0.901

Here, A site cation perovskite are Ba, Sr, Ag, La, Ca, Bi, Na, and K, while B site cations can be Fe, Co, Ni. X value also can be oxygen (O) and sulfur (S). For BSCF and its derivatives are accepted X value as oxygen (O).

A site and B site ionic radius values as Å (Angstrom) are shown in Table 4.1. By using these values, the Goldschmidt tolerance factors of the BSCF and the Ag-BSCF were calculated. In the literature, the Goldschmidt torelance factor is accepted between 0.75 and 1.1 for stable perovskite material (Li et al., 2024). When it is considered $0.75 < t < 1.1$ Goldschmidt factor criteria, it is seen that both BSCF and Ag-doped BSCF are in the perovskite class. The Goldschmidt factor values of the BSCF and the Ag-doped BSCF are 1.006 and 0.901, respectively, as seen Table 4.2.

Wang and colleagues investigated the stability of BSCF by building high-entropy perovskite material. They also studied on A site, B site or both sites (AB) doped high-entropy BSCF (HEBSCF), and calculated Goldschmidt tolerance factors for BSCF, HEBSCF-A, HEBSCF-B, and HEBSCF-AB as 1.02, 1.01, 1.02, and 1.01, respectively. Recently, high-entropy perovskite materials has been used to improve the stability of solid oxide fuel cell (SOFC) (Wang et al., 2022). The silver ion radius is 149 pm, which is close to Ba ion radius value. Barium is A site in perovskite system. Therefore, the silver-doped BSCF can be accepted as A site doped-BSCF (BSCF-A). Wang et al. found Goldschmidt tolerance factor slightly decreases after A-site doping process. Therefore, the synthesized Ag-BSCF perovskite exhibited a similar tendency in the tolerance factor (t) (see Table 4.2). In the literature, BSCF has a high oxygen permeation flux, and is used as membrane to seperate oxygen in SOFC. Wang et al. indicated that A site BSCF (BSCF-A) has a better stability in the oxygen permeation flux, especially 700^{o}C and 750^{o}C, than normal BSCF (sharply decrease) (Wang et al., 2022). So it can be said that the synthesized Ag-BSCF can exhibit a better performance in the oxygen permeation flux than the synthesized BSCF ($Ba_{0.5}Sr_{0.5}Co_{0.8}Fe_{0.2}O_{3-\delta}$).

The CV analysis was performed at between 1.0 and 1.8 V in the 0.1 KOH solution (see Figure 4.20). In the CV, it was observed that silver-doped BSCF has more current density than BSCF. Also, oxidation-reduction signals of the BSCF and the Ag-BSCF are slightly observed at around 1.2-1.4 V (see Figure 4.21). These signals stem from catalytically active ions (cobalt and iron ions, B site group in the perosvkite). Co^{2+} and Fe^{2+} ions or B site group involved in the catalytic performance are important for ORR and OER (Azad et al., 2018). It can be said that the Ag-BSCF has a good electrochemical performance when it is compared to the BSCF according to the obtained current density.

Ag ions were uniformly dispersed in the BSCF structure when considering the SEM images (See Figure 4.24 and Figure 4.23) and the value BET of 1.85 m^2/g. The morphology of these compounds are fine and have small particle size. Also, both structures have a porous morphology surface. BSCF has a particle size between 1 μm and 2 μm. BSCF can be around 7 μm and 9.3 μm as well, according to the used production method (Ahmadrezaei et al., 2013). Some studies show that the used synthesis method and calcination temperature can affect the particle size of BSCF. Ahmadrezaei and colleagues synthesized 40 nm particle size BSCF at 900ºC calcination temperature (Ahmadrezaei et al., 2013). Microstructure is important for fuel cell performance. Both the BSCF and the Ag-BSCF consist of aggregates of small-fine particle and occur large aggregation in the particles. According to the SEM images of BSCF and Ag-BSCF, it can be said that both are amorphous structure.

In literature, the XRD characterstic peaks of BSCF are in general seen at 20-25º small peak, 30-35º sharp peak, around 40º, 50-55º, around 50º, 65-70º, and 75-80º 2θ degree (Wang et al., 2022). In the Figure 4.22, all peaks belonging to the BSCF were observed. Extra peaks were observed 35-40 and around 45 2θ degree. It is expected that these extra peaks result from Ag ions that penetrate into BSCF crystal structure. In the Ag-BSCF, Ag peaks were also seen in Figure 4.22. This information has shown that the BCSF and doping BSCF materials was successfully fabricated. BET analysis of BSCF and silver-doped BSCF was determinated 0.77 and 1.85 m^2 per gram, respectively. The silver-doped BSCF powder shows a larger specific surface area than the BSCF powder. The specific surface area and particle size are significant to improve cathode performance, oxygen membrane performance, and the surface exchange kinetics. However, some studies related to BET surface area analysis suggest that catalytic efficiency is not limited to the surface area, so combination phases (or doping) and surface area can be responsible for better catalytic activity (Azad et al., 2018). Also, Azad et al.have shown that the porousity of BSCF causes an increase in active surface region as well as permits oxygen gas through these holes, so the porousity improves electrochemical catalytic performance for OER and ORR (Azad et al., 2018).

4.3.2. Synthesis and Characterization of Novel BSNF (Ba, Sr, Ni, Fe) Material

Here, metal salts: $Ba(NO_3)_2$, $Sr(NO_3)_2$, $Ni(NO_3)_2$, $Fe(NO_3)_2$ Chelating agents: EDTA Citric acid ($C_6H_8O_7$), and ammonia (25 % W/W). All chemicals were purchased from ZAG Industrial Chemicals in Türkiye and Sigma Aldrich in Germany.

4.3.2.1. Synthesis of Novel BSNF Material

$Ba(NO_3)_2$ (0.02 mol), $Sr(NO_3)_2$ (0.02 mol), $Ni(NO_3)_2$ (0.03 mol), $Fe(NO_3)_2$ (0.008 mol) were prepared in 0.1 L (I. Solution). Approximately 0.04 mol EDTA was dissolved in 1 M 40 ml of ammonia solution (II. Solution). Both of the solutions were mixed, and citric acid was added. The mixed solution was regulated at pH=5-6 by dropping conc. ammonia solution. Then, the mixed solution was heated at 70-80^{o}C and stirred for 24 h until obtaining gel formed. Finally, the gel was calcined at 900-1000^{o}C at atmospheric conditions. The synthesis methode of novel BSNF is similiar to BSCF synthesis.

4.3.2.2. Characterization of Novel BSNF

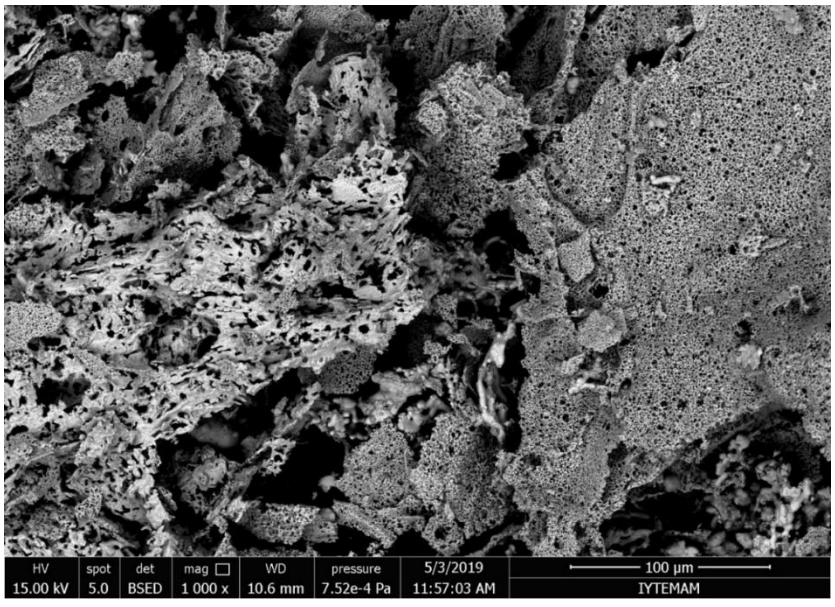

Figure 4.25. SEM of BSNF material.

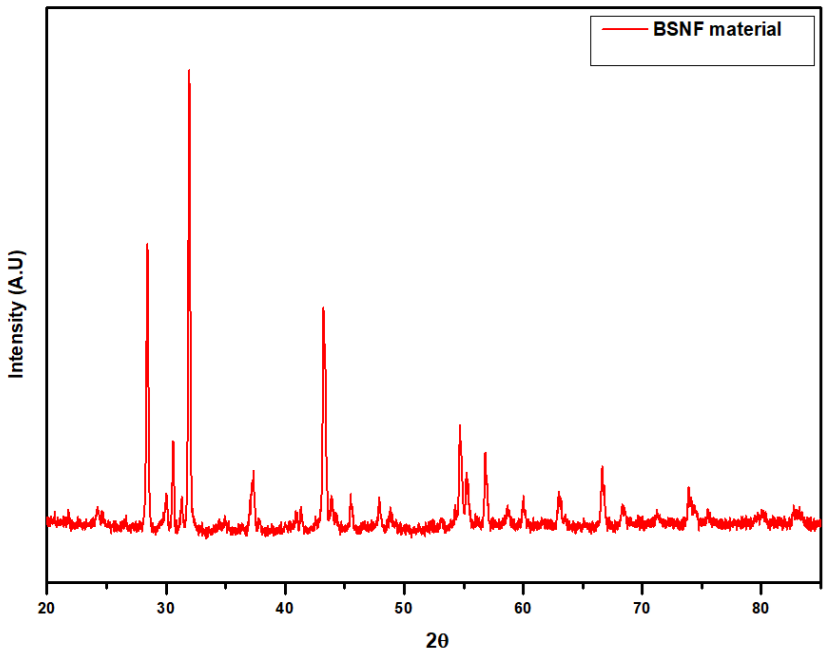

Figure 4.26. XRD of BSNF material.

4.3.2.3. Result and Discussion

As far as I know, this novel BSNF ($Ba_{0.5}Sr_{0.5}Ni_{0.8}Fe_{0.2}O_{3-\delta}$) material has not enough been discussed in the literature. The novel BSNF has been characterized by using scanning electron microscopy (SEM) and X-ray diffraction (XRD). The XRD patterns of novel BSNF are similar to the XRD patterns of BSCF. Far more research is required to characterize this novel BSNF material. Here, the electrochemical properties of novel BSNF have not discussed in the thesis. Figure 4.25 shows SEM morphology of BSNF powder after calcination. According to the SEM image, it can be said that the BSNF powder has fine, porous, and small particle size. The BSNF powder is very similar to BSCF in terms of morphology and particle size. The morphology and microstructure are crucial for fuel cell and electrochemical peroformance. Rawat and colleagues showed, by using glycine as chelating agent for synthesis, that BSNF cathode is a cubic perovskite structure *Pm3m*. In the thesis, the BSNF powder was first synthesized by using different agents (EDTA and citric acide). The XRD patterns of the novel BSNF match with peaks Rawat et al found. However, some sharp peaks (around 27.5°2θ and around 30° 2θ) are

seen in the XRD pattern. These foreign peaks can stem from phase formation or impurities. The XRD pattern of BSNF is shown in Figure 4.26.

4.3.2.3.1. Calculation Goldschmidt Tolerance Factor for Novel BSNF

Table 4. 3. A and B side ionic radius values.

A side	r_A (Å)	B side	r_B (Å)	X	r_O (Å)
Sr^{2+}	1.58	Fe^{+2}	0.75	O^{2-}	1.21
Ba^{2+}	1.75	Ni^{2+}	0.83	-	-

Table 4. 4. BSNF tolerance factor value.

Material	Goldschmidt tolerance factor (t)
Novel BSNF	0.97-1.03

Here, A site cation perovskite are Ba, Sr, Ag, La, Ca, Bi, Na, and K, while B site cations can be Fe, Co, Ni. X value also can be oxygen (O) and sulfur (S). For BSCF and its derivatives are accepted X value as oxygen (O). By using the Goldschmidt formula (see 4.1 formula number), the tolerance factor (t) was calculated for the novel BSNF.

In the literature, the Goldschmidt torelance factor, t, is accepted between 0.75 and 1.1 for stable perovskite material (Li et al., 2024). When it is considered $0.75 < t < 1.1$ Goldschmidt factor criteria, it can be said that the novel BSNF is in the perovskite class according to Goldschmidt formula. The tolerance factor (t) have been calculated 0.97-1.03 for the novel BSNF. The t factor is used to determine perovskite materials and their stability etc. The ideal Goldschmidt tolerance factor (t) is equal to 1.

I do not know whether only the Goldschmidt factor (t) is enough to define a material as perovskite, but Rawat et al.stated BSNF material as a perovskite.

The properties of the novel BSNF material, such as photoanode, photocathode, cathode material for solid oxide fuel cell, electrochemical performance, water splitting, and photovoltaic will be discussed and investigated in the further studies. As far as I know, these properties of the novel BSNF ($Ba_{0.5}Sr_{0.5}Ni_{0.8}Fe_{0.2}O_{3-\delta}$) are not addressed in the literature. This novel BSNF can be a promising material for SOFC as membrane and can be a catalyst to generate hydrogen oxygen for energy application.

4.3.3. Conclusion and Future Perspective

Perovskite materials, here the BSCF, the silver-doped-BSCF, and the novel BSNF, were successfully synthesized by using sol-gel methode and characterized. In the light of the literature, we indicated that all the XRD signals belong to the BSCFA and extra signals on the XRD refer to silver ions that penatrate into the BSCF crystal. Also, the electrochemical properties of these materials were investigated. It was shown that the BSCF with dopping silver exhibits a better electrochemical property than the BSCF. Moreover, thanks to Goldschmidt tolerance factor (t), these materials were shown in the perovskite class ($0.77<x<1.1$). It is quite obvious that novel BSNF material is corresponded to the Goldschmidt tolerance factor.

The BSCF, the Ag-BSCF, and the novel BSNF materials can be used as membrane in the solid state fuel cell (SOFC). Sensor and catalyst properties of these materials will be investigated. Their band gap energy values will be calculated by using DFT and Raman analysis to determine semiconductor properties and will be compared. Born and Phonon criteria for the BSCF, the Ag-BSCF, and the novel BSNF materials will be discussed in the future studies. In the thesis, we suggest that the silver-doped BSCF and the novel BSNF can be promising cathode materials and can be investiageted their electrochemical properies, catalytic effect, solid fuel oxide cell as seperator, and photoanode or photocathıde properties, and so on.

4.4. Aim and Motivation

Nowadays, multi-metal oxides are significant materials. These materials are widely utilized in many fields such as electronic devices, capacitors, and catalytical applications. Metal oxide materials are used to split water into hydrogen and oxygen for energy applications. Moreover, some of them can be used as pigment for paints and as additives in foods. Some metal oxides like MnO_2, NiO, Fe_2O_3, Cr_2O_3, Co_2O_3, TiO_2, RuO_2, ZnO are well known. Iron, cobalt, manganese, nickel molybdenum are profoundly studied on their catalytical activities to split water. For example, the oxide forms of Co, Zn, Ni, Mn play a good role in the electrocatalaytic activities of HER and OER. Metal oxides can consist of more one than metal and multimetal oxides, such as binary, ternary combinations can be formed for different aims (semicondutor, water splitting, electronic devices).

In the thesis, firstly, we have developed ink formulations made of Ni, Fe, Mn, Cr, Cu, and Co metals. We selected suitable organic solvent, surfactant, and other additives to get printable metal inks. For the optimization, viscosity and surface tension of the printable inks were determined and we found the viscosity and the surface tension values match with the literature information. Some pseudobinary combination oxides were fabricated from the printable inks via a modified inject printer and investigated their electrocalaytic properties for water splitting (OER). The fabricated binary multimetal oxides were widely discussed in this part.

Metal oxides are widely utilized in many applications, for example, batteries, photochemistry, photovoltaics, sensing, electronics, catalyst, and semiconductor. Also, multimetal oxides can form hundred of thousands, even millions, different metal combinations (binary, ternary, quaternary and so on). So, metal oxides can offer a vast academic research pool. To be honest, these are rather attractive for studies.

Now, here, we will discussed below headlines;

- Synthesis of printable metal inks
- Result and Discussion (optimization studies)
- Synthesis of multimetal oxide by using printable inks
- Characterization and electrochemical analysis of multimetal oxide
- Result and Discussion.

4.4.1. Synthesis of Printable Multimetal Oxide Ink

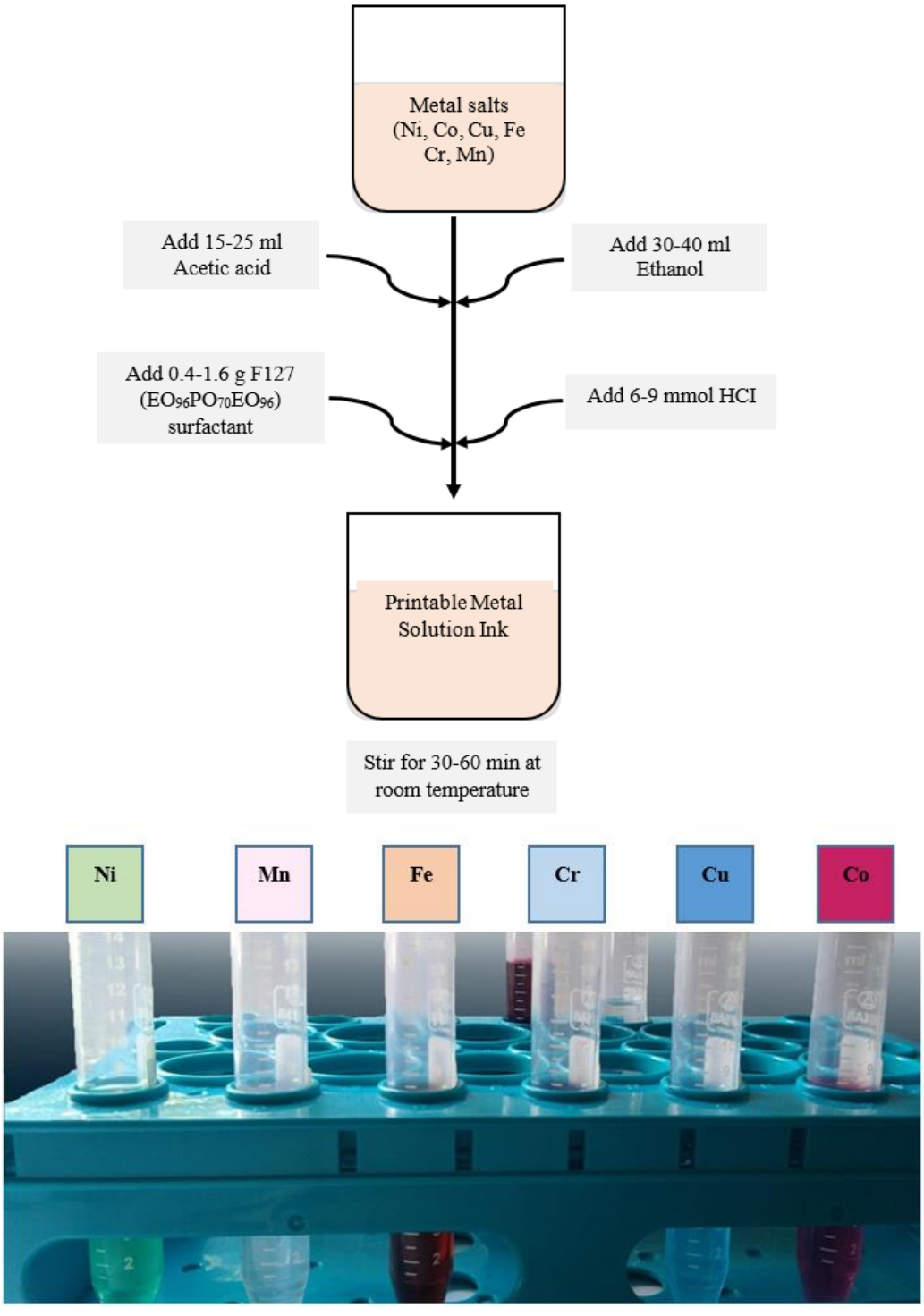

Figure 4.27. Preparetion of printable metal solution ink.

5 mmol metal nitrate salts ($Cu(NO_3)_2.2.5H_2O$, $Fe(NO_3)_2.9H_2O$, $Ni(NO_3)_2.6H_2O$, $Co(NO_3)_2.6H_2O$, $Mn(NO_3)_2.4H_2O$) were dissolved at 30 mL ethanol and 4 mL glycerol solution. Glycerol was added to arrange the viscosity of inks. Then 15-20 mL acetic acid was added to increase solubility. Finally 0.4-1.6 g F-127 as surfactant was added to the mixture. Inks solutions were stirred for 30 min at room temperature. Here, all chemicals used in the experiment were purchased from ZAG Industrial Chemicals in Türkiye and Sigma Aldrich in Germany. Chart synthesis of printable metal solution inks is depicted in Figure 4.27.

4.4.1.1. The Optimization Working of Printable Ink for Multimetal Oxide Material

Table 4. 5. Optimization of the printable ink for multimetal oxide.

1. Trial	**ml/gr**	**Result**
Glycerol (l)	0	
Acetic acid (l)	5-10	
F127 (s)	5	Not printable
Water (l)	30-25	
l: liquid /s: solid		
2. Trial	**ml/gr**	
Glycerol (l)	1	
Acetic acid (l)	4-8	
F127 (s)	2.5	Not printable
Ethanol (l)	25-30	
l: liquid /s: solid		
3. Trial	**ml/gr**	
Glycerol (l)	8-10	
Acetic acid/HCI (l)	15-20	
F127 (s)	1.6	Printable
Ethanol (l)	50-55	
l: liquid /s: solid		
Note: 10 mmol metal salts have been used for all assignments.		

4.4.1.2. Result and Discussion

Here, only Fe can be dissolved by supporting some drops HCI, but the same thing can not be said for Sr. The formulation of 3.Trial has been used to check the prepared ink for the optimization The printing of the ink on A4 paper is shown in Figure 4.28.

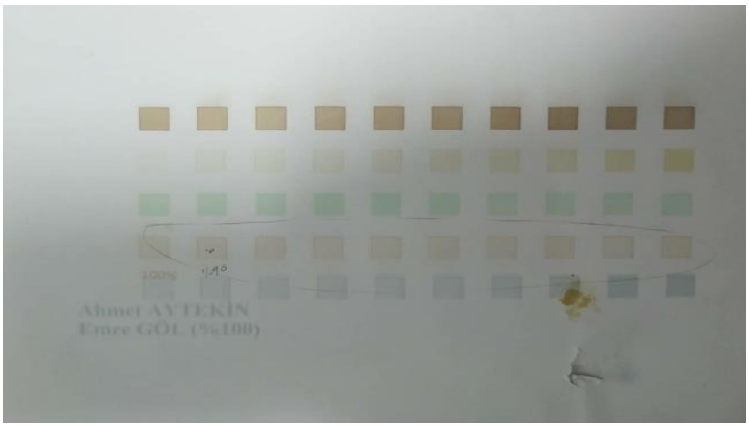

Figure 4.28. Printing example of the optimized formulation (3.Trial) (from down to up: Cr, Mn, Ni, Fe, and Co, respectively)

Here, the optimization of the printable inks has been supported by using viskozimeter and surface tansiometer devices. Viskosity analysis of the printable inks was measured via NDJ-1 mark viscometer, as seen in Figure 4.15. For surface tension measurement of the printable inks, Kruss K10 ST mark tensiometer gadget was used. The used tensiometer was shown in Figure 4.16. Strontium (Sr) ink easily clogs the nozzles on the printhead. So, the Sr ink is not suitable for printable ink. Further optimization studies are required to make printable ink of Sr. As a solution, solvents, HCI ratio, surfactants etc can be changed to improve the Sr ink. Ohnesorge number ($Z=Oh^{-1}$) is an important indicator that shows the property of a printable ink (must be $1<Z<10$) (Maleki and Bertola, 2020). Ohnesorge number of all the printable inks was calculated, and it was found that these values are between 1 and 10.

Table 4.6. The viscosity value of the printable inks

The Optimized printable ink	Cr	Mn	Ni	Co	Fe
cp(centipoise)	6.0	4.0	4.3	4.4	4.7

Table 4.7. The surface tension range of the printable inks

The Optimized printable ink	Cr	Mn	Ni	Co	Fe
Surface tension(dyn/cm)	24-27	24-27	20-26	23-27	24-28

Inkjet inks are required to perform certain factors, such as fluid dynamic and physical properties for generating stable droplets. The surface tension and the viscosity of inks are crucial to produce stable droplets, so these values must be within certain ranges (for example,10-12 mPa.s as viscosity, 28-42 mN/m as surface tension). Also, ink-substrate surface interactions affect droplet formation and droplet shape. Higher values for the surface tension can cause split and satellite droplets, while lower values for the surface tension can result in ink leakage from the head nozzle. In general, inks are Newtionian liquids and their viscosities and surface tensions must be stable. To get more stable droplets, some additives, such as polymers and surfactants are added to the ink. The surface tension and viscosity identify whether the ink is printable or not. In the printing nanoparticle ink, the particle size of NPs must be 100 times smaller than the head nozzle size to prevent NP aggregations (Lesch et al., 2015). Here, the surface tension values of Cr, Mn, Ni, Co, and Fe are summarized in Table 4.7. These values are very close to that of the literature, which shows also the printability of the prepared ink. The viscosity values of the inks (3.Trial ink) are roughly close to the values in the literature. All the viscosity measurement values of the printable ink are demonstrated in Table 4.6. After optimization ink study, the printable ink (3.Trial) was tried to check the printability of the ink on the A4 paper. From down to up square regions made from the printable ink on the A4 paper represent Cr, Mn, Ni, Co, and Fe, respectively (see Figure 4.16). 1.Trial, and 2.Trial, and 3.Trial ink are able to be printed up ot 1 day, 2-3 days, roughly 45-50 days, respectively. This study in the thesis shows 3.Trial ink is durable, stable, and has a high resistance to evaporation. However, it is hard to say same thing for 1.Trial ink and 2.Trial ink. Also, the speed of evaporation is an important factor in the formation of ink, because the evaporation affects the remaining duration of ink on the nozzle or holes in the printhead. In the literature, short-chain organic solvents such as ethanol, isopropanol, and glycol are used to prepare solvent-based inks. Such ink class is preferred to make good ink stability, suitable surface tension for ink, high viscosity, and improve evaporation rate of ink (Maleki and Bertola, 2020). As a result, suitable, stable, and printable inks were synthesized in this thesis.

4.4.2. Synthesis of Multimetal Oxide by Using Printable Ink

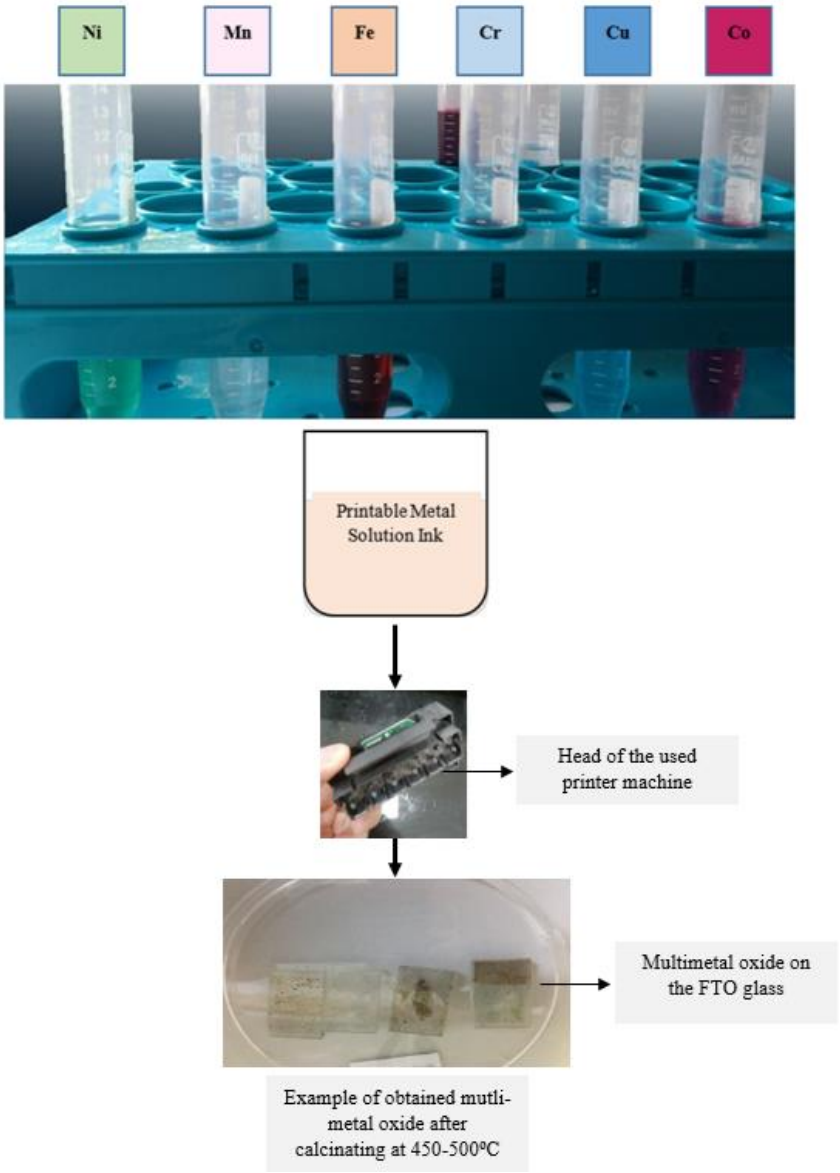

Figure 4.29. Synthesis of multi-metal oxide on the FTO glass via printer machine.

After the optimization and synthesis of the printable inks, multimetal oxide catalysts were fabricated on the FTO glass by using inkjet printer. Scheme of the synthesis of multimetal oxide electrocatalyst is shown in Figure 4.29. After printing on the FTO, the printable inks were dried at 90ºC in oven to remove volatile organic compounds. Then, the FTO glass with the inks was calcined at 450ºC in order to fabricate electrocatalysts.

4.4.3. Characterization and Electrochemical Analysis of Multimetal Oxide

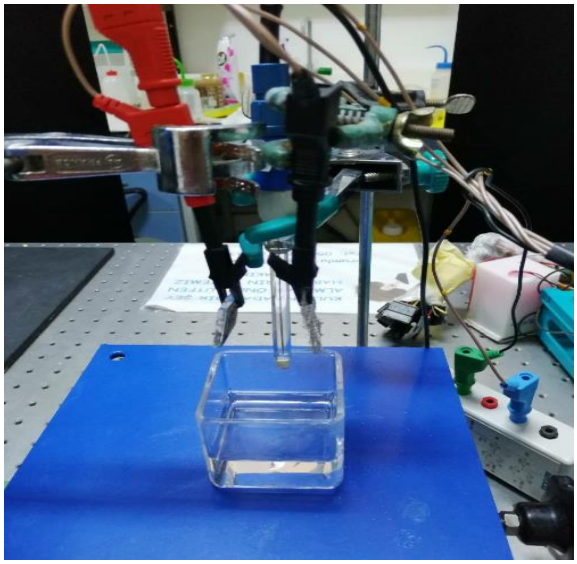

Figure 4.30. CV measurment setup of multimetal oxide

Cyclic voltammetry analysis was executed in 0.1 potassium hydroxide solution between -1.0 and 1.0 voltage. The multimetal oxide on the FTO was used as working electrode (W.E, left). AgAgCI and Pt mesh (right) were utilized reference electrode (R.E) and counter electrode (C.E), respectively. Design of CV analysis is illustrated in Figure 4.30.

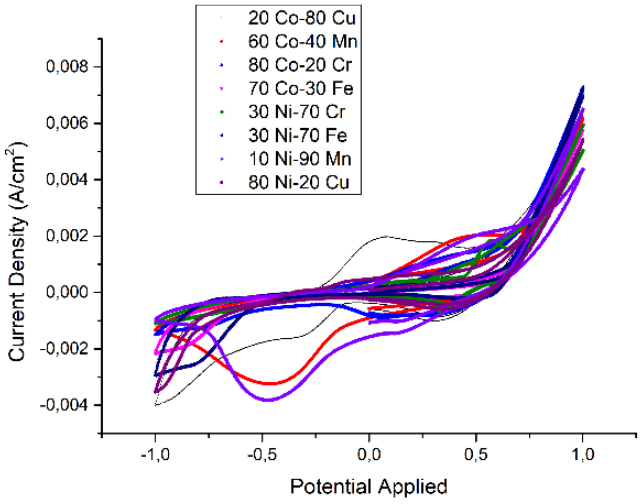

Figure 4.31. Two-combination (pseudobinary system) metal oxide CV analysis and their current density.

4.4.4. Result and Discussion

In the thesis, only two combinations or binary combinations (one metal-one metal) of metal oxide were discussed. CV measurement results is depicted in Figure 4.31. Eight different binary combination were analyzed and their current density values were compareted as current per cm squire (A/cm^2). Ni, Co, Fe, Cu, Mn, and Cr inks were synthesized at different metal ink combination ratio. Here, the multimetal oxide electrocatalysts of %20Co-%80Cu, %60Co-%40Mn, %80Co-%20Cr, %70Co-%30Fe, %30Ni-%70Cr, %30Ni-%70Fe, %10Ni-%90Mn, and %80Ni-%20Cu were fabricated at different ratio and analyzed their catalytical activity by using CV. Oxidation and reduction peaks on the CV are clearly seen, which shows the fabricated electrocatalaysts play an active role in the calayts process for oxygen evolution reaction OER. The reduciton and oxidation signals of %20Co-%80Cu, %10Ni-%90Mn, and %60Co-%40Mn are more clear and bigger than the other metal-metal oxide forms, as seen in Figure 4.31. However, Ni-Fe (%30 and %70, respecitvely) oxide exhibits maximum current density of around 7.5 mA/cm^2 compared to the other samples. Ni-Fe oxide has oxidation states of +2 and +3 for Ni and Fe respectively, which are much closer to the oxidation states in the OER region. Studies applied on Ni-Fe oxide showed that the incorporation of Fe into Ni films improves electrocatalys activity and Fe-Ni oxide can indicate up to 10 mA/cm^2 (which is close to the synthesized Ni%30-Fe%70 oxide as around 7.5 $mA.cm^{-2}$) current density at low tafel slope of 20-25mV/dec (Gong and Dai, 2015). McCrory et al. showed that $NiCoO_x$, $NiCuO_x$, and $CoFeO_x$ has promosing activity for OER, these metal oxides can also reach 10 mA/cm^2 (McCrory et al. 2013). Ni-Fe oxide, at the ratio of 1:2(Ni:Fe), is able to form nickel ferrit ($NiFe_2O_4$) that is in the cubic closed-packed structure in which Ni accopy one-eighth of the tetrahedral holes and Fe accopy half of octahedral holes. Also, Ni-Fe oxide has a high resistance to corrosion, so it gains high attractive for OER. Moreover, various studies have demonstrated that Ni-Fe oxide forms have a high catalytic property, a low overpotentail, and a low Tafel slope (Gong and Dai, 2015). Gong and Dai also discussed some metal oxides such as a-Fe_2O_3, a-CoO_x, a-$Fe_{50}Co_{50}O_x$, a-$Fe_{50}Ni_{50}O_x$, a-$Fe_{33}Co_{33}Ni_{33}O_x$ and these structures exhibited similar CV patterns to Figure 4.31 CV results. In the thesis, Co-Mn(60:40), Ni-Mn(10:90), and Co-Cr(80:20) oxide catalysts show around 6 mA/cm^2, but Ni-Cr(30:70) and Ni-Cu(80:20) indicate between 4 and 5 mA/cm^2 (see Figure 4.31). In the literature, metals show the following stability path; Re

> Os > Ir > Ru > Rh > Pt > Co > Ni > Fe > Pd > Au > Cu > Ag (Li et al., 2023). So, especially catalysts made from Co-Ni-Fe oxide combinations can exhibit a good electrocatalyst performance, which confirms the Figure 4.31. However, the Ni-Cu and the N-Cr indicated a low current density, probably because of their non-stable oxide forms with respect to the stability path (Cu low stability). Cu has a low stability, Li et al.discussed the effect of Fe and Cr on Cu catalyst and they found that Fe and Cr has a synergic effect on Cu, and Fe-Cr-Cu catalayst show excellent electrocatalyst performance and stability to generate hydrogen as fuel from methanol steam reforming (MSR), even from water gas shift (WGS) reactions due to the O_{vac}/O_{ads} (Li et al., 2023). Godinho and colleagues studied, by replacing Ni and Mn into in the cobalt ferrit $CoFe_2O_4$ in the place of Fe, the OER activity of Co-$Fe_{2-x}Ni_x$ oxide and Co-$Fe_{2-x}Mn_x$ oxide. They found that Co-$Fe_{2-x}Mn_x$ oxide has a low catalyst activity, while Co-$Fe_{2-x}Ni_x$ oxide exhibits a high electrocatalaytic property due to fact that Ni brings about the presence of the cobalt (III) ion tetrahedrally coordinated in addition to the Co^{3+} / Co^{2+} in octehedral sites, which offers an excellent catalyst for the OER. Also, Co-$Fe_{2-x}Ni_x$ oxide and Co-$Fe_{2-x}Mn_x$ oxide were found 1.5 A/cm^2 and 0.32 A/cm^2. Generally, the studies on oxides included Fe and Co show that the Co is more effective on the electrode behaviour, and electronic factors play important role in the electrode behaviour (Godinho et al., 2002). Here, in the thesis, there is a general tendency that the oxides contained Co has more curent density (at least >5 mA/cm^2) as seen Figure 4.31. Ni-Co binary oxide did not fabricated in the thesis, but the Co-Mn binary oxide was discussed, this binary oxide shows not a bad catalytic effect. Studies applied Mn oxide indicated that Mn oxide has a good calaytic performance in the oxidation of carbon monoxde, ethonal, methane, propane, and formaldehyde oxidation. This are attributed to oxidation state and oxygen storage capability in the crystal lattice. Also, the catalytic performance of Mn can be enhanced by adding some metals (Zhang et al., 2013), and the synergistic effect of between Co and Mn was discussed in various studied, and this synergistic affect plays significant role in the catalytic activity (Tang et al., 2014). Xiang et al. studied the pseudoternary catalysts of $Ni_{0.85}Fe0.1Co_{0.05}O_x$, $Ni_{0.45}Fe_{0.15}Co_{0.4}O_x$, and $Ni_{0.15}Fe_{0.35}Co_{0.5}O_x$. They investigated their electrocatalytic properties and bubble intensities for OER. $Ni_{0.85}Fe0.1Co_{0.05}O_x$ catalyst exhibited the highest bubble instensity and high electrochemical catalyst comparing to the other catalyst, Xiang's work showed that as Ni increases in the structure lattice, the electrochemical catalyst property and bubble intensity (OER) of Ni-Fe-Co oxide enhance (Xiang et al., 2014). Here, all the synthesized metal-metal (binary) oxides are pseudo

binary systems, because the pseudo binary oxides were not characterized to determine true binary combination. Only the CV analysis was applied to determine the catalytic activity of the pseudobinary oxides for OER. The water bubbles were observed during the experiment, but the bubble intesities were not calculated. Considering that the stability order of the metals (Co>Ni>Fe), many studies showed that Co, Fe, and Ni generally can exhibit a good catalytic performance in the different binary or ternary systems. However, depending on metals incorperated into the structure lattice, they may have different catalytic effects. For example, the electrocatalytic activity of $Ni_xFe_yCo_zO_m$ (x,y,z,m random ratio) oxide deponds on x, y, x mol ratios. The effect of mol ratios on the calaytic activities was demonstrated by Xiang et al. Also, synergetic effect (Mn, Cu, Cr etc) in the calaytic studies plays crucial role in the electrocatalytic acitivity and stability of binaray or ternary systems. Guevarra et al. showed that Mn is instable in the catalyst and it brings about corrosion in the catalyst system. Also they invesitgated the electrocatalytic activity of Ni-Fe-La trenary oxide, they indicated that this oxide exhibits an excellent catalytic performance compared to Mn-Ni-Fe oxide (Guevarra et al., 2022). Baeck et al studied that tungsten (WO_3) oxide, a low electrical conductivity, can show significantly improved photovoltaic performance by doping with Ni, but can not get same effect by doping with Cu, Co, Zn. Probably, Ni can increase the conductivity and decrease charge carrier recombination in the tungsten oxide (Beack et al., 2002). Woodhouse and Parkinson in their article catagorized metals and their oxides; light adsorbing: Fe, Cr, Co, Ni, Cu, V, Mn, and Ce, catalytic: Rh, Ru, Pt, Ni, Pd, Ir, Os, Re (Woodhouse and Parkinson, 2009). Therefore, numerious factors affect (dopant, calnication temperature, light, synergetic effect, conductivity, medium(acid or base, for example IrO_2 catalyst, its max performance in basic medium), charge, oxidation munber, combination systems, such as binary, ternary etc.) the electrocatalytic activity and stability of metal-metal oxides for OER and ORR. As a result, the synthesized Ni-Fe oxide catalyst shows maximum current density, then the oxides containing Co (Co-Cu, Co-Mn, Co-Fe,Co-Cr) exhibit moderate current density, while the synthesized Ni-Mn and Ni-Cu demonstrate the lowest current density in this study.

4.4.5. Conclusion and Future Perspective

In this part of the thesis, three ink formulations have been developed to fabricate multi-metal oxides for catalayst, especially water spitting to generate hydrogen gas for energy. Three trials were executed to optimize the inks. Also, for optimaztion of the inks, the viscosity and surface tension were measured. It was shown that “Third trial” was printable ink. This ink were used in the all synthesis of mutli-metal oxides. pseuodbinary combination metal oxides on the FTO as substrate were printed by using inkjet printer machine. Pseudobinary combinations (Co-Cu, Co-Mn, Co-Cr, Co-Fe, Ni-Fe, Ni-Mn, Ni-Cu) were synthesized and discussued. Among the fabricated pseudobinary combinations, the Ni-Fe (%30-%70) binary combination exhibited maximum current density (about 7.5 $mA.cm^{-2}$), but the pseudobinary combination of the Ni-Cu and Ni-Cr showed minimum current density. We found that the binary combination systems made of Co, Ni, and Fe generally exhibit high current density,which matchs with stability range of Co>Ni>Fe. Moreover, we showed that the printable inks (3.Trial formulation) fit in ohnesorge number (1<Z<10; Z:Ohnesorge number).

In the future studies, the hundred of thousands multimetal oxides can be simultaneously synthesized for water oxidation and sensor applications and can be profoundly investigated their electronic structure to figure out catalytic mechanism in the fabricated metal oxides. Binary, ternary, and quaternary oxides will be fabricated and compared and their electrocatalytic activity will be investigated for OER and ORR studies (CO converting CO_2 ,generation hydrogen gas from methane, etc)

4.5. Aim and Motivation

Nickel hydroxide is a significant cathode material used in Ni-Zn batteries. There has been an increase in studies on developing cheaper synthesis methods and improving the performance of nickel hydroxide cathode material. Nickel hydroxide is used as the positive electrode for rechargeable alkaline batteries, such as Ni-Zn, Ni-Cd, Ni-MH (nickel-metal hydride) and Ni-Fe. Nickel hydroxide is clean, high-capacity, inexpensive, and safety. Nickel hydroxide has two polymorphs: one is α-$Ni(OH)_2$ and the other is β-$Ni(OH)_2$, that in the oxidation phase change into γ-$Ni(OH)_2$ and β- $Ni(OH)_2$, respectively. Various methods, such as urea decomposition or hydrothermal, hexamethylenetetramine (HTM), sonochemistry etc. can be used to synthesize $Ni(OH)_2$ cathode.In this thesis, urea decompositon methode has been used to fabricated nickel hydroxide and M-(M: Cu, Al, Zn, Co)doped-$Ni(OH)_2$. We synthesized alpha and beta nickel hydroxide and we characterizated them by using XRD, SEM, and CV. The capacitance (F/g) of M-doped-$Ni(OH)_2$ were calculated. For the optimization studies, we have used a reference cathode material (commercial product) to provide the optimization conditions. After the optimization, we used the Co doped-β-$Ni(OH)_2$ to determine its specific capacity. C rate effect, binder affect, electrolyte effect on the capacity of cell were profoundly discussed as well. Nickel hydroxide is eco-friendly, cheap, safe, and abundant, and nickel hydroxide exhibits a high theoretical capacitance, pseudocapacitive, electrocatalyst, supercapacitor, active cathode material, and electrochemical sensor properties. So, it can offer a large study area for energy applications and academic research. Doping and optimization studies to improve the capacity of beta-nickel hydroxide as cathode material are quite attractive as well. These factors have motivated us to study on the nikel hydroxide and its optimization.

Now, here, we will discussed below headlines;

- Synthesis of nickel hydroxide
- Synthesis of Co, Cu, Al and Zn doped-Nickel Hydroxide
- Electrochemical performance of Co, Cu, Al and Zn doped-$Ni(OH)_2$
- Result and Discussion
- Fabrication of anode-cathode and optimization study for capacity
- Result and Discussion
- Process of the optimization preparation (C rate, binder,and electrolyte).

4.5.1. Synthesis of Nickel Hydroxide Cathode Material

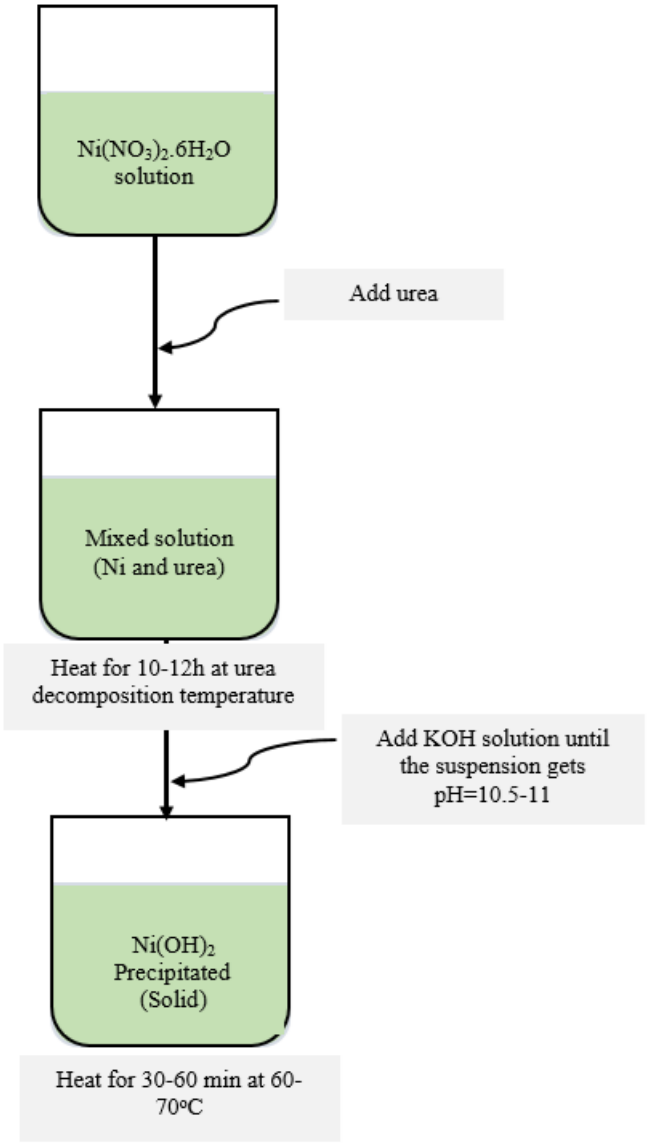

.Figure 4.32. Synthesis of $Ni(OH)_2$ cathode material.

Nickel hydroxide as cathode material was synthesized by using urea decomposition method. 0.1 mole $Ni(NO_3)_2.6H_2O$ and 0.25 mole urea (CH_4N_2O) were dissolved in distilled water and stirred for 10-12h at 95-100ºC. After aging in alkaline media (KOH or NaOH), formed $Ni(OH)_2$ was filtered and washed with hot distilled water, and then dried at 70-80ºC in the oven. Diagram of synthesis is shown in Figure 4.32. All chemicals used in the experiment were purchased from ZAG Industrial Chemicals in Türkiye and Sigma Aldrich in Germany. The setup is illustrated in Figure 4.33.

Figure 4.33. Experiment set-up for synhtesis nickel hyroxide.

Figure 4.34. Photo of obtained nickel hydroxide product.

4.5.2. Synthesis of Co, Cu, Al and Zn doped-Nickel Hydroxide Cathode Material

Nickel hydroxide was synthesized by using urea decomposition method. 0.1 mole $Ni(NO_3)_2.6H_2O$ and 0.25 mole urea were dissolved in the distillate water stirred for 20-30 min at room temperature. After being dissolved, the reaction was stirred at 95-100^oC temperature for 10-12h. Formed α-$Ni(OH)_2$ was doped with transition metal salts such as Co, Zn, Al, and Cu (nitrate form). Then, the prepared KOH solution was added to the reaction until pH value is 10.5-11. The reaction was filtered, washed with hot distilled water, and dried at 70-80^oC in the oven.

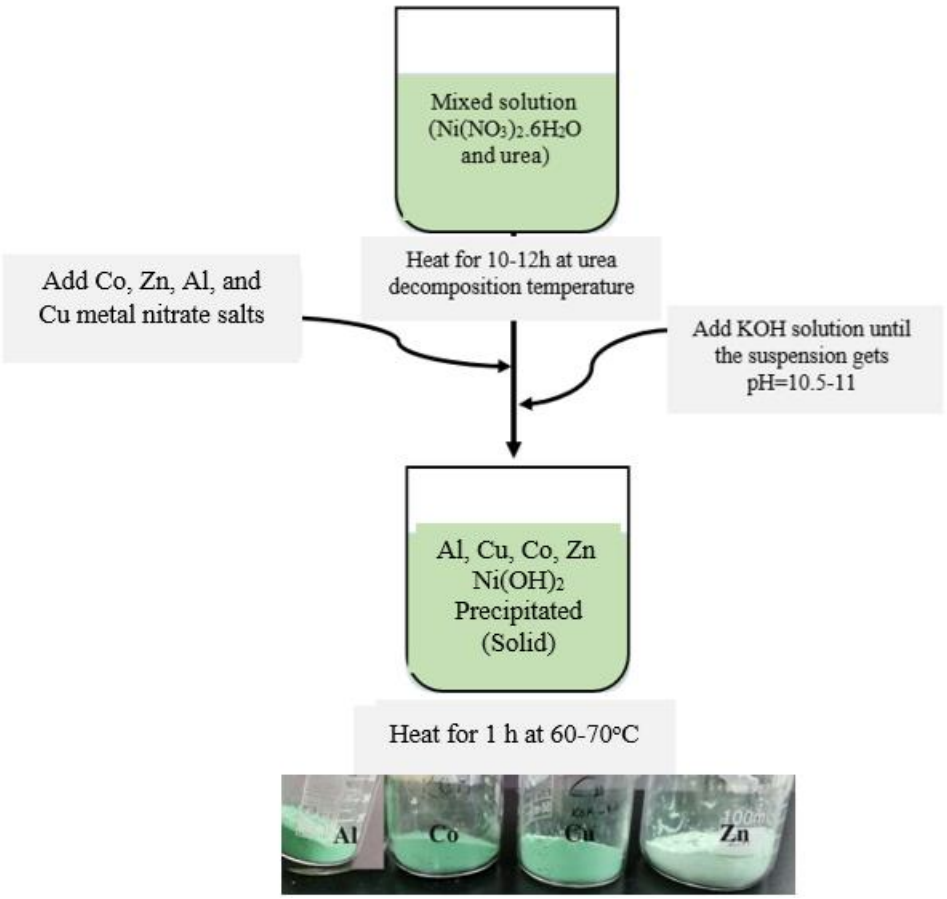

Figure 4.35. Synthesis of Zn, Co, Cu, Al doped-$Ni(OH)_2$ cathode material.

The scheme of the synthesized Zn, Co, Cu, Al doped-$Ni(OH)_2$ is illustrated in Figure 4.35, and the synthesized products were photographed. Urea decomposition method or hydrothermal method was used to synthesize nickel hydroxide. This method is cheap, easy, and accessible, so this method was selected for synthesis. There are also various methods for synthesis In the first phase, the alpha-nickel hydroxide form was developed, then, by adding KOH solution (3-4 M) to this form, the beta-nikel hydroxide was fabricated. In the literature, the β-$Ni(OH)_2$ is generally accepted as cathode due to its high stability. Here, all the Zn, Co, Cu, Al doped-$Ni(OH)_2$ cathode materials were successfully synthesized.

4.5.3. Electrochemical Performance of Co, Cu, Al, and Zn doped-Nickel Hydroxide Cathode Material

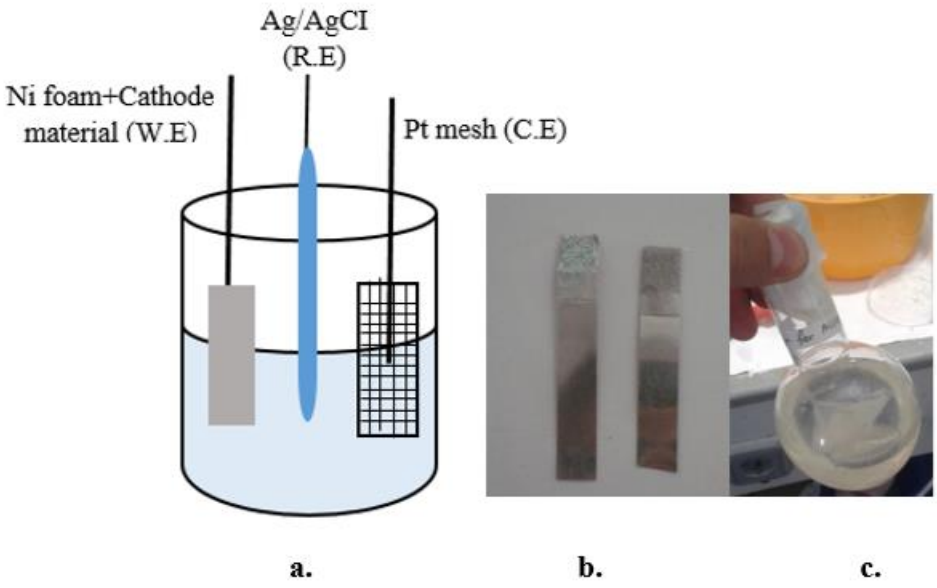

Figure 4.36. **a.** Electrochemical cell **b.** Ni foam substrate **c.** Binder.

For binder, approximately 17 g of PVA (polyvinyl alcohol) and 3 g of PVP (polyvinlypolypyrrolidone) have been dissolved 30-35 ml of hot distilled water. The binder has been supported by some potassium hydroxide (3-4 M KOH). Then, the binder was strirred for 1-2 h at 90-95^{o}C.

For the preparation of nickel hydroxide cathode material, 800 mg of $Ni(OH)_2$ cathode, 100 mg of carbon black (C.B), and 100 mg of the binder were mixed for 2-3 h at room temperature. After preparing the cathode material, it was loaded on nickel foam as substrate. The loaded amount was 180-200 mg. The same preparation procedure was executed for ,Zn, Co, Cu, and Al doped-$Ni(OH)_2$ to do electrochemical analysis.

For electrochemical measurement of the cathode material, $Ni(OH)_2$ on the Ni-foam, Pt mesh, and Ag/AgCI were utilized working electrode (W.E), counter electrode (C.E), and reference electrode (R.E), respectively. CV analysis was perfomed at between -0.1 and 0.5 V.

4.5.4. Result and Discussion

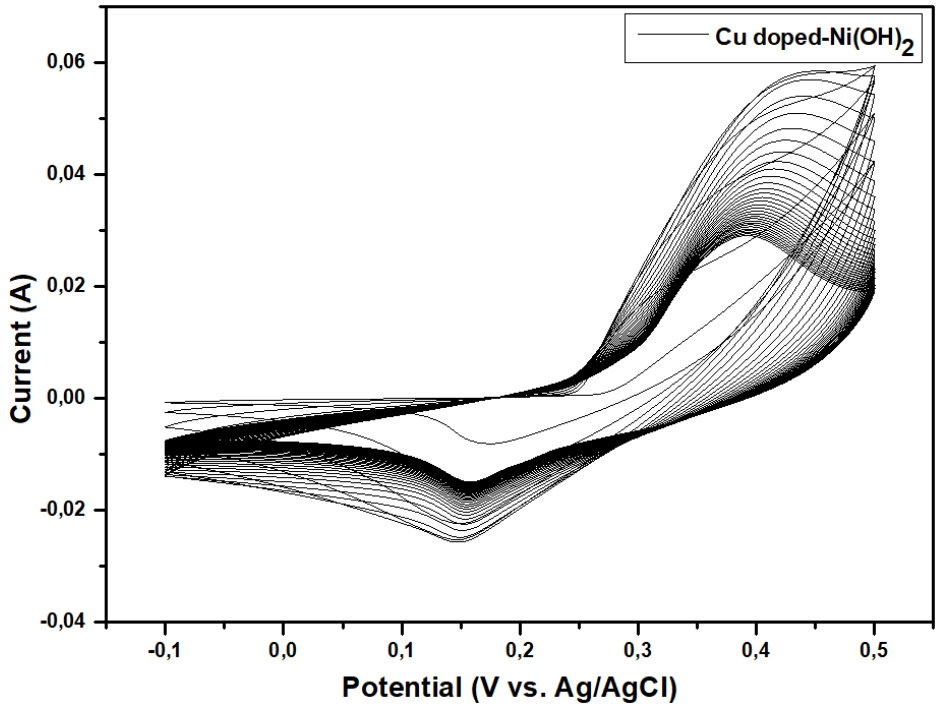

Figure 4.37. CV analysis of Cu-doped $Ni(OH)_2$.

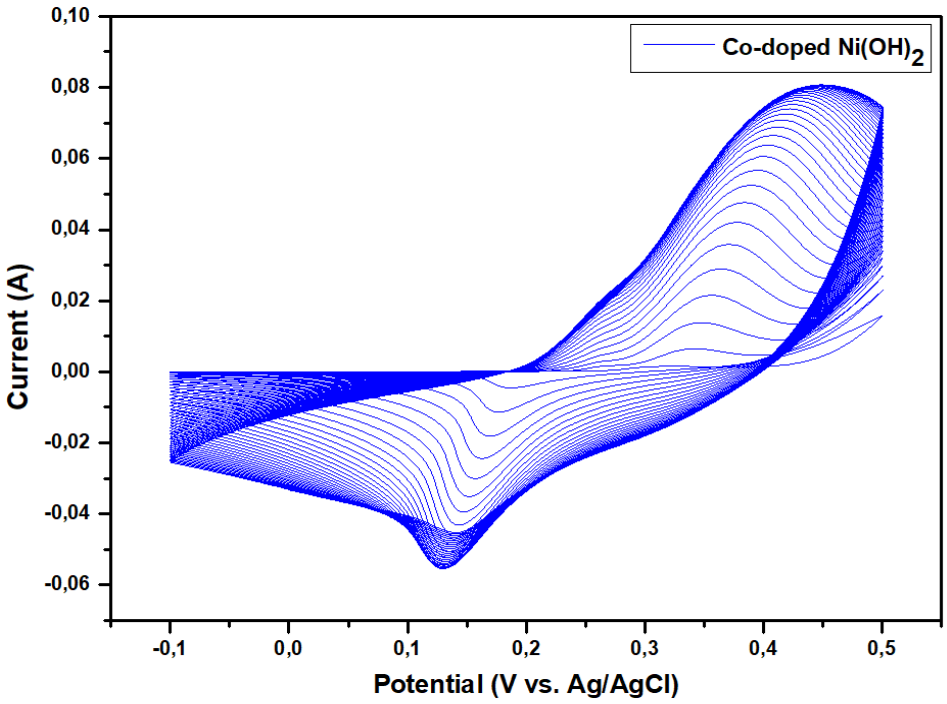

Figure 4.38 CV analysis of Co-doped $Ni(OH)_2$.

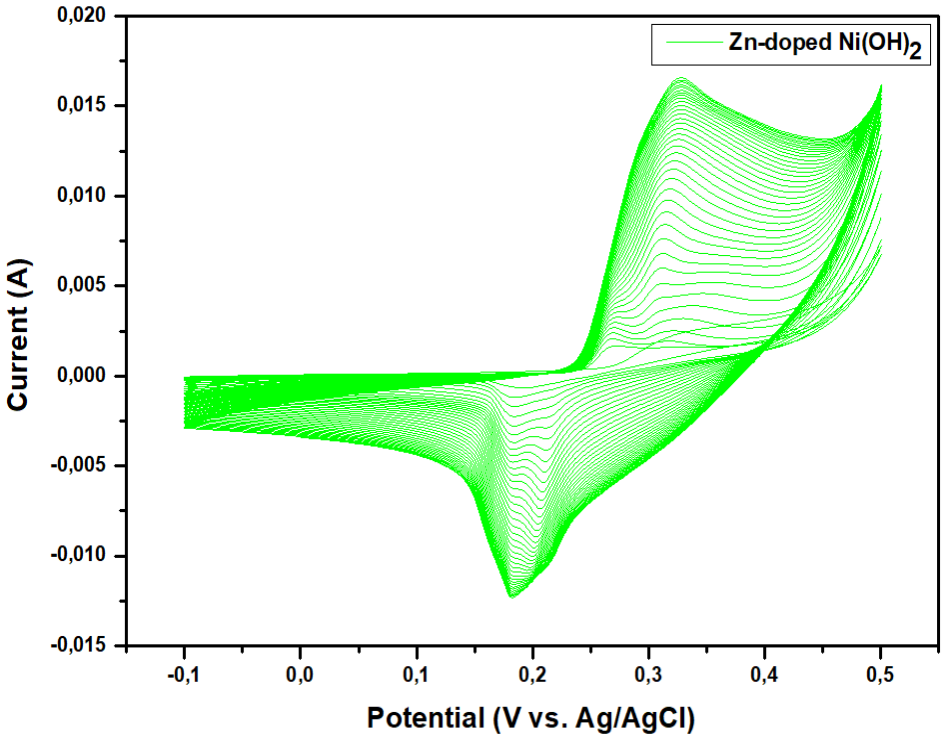

Figure 4.39. CV analysis of Zn-doped $Ni(OH)_2$.

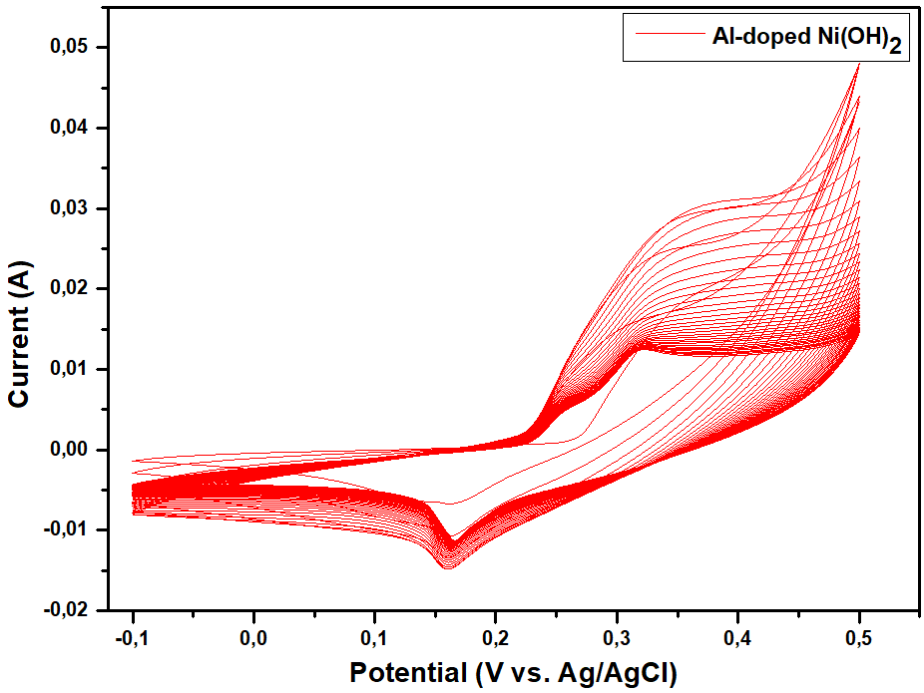

Figure 4.40. CV analysis of Al-doped $Ni(OH)_2$.

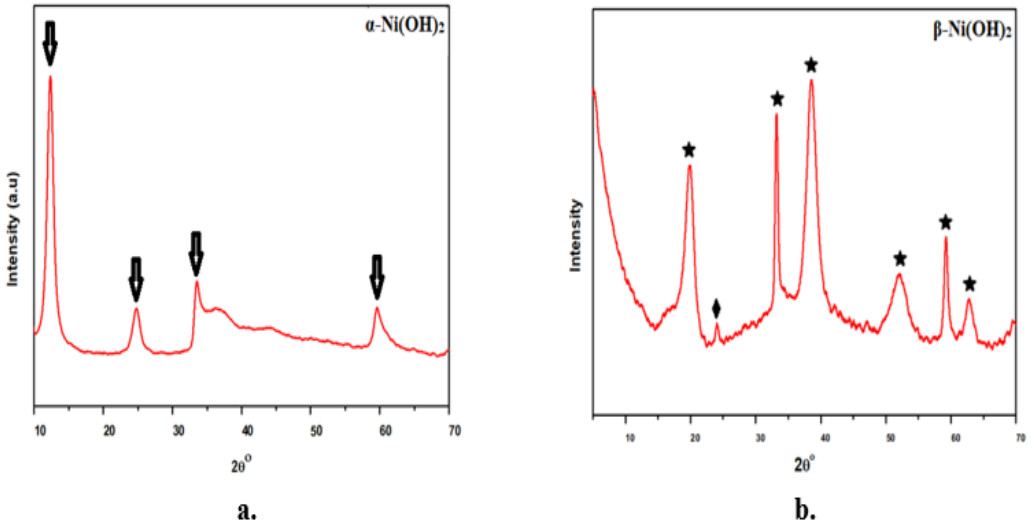

Figure 4.41. **a.** XRD patterns of α-$Ni(OH)_2$ crystal structure **b.** XRD patterns of β-$Ni(OH)_2$ (stars) crystal structure.

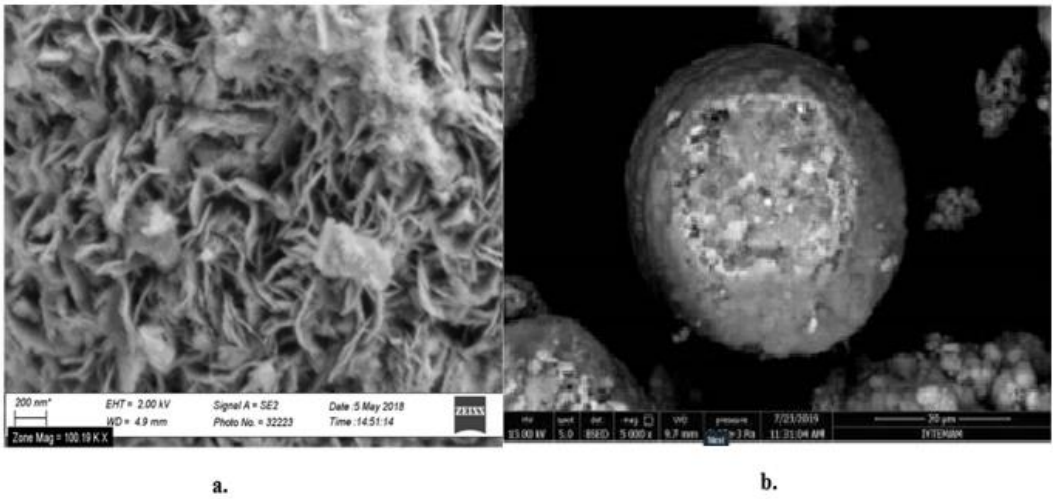

Figure 4.42. **a.** $Ni(OH)_2$ flowers-like structure form at 200 nm magnification **b.** Nikel hydroxide general form at 20 μm magnification.

Capacitance values of metal salts (Co, Cu,Zn, Al) doped-$Ni(OH)_2$ were calculated by using OriginPro-9 software. To this end, area between anodic and cathodic peaks was measured as absolute area via the software. Then, the capacitance values of the metal salts doped $Ni(OH)_2$ were calculated with the aid of the formula given below.

$$C_p = \frac{A}{2.m.k.(V_1 - V_2)} \quad (4.2)$$

Here, all the measurement of CV were executed at 10 mV/sec scan rate and between -0.1V and 0.5 V, 0.18 g of active materials were roughly loaded.

Where, so

m=0.18 g

V_1-V_2=0.6V

k= 10 mV/sec=0.01V/sec.

Table 4.8. Capacitance values of Co, Cu, Al, and Zn-doped $Ni(OH)_2$.

X-doped-$Ni(OH)_2$ X: Doped metal ions	**Co**	**Cu**	**Al**	**Zn**
Absolute area	0.99	0.51	0.31	0.17
Capacitance (Cp) (F/g)	463	231	135	79

The capacitance values of Co, Cu, Al, Zn-doped $Ni(OH)_2$ were found 463, 231, 135, and 79 F/g, respectivaly. It was determinated that electrochemical performance of cobalt doped $Ni(OH)_2$ is better tha the other doped materials such as Cu, Al, and Zn. Also, it is clear seen that current density of Co-doped $Ni(OH)_2$ show better performance in Figure 4.38. Moreover, it can be said that the Co-doped $Ni(OH)_2$ has a good capacity as cathode material for Ni-based battery.

The XRD results of alpha and beta nickel hydroxide forms are in compliance with the litarature of results. Synthesized β-$Ni(OH)_2$ peaks match better with the standard JCPDS FILE NO-14-0117 that indicates β-$Ni(OH)_2$ structure. The XRD peaks of β-$Ni(OH)_2$ are 20 (001), 32-33 (100), 39 (101), 52 (102), 59 (110), and 63 (111) 2θ degrees. in Figure 4.41.b. The α-$Ni(OH)_2$ crystal structure peaks are 10 (003), around 25 (006), 35 (101), and 60 (110) 2θ degrees in Figure 4.41a, and these peaks match the information in the literature. Broud peaks probably shows alpha-$Ni(OH)_2$ is in the amorphous structure. So, it can be said that both structure forms were well synthesized in the study.

SEM image of nickel hydroxide is indicated in Figure 4.42. In the SEM, nickel hydroxide particle size is around 20-25 μm in the Figure 4.42.b. The surface of the $Ni(OH)_2$ is flowers-like at 200 nm in the Figure 4.42.a. Also, the tap densities of all the doped-$Ni(OH)_2$ were found between 1.7-1.95 g/mL (Mark:Tap Dense-TD101).

Oxidation voltage values of Cu-doped-$Ni(OH)_2$, Co-doped-$Ni(OH)_2$, Zn-doped-$Ni(OH)_2$, Al-doped-$Ni(OH)_2$ are 0.43 V, 0.45 V, 0.32 V, and 0.36 V, respectively. Reduction voltage values of Cu-doped-$Ni(OH)_2$, Co-doped-$Ni(OH)_2$, Zn-doped-$Ni(OH)_2$, Al-doped-$Ni(OH)_2$ are around 0.15 V, 0.13 V, 0.175 V, 0.16 V, respectively (See Figure 4.37, Figure 4.38, Figure 4.39, and Figure 4.40). The reversibilities of M-(M:Cu, Co, Zn, Al)-doped-$Ni(OH)_2$ cathodes were calculated by using $\Delta E_p = Abs(E_{pa} - E_{pc})$ formula. Here, E_{pa} and E_{pc} represent anodic peak potential and cathodic peak potential, respectively. The different between the anodic peak and the cathodic peak inform about the reversibility of redox reactions. When this difference ($\Delta E_{p)}$ is minimal, the reversibility of the redox reaction reaches a bigger value. According to the difference ($\Delta E_{p)}$ values, the redox reactions can be irreversible or quasi-reversible. The ΔE_p values of Cu-doped-$Ni(OH)_2$, Co-doped-$Ni(OH)_2$, Zn-doped-$Ni(OH)_2$, Al-doped-$Ni(OH)_2$ were found 0.28 V, 0.32 V, 0.145 V, and 0.2 V, respectively. The reversibility of the cathodes is obtained as Zn>Al>Cu>Co. The anodic (positive current density, $Ni^{2+} \rightarrow Ni^{3+}$) and cathodic (negative current density, $Ni^{3+} \rightarrow Ni^{2+}$) peaks of Zn-doped $Ni(OH)_2$ are sharply seen. This probably shows that nickel is oxidized before oxygen arises from water in the medium, so the Zn-doped-$Ni(OH)_2$ cathode exhibits high reversibility, but low capacitance. Also, Wang et al showed the ΔE_p value of cobalt coated the surface of $Ni(OH)_2$ (0.27 V, lower overpotential) is smaller than the uncoated (only Co metal powder added for conductivity) $Ni(OH)_2$ (0.48 V), that is, more reversibility than that of the uncoated $Ni(OH)_2$. Here, the Co-doped $Ni(OH)_2$ is 0.32 V of the ΔE_p, it can said that cobalt affects reversibility of redox reactions of uncouted beta-$Ni(OH)_2$. (Wang et al., 1998). So, It can be suggested that when considering 0.48 V found by Wang et al., all the dopants (Cu, Co, Zn, Al) increase the reversibility of redox reactions. Surface modifications and dopants affect discharge capacity, reversibility, oxygen evolution overpotential, and electrochemical performance of a electrode (Wang et al. 1998). Both cobalt (for capacity and conductivity) and zinc (stabiliy and reversibility) probably significantly affect the capacity and stability of $Ni(OH)_2$ cathode (synergetic effect). Moreover, Liu and colleague showed that Al-stabilized α-$Ni(OH)_2$ and Co-encapsulated β-$Ni(OH)_2$ have lower ΔE_p values of 0.102 V and 0.28 V, respectively. Al dopant offer more reversibility than Co dopant (Liu et al., 1999). Studies of Liu and Wang have confirmed the study we did. In the thesis, while the Co dopant offers a high capacitance property (See Table 4.8), the Zn dopant contributes a high reversibility to the nickel hydroxide cathode.

4.5.5. Fabrication of Anode and Cathode, and Optimization Study for Measuring the Capacity of Cathode

The fabrication process of the cell starts by preparing Ni foam as a substrate. The substrates were cut in a suitable dimension (40 mm x 50 mm). All the Ni foam substrates were cleaned with nitrogen gase to remove dust particles, impurties, and humidity. For Cathode, 1 g active material (beta-Nickel hydroxide) was weighted. The active material, carbon black, and binder were mixed with 8.5:0.5:1 ratio. The mixture was stirred for 1-2 h until it was obtained a good slurry. The slurry was appiled on the clean nickel foam as current collector. CMC (%2 w/w CMC:water) were used as binder, as seen Figure 4.43.

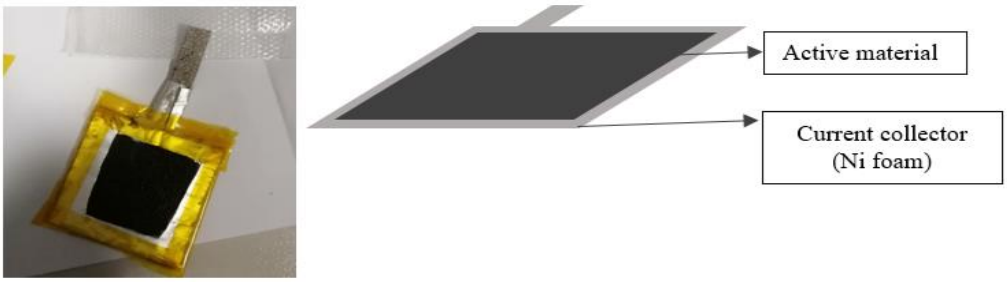

Figure 4.43. Preparation of cathode.

For anode, 4-5 g ZnO as anode material was weighted. The ZnO and binder were mixed with 9:1 ratio. The mixture was stirred for 2 h until it was obtained a good slurry. The slurry was appiled on nickel foam as current collector. CMC (%2 w/w CMC:water) were used as binder (see Figure 4.44).

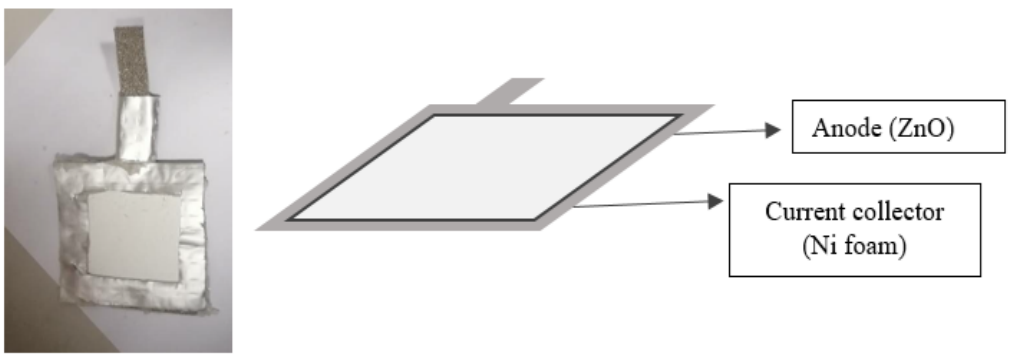

Figure 4.44. Preparation of anode.

Anode and cathode materials, by wetting with 6M KOH solution, were assembled by inserting a nafion-based membrane between them.

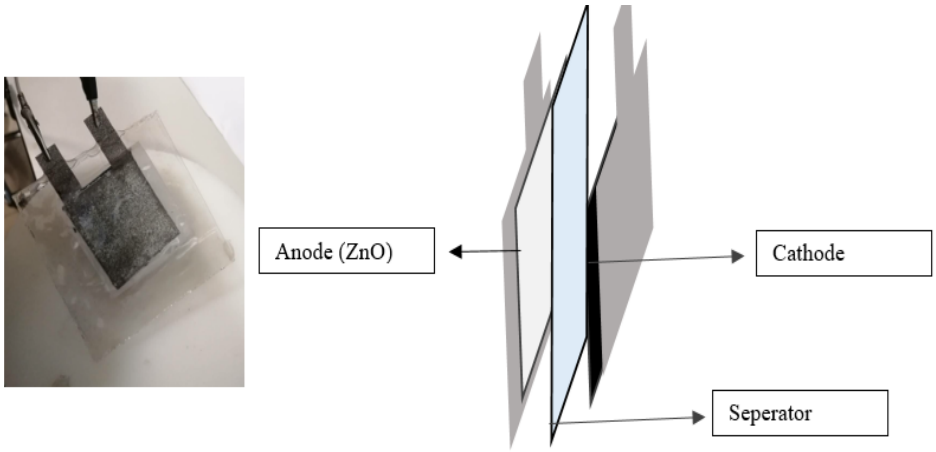

Figure 4.45. Assemble of anode and cathode.

For optimization of the cathode capacity, CC-Charging and CC-Discharging protocol was seleceted to determine the capacity of active material at 0.8-1.98 V. All the measurements was done by using Battery Tester Neware CT4000. Assemble of anode and cathode is shown in Figure 4.45.

Here, the experiments were executed according to the optimization studis as before-after. In the thesis, C rate, electrolyte effect, and binder effect were investigated and discussed to understand their effects on the capacity of the active material. The study of before optimization was done by using C1 cell (Figure 4.46) and C2 cell (Figure 4.47). However, the study of after optimization was done by using H-type cell to easly control electrolyte and binders because the H-type cell is a simple aparatus and easy control. During the process of charge-discharge, it is hard to control the C1 and the C2 cell types because they need a good design and a well-isolation anode-cathode to deal with short-circuit. Such type cells are also hard to open and close when the cell needs to be fed by the electrolyte.

4.5.6. Result and Discussion (Optimization Study)

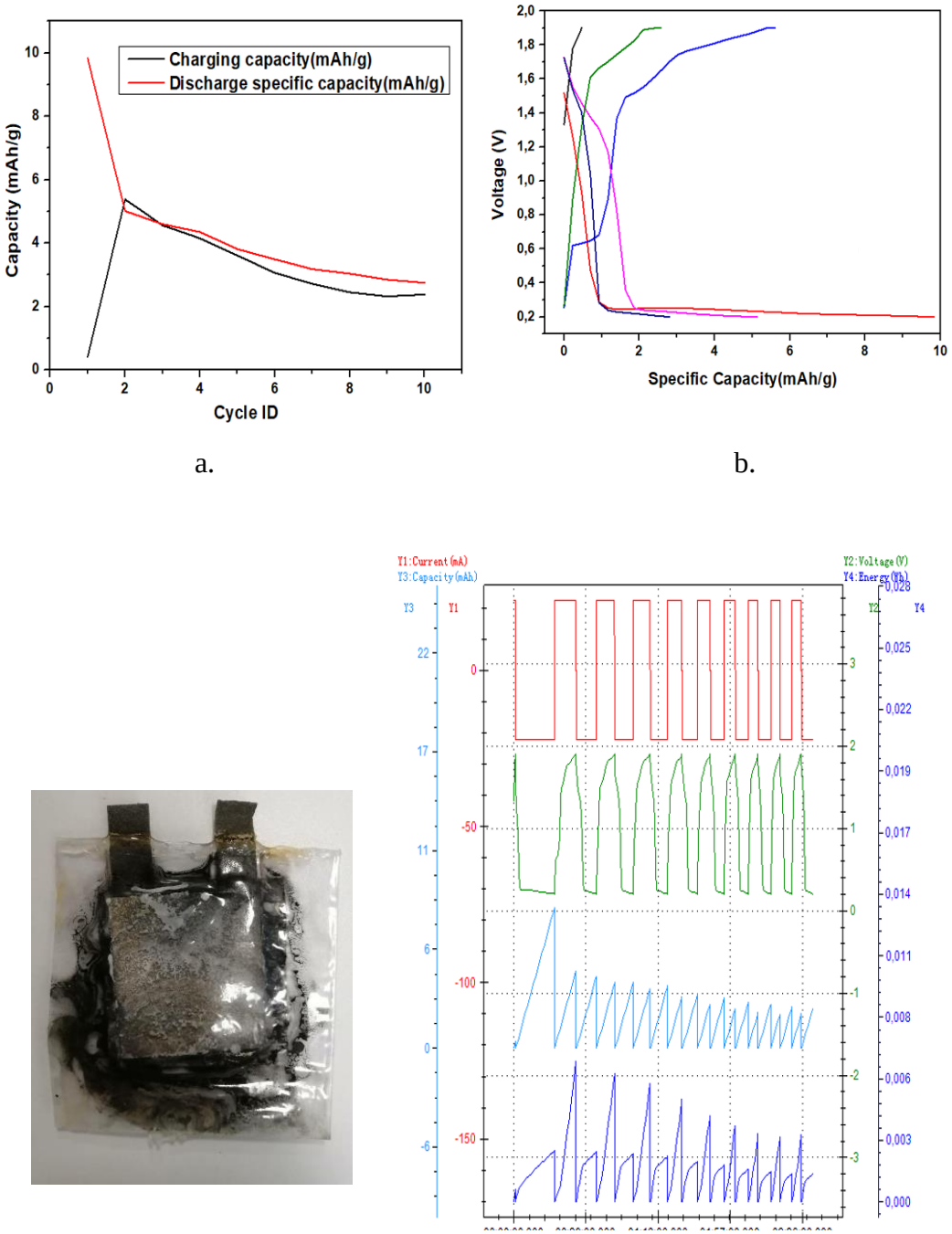

a. b.

c. d.

Figure 4.46. a. Capacity-Cycle number b.Voltage-Capacity c. Cell (**C1**), d. Current-Voltage-Energy patterns during charge and discharge.

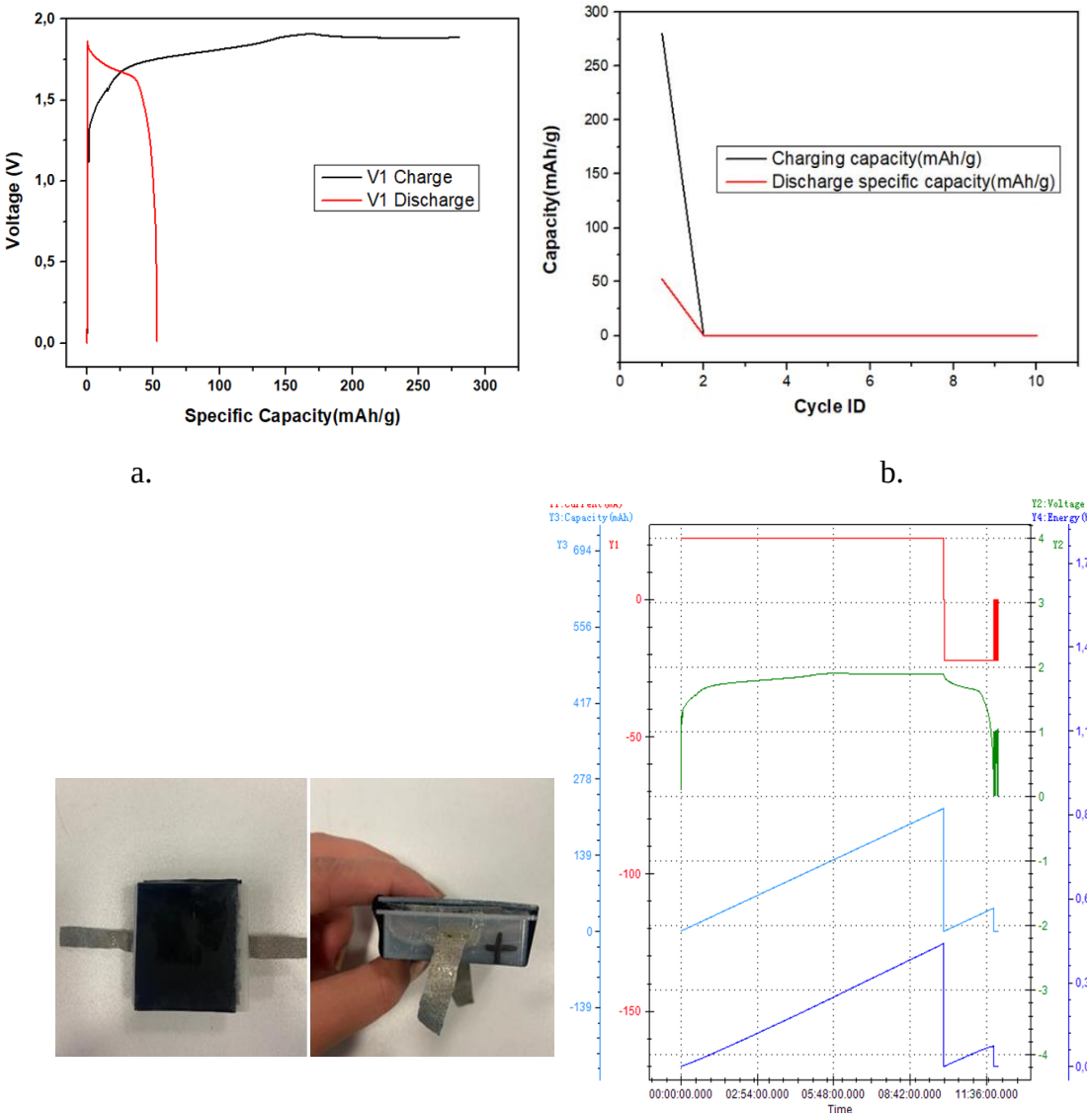

Figure 4.47. a. Capacity-Cycle number b.Voltage-Capacity c. Cell (**C2**), d. Current-Voltage-Energy patterns during charge and discharge.

C1 and C2 type cells were designed for optimization and capacity studies were carried out. Cell C1 seems to be quite low in capacity. In 10 cycles, both charging and discharging capacity showed a decreasing trend. Current and voltage patterns appear normal but they are irregular. Firstly, only three cycles were applied to the C1 cell to observe voltage-specific capacity patterns (Figure 4.46.b), but when the C1 cell passed from the charge phase to the discharge phase, over-discharge on the C1 occurred, causing hydrogen evolation reaction (HER). According to the Pourbaix diagram (see Figure 4.53), during discharge, straight lines, at around 0.2 V in Figure 4.46.b, show that hydrogen

evolution took place in the C1 cell. This phenomenon is not wanted in the cell because it causes the expansion volume of the cell, as it can be seen in Figure 4.46.c. Sometimes, this event can be also occured during over-charge, which triggers oxygen evolution in the cell, so the cell expands. Such expansions deteriorate cell and cell components, so the desired charge-discharge patterns are not observed. It is significant to control these effects for cell optimization and a good charge-discharge pattern. Here, The charge-discharge protocol was changed, and cut-off voltage value for the discharge was done more than 0.2 V to alleviate or remove HER. Also, the cut-off voltage for the charge was set at 1.98 V to deal with OER. Then the C1 cell again restarted for ten cycles to determine the capacity. However, the capacity value of the C1 cell was not satisfying and was very low. Possible factors that affects the capacity of the C1 cell, such as not enough well-seal, non-stable electrolyte, application method cathode-anode on the substrate, and lack of some additives materials to improve anode stability and electrolyte sability can be listed.

For the C2 cell, the charging voltage is stable and regular. The C2 cell showed, for the first cycle, good capacity, approximately 250-265 mAh/g. However, it can not say the same for the discharging capacity for the first cycle, approximately 50 mAh/g. It means that the C2 cell has very low efficiency. After first cycle, the C2 cell was short-circuited in Figure 4.47.d. Cell design and assembly are important factor that effect the capacity of active cathode. Also, the stability of electrolyte is a significant factor. For example, some additives must be added to electrolyte (KOH equeous) to get a stable electrolyte. A case for the C2 cell was designed for a good isolation. However, the C2 cell was able to resist only first cycles, especially the charge phase, after first cycles the C2 cell went to short-circuit (see Figure 4.47.d after 10 h, bold red and bold green vertical lines). The C2 cell is shown in Figure 4.47.c. Hydrogen evolution and oxygen evolution were not observev in the C2 cell. The C2 cell exhibited normal charge-discharge patterns for only first cycles, but this is not enough to determine real capacity of the cell during long cycles.

4.5.6.1. C rate Effect

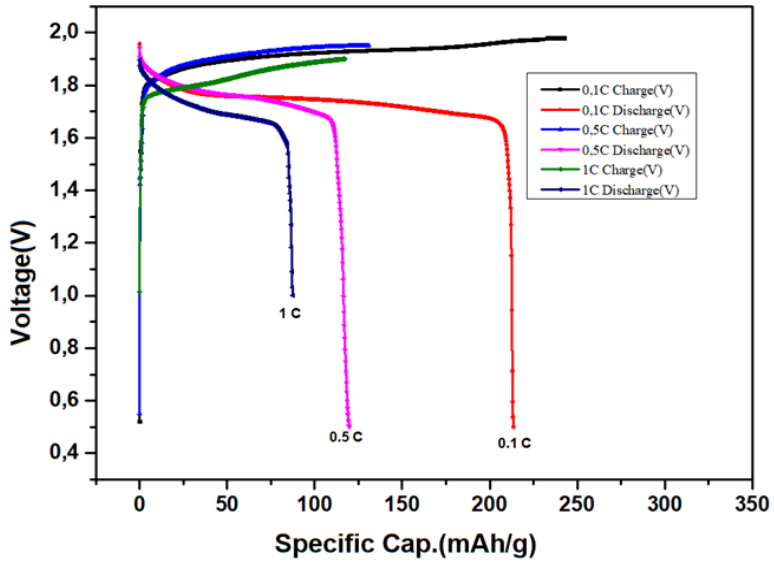

Figure 4.48. C rate effect on the capacity

It is clearly seen that the C rate affects the capacity of active material. The C rate test was executed for only the first cycle to determine C rate effect. In Figure 4.48, the highest capacity of the cathode was seen at the 0.1 C rate ratio, but the cell indicated the lowest capacity of the cathode at the 1 C rate. The cell delivered first discharge capacities of about 213 mAh/g , 122 mAh/g , and 90 mAh/g 0.1, 0.5, and 1.0 C-rates, respectively.

The cell or battery cycled at a higher c-rate have a bigger overpotential that brings about the cell to reach cut-off voltages more earlier in CC mode. Likewise, works studied on the $LiCoO_2$/Graphite cell at the C rates of 1C, and 0.5C and 0.1 C in CCCV protocol has indicated that max capacity fade or loss was at 1C rate. However, there are some studies indicated that the capacity loss can occur even at low c rate because of solid electrolyte interphase (SEI) event in lithium ion cell at 0.1 C (Snyder, 2016). Zinc dendride formation on the anode also affects the capacity of active material in the Ni-Zn cell. A high C rate has, maybe, quickly triggered zinc dendride formation on the anode and has caused capacity loss. The capacity loss of Ni-Zn cells accelerates with faster charge-discharge rates, this is supported by studies (Liu et al., 2022 and Ito et al., 2011). Some morphologies of Zn electrodeposits such as flat, mossy, and dendritic have been determined. The morphology has been significantly affected by high rates and

electrolytes. Zinc morphology (from micron to milimeter scale) may affect cell performance. Not only chemical mechanisms (the loss of lithium in the Li-ion battery, the loss of zincate ion in the Ni-Zn cell) but also mechanical mechanisms can affect cell performance at a high c rate. Mechanical phenomena play an important role at high c rates, for example, the degradation of active material particles accelerates at high c rates. This results in increasing battery resistance (Snyder, 2016).

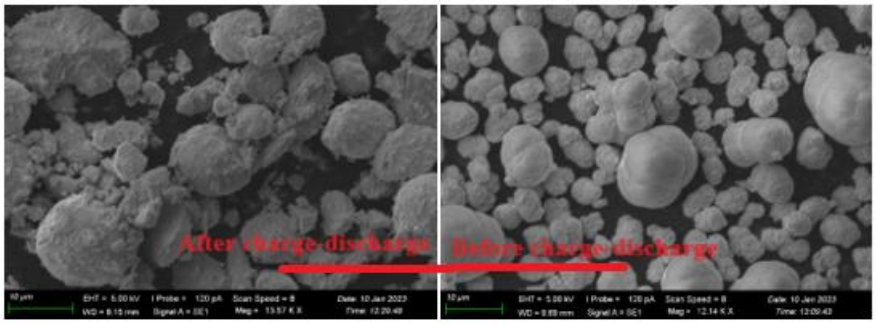

Figure 4.49. Degradation mechanism (after-before charge-discharge).

The mechanical mechanism is related to increase in resistance. The degradation of active material in the cell is depicted in Figure 4.49. This degradation causes capacity loss and increases cell resistance. A higher c rates accelerates the degradation and breakage in the active material particles. The charge-discharge of Zn anode in the electrolyte is directly associateed to the deposition-dissolution of Zn. During cell charge, Zincate ions ($Zn(OH)_4^{2-}$) is occured and then the Zincate ions gain two electron on the anode surface and is reduced to Zn. The zincate ions freely diffuse across the electrolyte and decompose into zinc oxide (ZnO). This is why the dendrites occur on the anode surface. These dendrites are unwanted on the anode surface due to affecting cell performance. Various additives materials, for example cetyltrimethylammoniumbromide (CTAB), polyethyleneglycol (PEG), and thiourea ($SC(NH_2)_2$, have been added to alleviate the dendrites (Liu et al., 2022).

4.5.6.2. Binder Effect

PVDF binder was prepared by mixing NMP as solvent and PVDF powder at % 5 ratio. PVP-PVA binder was prepared in 40 ml hot water at 17:3 w/w ratio, respectively. 100 ml hot water and 1-2 g CMC powder was mixed to prepara the CMC binder.

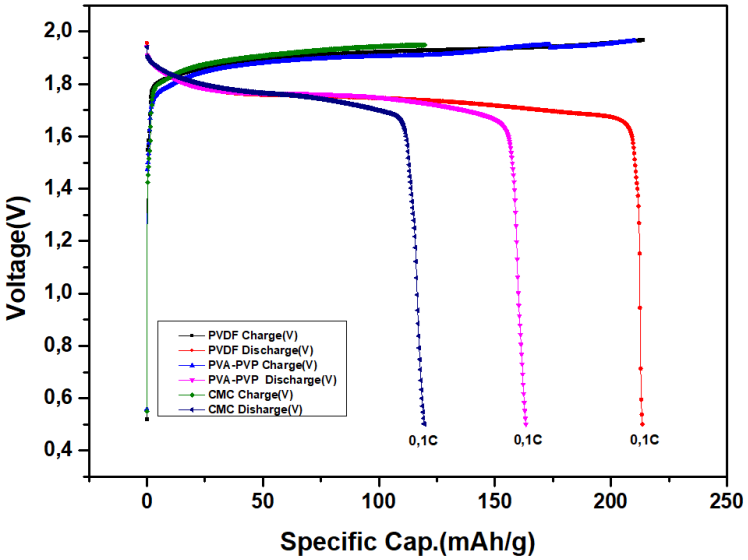

Figure 4.50. Binder effect on the capacity of the cathode.

The binder effect on the capacity is shown in Figure 4.50. All the tests were applied at the same C rate (0.1 C) to determine the binder effect and applied the same charge-discharge protocol. The PVDF binder indicated the highest capacity at 0.1 C rate among the binders. However, the CMC binder had the lowest capacity at 0.1 C rate. The PVP-PVA binder showed a moderate effect when it comperated to the other binders. Binders play a significant role of binding the cathode material and the conductive additives (carbon black). There are various binders, such as polyvinylidene fluoride (PVDF), poly-2-vinyl pyridine (P2VP), poly ethylene oxide (PEO), carboxymethly cellulose (CMC), polyvinyl alcohol (PVA), polyvinyl pyrrolidone (PVP). Some of them can be dissolved in the organic solvent that is N-methyl-2 pyrrolidone (NMP). The other polymers can also dissolvend in hot water. There is a ratio of carbon black to binder that affect mechanical integrity and cause increase or decrease conductive of cathode material. Therefore, the selection of binder is crucial to get more performace from battery or cell. Moreover, there is a balance between conductive additive materials and binder, which enhance conductivity and mechanic strength. For example, in the experiment, it was observed that the cathode material (beta-$Ni(OH)_2$) with CMC binder fell out or dispersed in electrolyte during charge and discharge. As mechanical, it can be said that the CMC is a weak binder, when it compared to the other binders types.

4.5.6.3. Electrolyte Effect

Table 4.9. Zn in the electrolyte amount for stabilization (EDX results).

Zn (in the electrolyte)/Time	3 hour	3 days	9 days
%	0.16	1.62	3.1

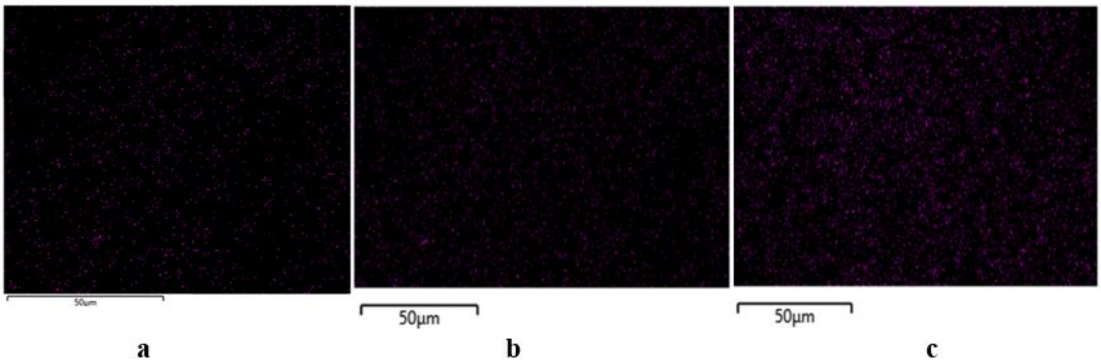

Figure 4.51. EDX mapping analyse Zn in the electrolyte **a.** 3h **b.** 3 days **c.** 9 days.

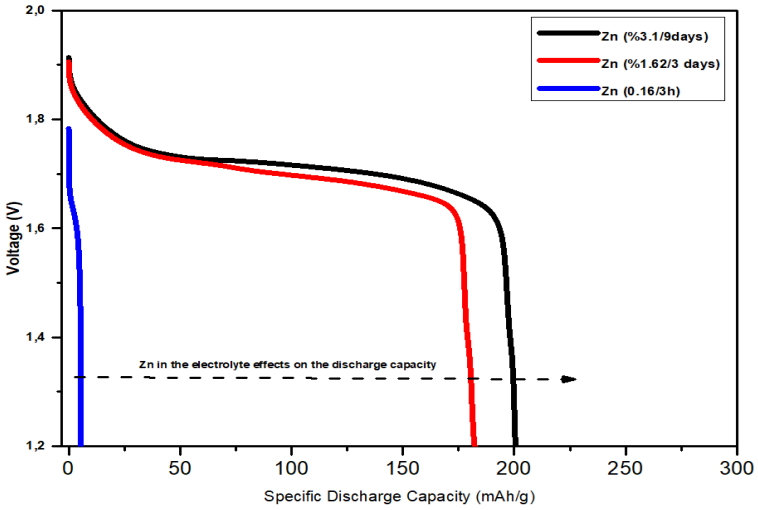

Figure 4.52. Zn in the electrolyte effect on the discharging capacity.

To observe the effect of electrolyte, Zn plate was immersed in the KOH electrolyte to saturate the electrolyte at different times. Zn plate staying times in the KOH solution at 3h, on 3 days, and 9 days, respectively, and percentage values in the KOH solution are shown in Table 4.9. The percentage values was determinated by utilizing EDX. Also EDX mapping analysis is depicted in Figure 4.51. EDX mapping analysis in Figure 4.51

indicates that the amount of zinc increased in the electrolyte over time. In Figure 4.52, it is clear that as the amount of zinc in the electrolyte increases, the capacity of the cell increases. For % 0.16 Zinc-3h (blue line) in Figure 4.52., the discharge capacity of the cell is about 10 mAh/g, while for the others, % 1.62 Zinc-3days (red line) and % 3.1 Zinc-9days (black line) are roughly 180 mAh/g and 200 mAh/g, respectively. When there are not enough zincate ions in the electrolyte, the discharge capacity decreases fastly. Also, there are various factors that affect the discharge capacity, such as dendrite formation, unstable zincate ions, and unbalanced zincate ion formation/deposition during charge-discharge. However, using the Zn plate directly as an anode in the cell is not suggested for more cycle numbers because the Zn plate can be corroded over time and form dendrite formation on the Zn plate surface, which affects the discharge capacity and efficiency.

Recent studies have prolonged the cycle span of the Ni-Zn cell by using a reduced concentration of potassium hydroxide to suppress zinc solubility in the electrolyte and by using additives materials (Linden, 2005) such as CTAB, PEG, and $SC(NH_2)_2$ (Liu et al., 2022). Moreover, Wen et al. demonstrated that lead ion and tetrabutlyammonium (TBAB) inhibited the growth of zinc dendrite due to synergistic effect of Pb-TBAB. Huang et al. indicated that the morphology of deposited zinc on the electrode changed at different current densities, and with high current density, discharge voltage decreased within a short time because of dendrite formation, which deteriorate the discharge capacity (Huang et al., 2023).

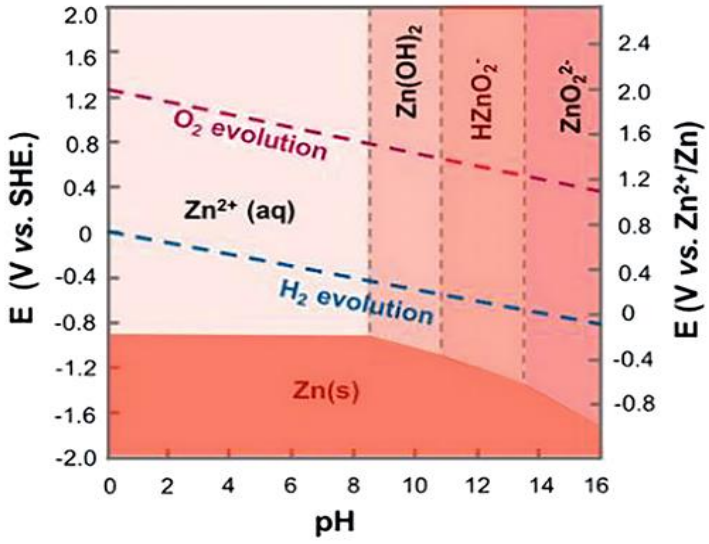

Figure 4.53. Pourbaix diagram (Liu et al. 2024).

Electrolyte affects the stability and the capacity of active material during charging and discharging. That is because some additives is added to electrolyte. Also, ZnO and Zn powder are added to electrolyte to producte zincate. The zincate/ZnO equilibrium in electrolyte depends on both the charge/discharge conditions (temperature, running time, KOH conc., additives, zinc feeding speed, etc) and the cell design. Electrolyte pH affects also OER and HER. Pourbaix diagram explains Zn/zincate formation (Zn and OH species) at different pH values, and HER and OER occurance voltages in Figure 4.53. Also, in a mild pH medium, zinc ion is easly surrounded by water molecules, formating the solvation shealth $(Zn(OH)_6)^{2+}$, which enhances energy barrier of the reduction and reduces the potential of Zn/Zn^{2+} reduction (Liu et al., 2024).

4.5.6.4. Process of the Optimization Preparation

Some optimization preparation studies were applied to improve the capacity of the cell. All the studies were did by using a reference product (commercial product, Beta-$Ni(OH)_2$). H-type cell (custom-made) was utilized during the optimization works (see Figure 4.54). Concentration of the electrolyte (KOH) was regulated as 6 M and was saturated with Zn to improve the stability of the electrolyte. Also, %5 PVDF was used as binder during this process. Finally, all the physical conditions were regulated. CC-Charge/CC-Discharge protocol was applied during the analysis.

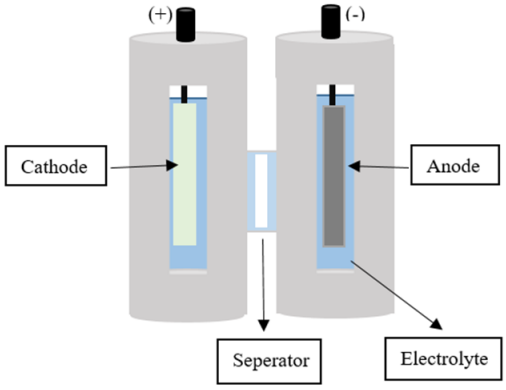

Figure 4.54. Custom-made H-type cell.

During the optimization works, the effects of c rate, binder, and electrolyte were investigated to optimize and to improve the cell's capacity. All these effects were

discussed in detail as well. After all the optimization process, the capacity of the synthesized Co-doped $Ni(OH)_2$ and the reference product were analyzed and dicussed in this thesis.

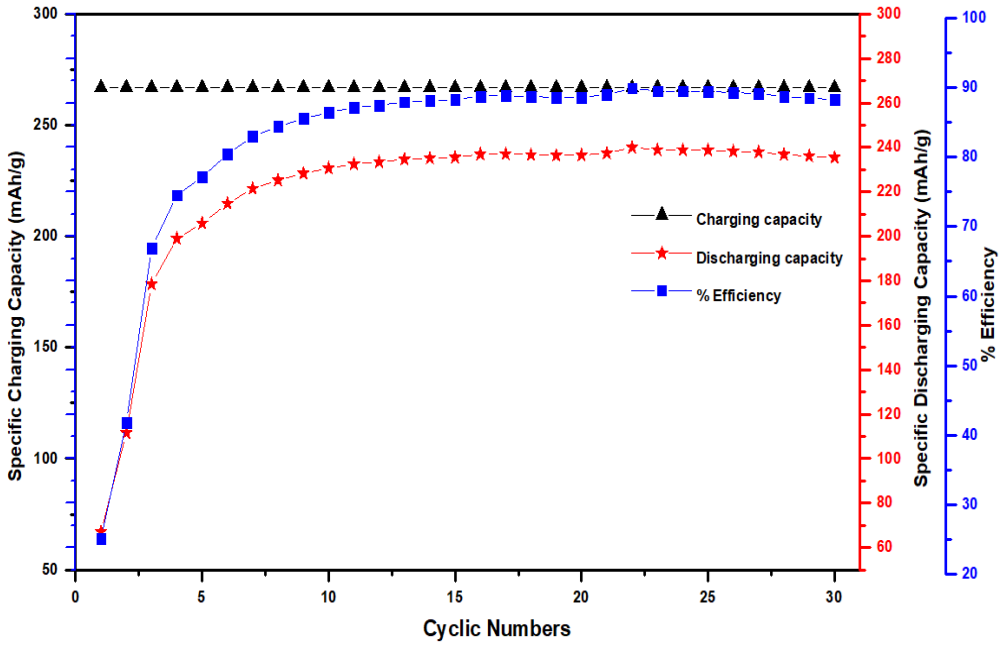

Figure 4.55. Reference product study.

In Figure 4.55, the CC-charge-CC-discharge protocol was applied to analyze the cell's capacity and efficiency. 30 cycles were applied to the cell to analyze its capacity. In Figure 4.55, a stable charge-discharge patterns exhibited during 30 cycles. The cell of efficiency was able to reach about % 90 value, as seen in Figure 4.55 (blue-square symbol-line). It can be said in this study that the optimization studies were successfully applied to improve the cell performance. Here, the protocol was applied by using custom-made H-type cell, % 5 PVDF binder, saturated-Zn electrolyte, and physical condition (room temperature and pressure, 1 atm). The cell's discharge capacity exhibited an incease between the first and tenth cycles, but after the 10th cycle, its discharge capacity showed a flat line, that is, reached a stable position. The discharge and the charge capacities are about 240 mA/g and about 265 mA/g, respectively. However, more further cycles are needed to get a general charge-discharge pattern. In this study, only 30 cycles were applied to the cell to check the optimization study. In literature, the nominal capacity of beta-nickel hydroxide is 289 mA/g. Considering this value, it can be said that the

reference product exhibited a good performance for thirty cycles, especially in the aspect of the charge capacity, which shows that the optimization studies have worked.

On the other hand, in the thesis, the capacity of the synthesized Co-doped-$Ni(OH)_2$ was analyzed. All the same procedures and optimization works were also applied to the Co-doped $Ni(OH)_2$ product.

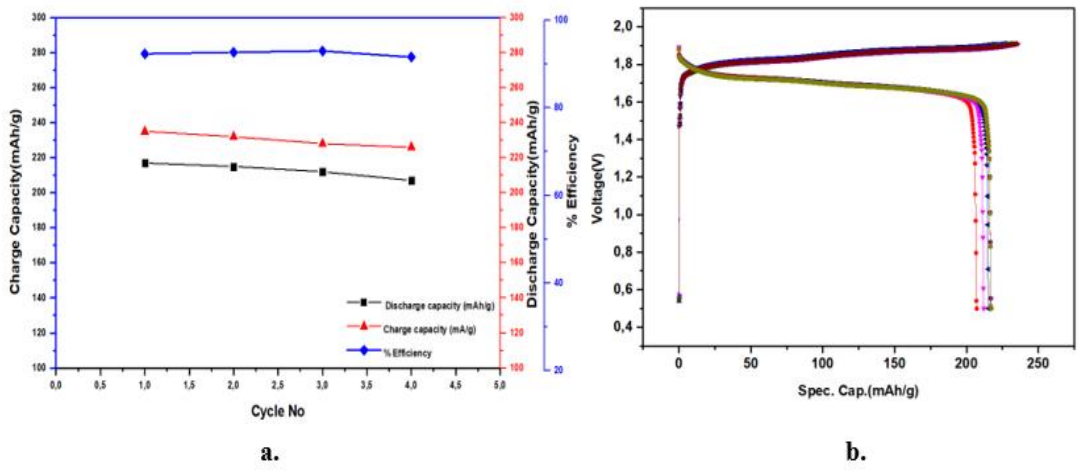

Figure 4.56. Co-doped-$Ni(OH)_2$ product **a.** cycle-capacity, **b.** voltage-specific capacity.

In the study, only four cycles were applied to the cell to examine the optimization process. The CC-charge and CC-discharge protocol was used. The cut-off voltages were set at 1.98 V for charging and at 0.6 V for discharging. Voltage-specific capacity pattern was indicated in Figure 4.56.b. The charge and discharge specific capacities were found about 240 mA/g and around 210 mA/g, respectively. The efficiency of the cathode is more than % 90 (see Figure 4.56.a, blue-line). It is clearly seen that the discharge voltage was sharply dropped at around 1.5 V in Figure 4.56.b. This shows that the cell can discharge up to around 1.5 V, which means a majority discharge capacity of the cathode has lost around 1.5 V.

It can be said here that the optimization study for the Co-doped-$Ni(OH)_2$ product has worked. However, it is not enough for only four cycles to determine the capacity of the cathode, because the cathode can maybe lose its capacity after long long cycles. So, a different voltage-capacity pattern and a cycle-capacity pattern can occur after long cycles. This is because the cathode material can be mechanically and chemically deformed during long cycles. In the thesis, the study was done at a few cycles as much as possible to accelerate the optimization study. Here, the related between the capacity and the

optimization studies is illustrated in Figure 4.57. It is seen that the more optimization studies are done and the conditions are controlled, the more capacity increases.

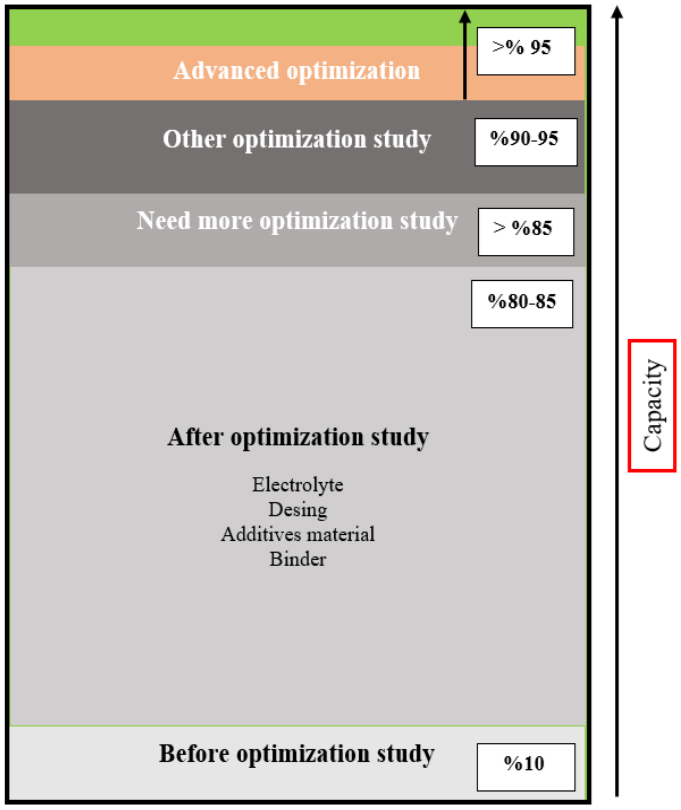

Figure 4.57. Optimization-capacity relationship.

In the thesis, it can be said that the improvement of the capacity is %80-85 after electrolyte, desing, additives material, and binder are stabilized and developed. For further impovement of the capacity, advanced optimization studies are required to reach >% 95 as seen in Figure 4.57. All the physical (temperature,pressure,design, anode-cathode assemble etc) and chemical (additive materials, cathode and anode composition, electrolyte etc) condition must be controlled to reach the full capacity of the cathode material.

4.5.8. Conclusion and Future Perspective

Nickel hydroxide as cathode material for Ni-based battery was fabricated by using the urea decomposition method (hydrothermal methode). Both alpha-$Ni(OH)_2$ and beta-$Ni(OH)_2$ forms were synthesized and characterized by XRD, SEM, and CV (but CV analysis of the alpha-nickel hydroxide was not done). Cu, Al, Co, and Zn doped beta $Ni(OH)_2$ were measured for their electrochemical properties, then were compared electrochemical performances in terms of current density. The capacitance ($F.g^{-1}$) values of the Cu, Al, Co, and Zn-doped β-$Ni(OH)_2$ were found 231, 135, 463, and 79, respectively. The study indicated that the ranking current densities of Cu, Al, Co, and Zn-doped β-$Ni(OH)_2$ are Zn<Al<Cu<Co. XRD peaks depicted that alpha form $Ni(OH)_2$ was amorphous structure. Also, the capacity of the Co-doped beta $Ni(OH)_2$ cathode was analyzed by using Battery Tester machine. The capacity of the cathode was measured at different C rate. Moreover, different battery cells have been fabricated to optimize its capacity and to get maximum performance. C rate effect, binder effect, and electrolyt effect were widely discussed in the thesis. The optimization works were done to obtain the maximum capacity from the active cathode material we synthesized. We showed that the discharge specific capacity of the Co-doped β-$Ni(OH)_2$ is around 210 mA/g after the optimization studies (during all the optimization studies were used commercial product as reference)

More optimization studies and different dopant chemicals can be carried out to get maximum stability and capacity from nickel hydroxide. The sensor, catalyst (OER, ORR from water spliting or the other organic compounds), and supercapacitor properties of nickel hydroxide can be investigated. Various addivite materials (Bizmuth oxide, calcium hydroxide or oxide, lead (II) oxide, and some organic chemicals) will be investigated and discussed to improve the capacity of the β-$Ni(OH)_2$. In this part of the thesis, unfortunately we studied the capacity of the beta-nickel hydroxide for only a few cycle numbers, this may not be enough because we need long and long cycle numbers to determine actual capacity of the synthesized β-$Ni(OH)_2$.

4.6. Aim and Motivation

Recently, researchers have intensively studied lithium-ion cells due to the decrease in fossil fuels (oil, natural gas, coal) and the development of electric vehicle (EVs). The supply of a good active cathode for Li-ion batteries is a significant issue to meet the needs in the technological developments and in the battery sectors. NMC and NMC-derivatives are some of the most important cathode active materials that are utilized in most Li-ion batteries and next-generation batteries. NMC material has a high theoretical capacity, low toxicity, and good thermal resistance. Also it posseses high energy density. The NMC cathodes have about 234 mAh per gram of specific capacity. NMC622 is one of the most promosing cathode for Li-ion cells because of its high capacity and high energy. There are numerous studies in the literature about NMC and NMC derivatives, such as NMC111, NMC811, NMC622, and NMC532 etc.

In the thesis, we have firstly synthesized $Ni(OH)_2$, $Mn(OH)_2$, and $Co(OH)_2$, separately. Then, we fabricated NMC622 cathode material using ball-milling mathode (solid state methode). The NMC622 active cathode was characterized by utilizing XRD, ICP-OES, and SEM. For capacity study, the NMC622 slurry was prepared and applied on Al substrate. CR2032 coin cell was assembled to determine the capacity of the NMC622 by using battery tester.

Li-ion battery starts to become important because of developments in the EVs. the Transition-metal mixed oxide (NMC and its derivatives) has attracted significant attention as a potential substitute. In the literature, Single crystal NMC can be promising cathode material for lithium ion batteries because of its high stability. Such developments motivate us to synthesize and improve NMC cathode.

In this part of the thesis, now we will discussed below headlines;

- Synthesis of NMC622 cathode for Li-ion battery
- Assemble anode and cathode for capacity study
- Result and discussion

4.6.1. Synthesis of NMC Cathode Material for Li-ion Battery

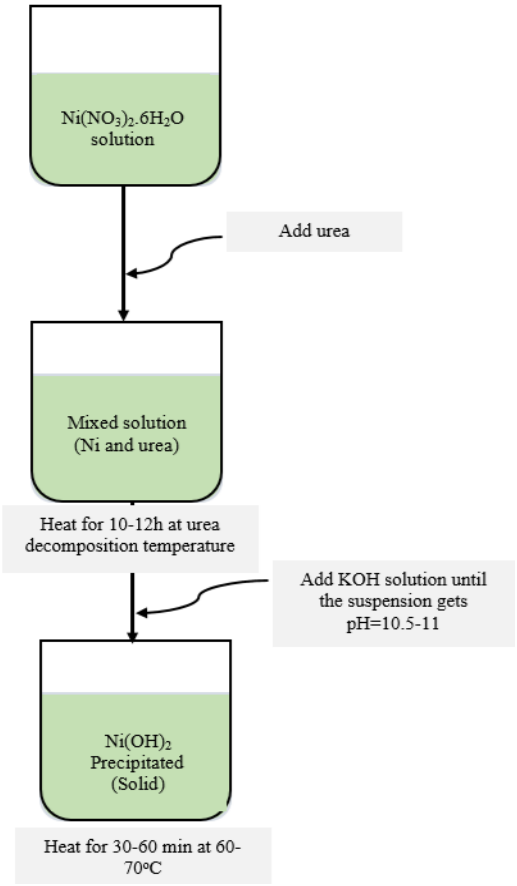

a. **b.**

Figure 4.58. b. scheme of the NMC synthesis a. $Co(OH)_2$, $Ni(OH)_2$, $Mn(OH)_2$.

Mol ratio:6:2:2 (Ni, Mn, Co, hydroxide forms, respectively) was weighted and put in the plastic bottle with ethanol. (ethanol vol : the bottle vol 7:10) 1:10 (w/w, total Metal-hydroxide: ZrO_2 ball numbers) was applied and stirred for 24h. The sythesized procursor NMC-hydroxide form was mixed with Li_2CO_3 as % 3-5 and calcinated at 900ºC. Here, the same methode, as seen Figure 4.58.b, was followed to synthesize $Mn(OH)_2$ and $Co(OH)_2$. In Figure 4.48.a, left beaker (purple-blue), middle beaker (green), right beaker (brown-mud) represent $Co(OH)_2$, $Ni(OH)_2$, and $Mn(OH)_2$, respectively.

4.6.2. Assemble Anode-Cathode for Capacity Study

Li chips metal (disc form) as anode was purchased from Xiamen Aot Electronics Technology Co. LTD, China. The positive electrode was prepared by mixing the 90% NMC cathode powder, 5% carbon black, and %5 PVDF binder. The slurry was stirred for 1 h to get the desired viscosity. The slurry was applied uniformly to an aluminum foil as current collector. The Al foil with the NMC cathode was dried at 70^{o}C for 24 h and was cut in disc form by using cutting apparatus (disc cutter), as seen Figure 4.59a. The loading amount of the NMC cathode on the Al substrate was weighted as 10 mg. Polypropylene (PP) was used as the membrane and 1.0M $LiPF_6$ (EC/DMC:50v/50v) solvent was utilized as the electrolyte. PVDF powder and NMP organic solvent were mixed to prepare % 5 PVDF binder. The coin cell pieces are depicted in Figure 4.59b.

a. **b.**

Figure 4.59. a. The applied and cut NMC cathode b. Coincell pieces.

CR2032 coin cell was bought from Xiamen Aot Electronics Co. LTD, China. The coin cell was used to test the capacity of the NMC cathode. The coin cell components is shown in Figure 4.60. The CR2032 coin cell was assembled in a glovebox.

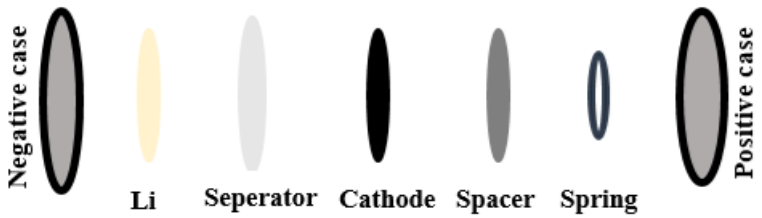

Figure 4.60. CR2032 coincel components.

4.6.3. Results and Discussion

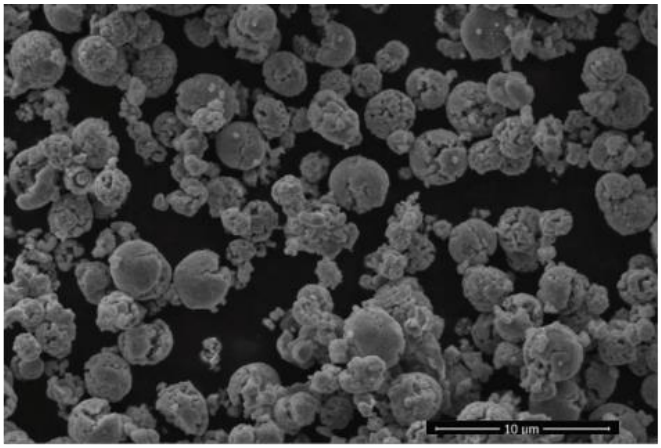

Figure 4.61. SEM image NMC622.

Figure 4.61. indicates scanning electron microscopy (SEM) image of a maltiparticle overview of the NMC622 cathode. General particle distribution is around 5 micron. There are particles, as seen in Figure 4.61, that are smaller than 5 μm and are larger than 5 μm. It can be clearly seen that some particles are split and cracked. Some of them are also deformed and have irregular shapes. These results indicate that zirconia balls used during the synthesis probably break down some particles and deteriorate their shapes. However, a spherical shape is more dominant after calcinating. Various factors that affect morphology of the particle NMC cathode, such as temperature, annealing temperature, calcination temperature, selected methode, pH, selected chelating chemicals (this especially in the coprecipitation methode), and rpm have profoundly discussed by Malik and his colleagues (Malik et al.,2022). Moreover, Ihalainen and his colleagues studied how calcination temperature affects the morphology of the NMC particles and they widely discussed these factors. For example, in their study, the particles of NMC cathode have spherical geometry and regular morphology between 600 and 700^{o}C, while these particles start to deform and to be cubic-like structures between 850 and 900^{o}C (Ihalainen et al., 2023).

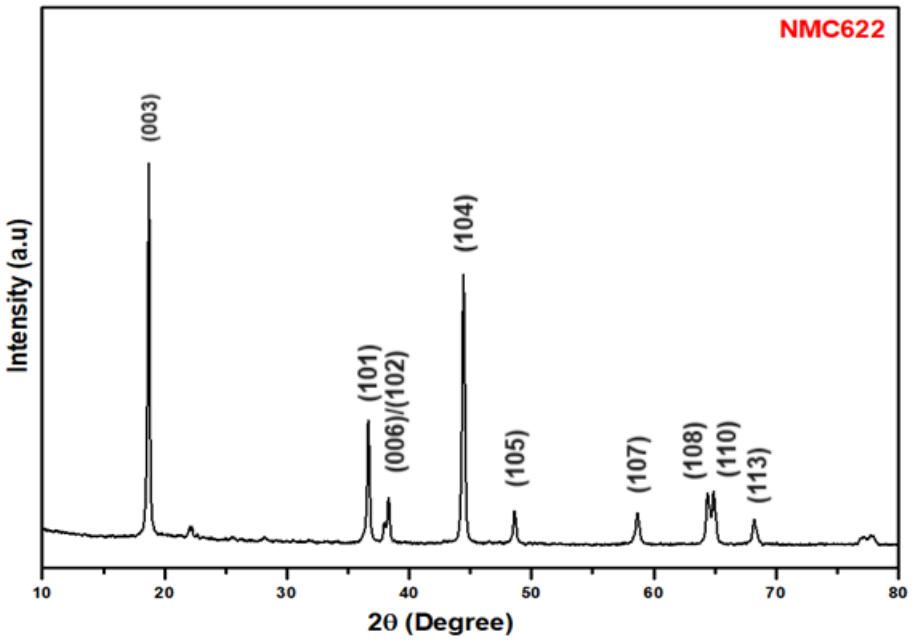

Figure 4.62. XRD pattern NMC.

Figure 4.62. shows XRD patterns of the NMC cathode powder in the 10-80º2θ. All the diffraction peaks are sharp and clear. This indicates a well- crystallized structure and the enumerated signals correspond to characteristic the NMC cathode. The XRD patterns of the NMC powder macths with alpha-$NaFeO_2$ hexagonal structure with space group R3m (Zybert et al., 2023), also all the peaks that belongs the NMC cathode comply with the literature. A few additional peaks are observed in the 20-25 º2θ and 75-80 º2θ. These foreign peaks may be refered to small impurities in the structure (Zybert et al., 2023), but some studies have shown that the small signals in the 20-25 º2θ regard to superlattice phenomenon resulting from between NMC111 and Li_2MnO_3. Moreover, peak splitting are observed around 37º and around 64º (Ihalainen et al., 2023), these peaks result from the existence of a $Li(Ni,Mn)_2O_4$ spinal-phase (Bak et al., 2014). The characteristic (006)/(102) and (108)/(110) peaks point out a high degree of hexagonal ordering of the layered structure (Ren et al., 2017). Furtermore, low value ($I_{006}+I_{102}/I_{101}$) ratio shows a high hexagonal ordering of the structure. I_{003}/I_{104} parameter is the most important factor that is related to the phenomenon of lithiım ion and nickel ion mixing (Zybert et al., 2023). The minor signals between 75 and 80º2θ could have come from phases such as $Ni(OH)_2$, $Mn(OH)_2$, and $Co(OH)_2$ which are unreacted as impurities

(Malik et al.,2022). The NMC622 lattice parameters are *a* (2.8741), *c* (14.2346), *V* (101.831), and *c/a* (4.9527) (Zybert et al., 2023).

Table 4.10. ICP-OES analysis results for the NMC.

Elements (ICP-OES)	%
Li	8
Ni	32
Co	11.7
Mn	11.1

The NMC cathode was dissolved in an acid medium via microwave digestion for analysis. ICP-OES instrument was used to determine the chemical composition of the NMC cathode material, and the results have shown good agreement with the 6:2:2 ratio of the NMC as seen in Table 4.10. In the literature, the elemental composition of NMC622 was determined by using ICP-OES, and the elemental mole ratios of Li, Ni, Mn, and Co were found to be 0.927, 0.610, 0.19, and 0.20, respectively (Ihalainen et al., 2023). Both these results match with each other.

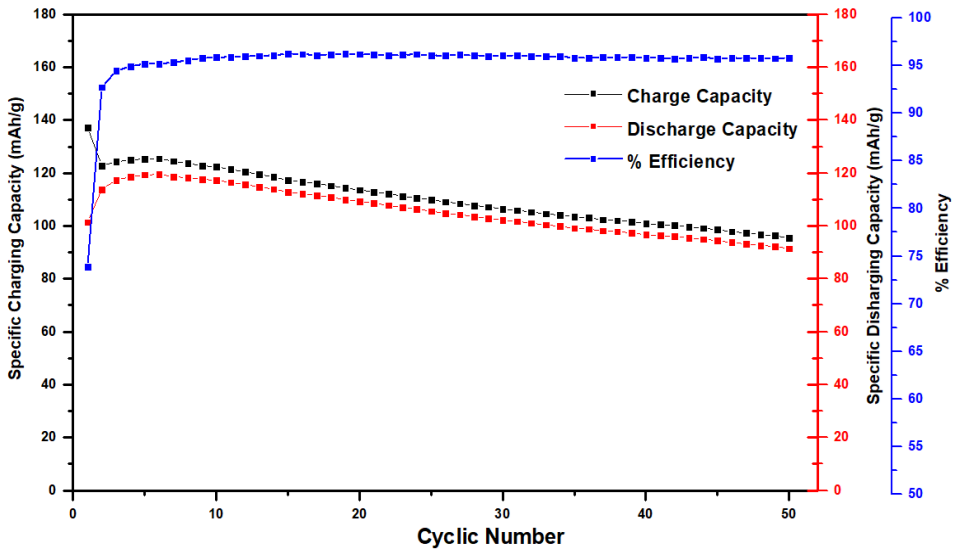

Figure 4.63. Capacity of the NMC active cathode.

In Figure 4.63., work of capacity was done by using the coin cell. CC-charge/CC-discharge protocol was executed in the voltage range of 2.6-4.3 V during 50 cycles with

a 0.1 C rate. Figure 4.63 presents electrochemical properties of the synthesized NMC622 active material. The value Coulombic efficiency is slightly over 95%. The capacity of the charge and the discharge exhibited a slight decrease during first 50 cycles and showed similiar patterns as seen in Figure 4.63. Specific charge and discharge capacity of the NMC cathode material is around 125 mAh/g for first 10 cycles. In the literature, the theoritical capacity and actual capacity of NMC622 pristine active cathode material are 277 mAh/g and 175 mAh/g, respectively (Chang et al., 2023). The synthesized NMC622 active material has exhibited a low specific capacity when considering actual and theoritical value of NMC622 active material. These can be related to oxygen and humidity in the glovebox, the morphology of the NMC622 (particle distribution and size), applying the active material on the Al substrate (thickness, smoothness), and inorganic/organic impurities during assembly. Such factors play a significant role in the capacity and efficiency of an active cathode material.

4.6.4. Conclution and Future Perspective

NMC622 was successfully synthesized and characterized. The result of the ICP-OES showed that NMC cathode material has 6:2:2 ratio, Ni, Mn, Co, respectively. The XRD indicated all the peaks related to NMC cathode and matched well with the literature (standard signals) peaks. The spherical particles of the NMC622 are around 5 micrometer according to the SEM image. It was found that specific charge and discharge capacity of the NMC622 are around 125 mAh/g for first 10 cycles, respectively. However, these capacities significantly decreased around 50 cycles. The NMC622 exhibited the Coulombic efficiency of over %95. Generally, it can be said that the synthesized NMC622 active material has exhibited a low specific capacity when considering actual and theoritical value of NMC622 active material. There are various factors that affects the capacity of the active cathode, for example oxygen and moisture in the cathode and in the glovebox, the cathode of thickness on the substrate, roughness etc. Next, we will profoundly control these factors effecting on the capacity of NMC cathode and we will investigate different synthesis methode to improve capacity and Coulombic efficiency. More cyclic numbers and the capacity of the NMC cathode will be studied at high voltage. The penetration of lithium ions into NMC structure will be investigated to understand the mechanism of charge-discharge and effect of Li ion on the structure.

4.7. Aim and Motivation

Halide perovskite materials offer high performance properties in solar cell applications. Also, due to their flexibility, these materials offer a significant opportunity to improve material science. Perovskites can be classified as metals, insulators, and semiconductors. Composite oxides (perovskite, perovskite-like oxides) are understood to have an activity for the oxidation of hydrocarbon (HC) and carbon monoxide (CO). These catalysts have a high oxygen vacancy density and a powerful redox ability, which plays a significant role in catalyzing oxidation reactions. Dai and colleagues in 2000 and 2001 studied various halo-oxide (halide element + oxygen) perovskites such as $ACuO_{2-\delta}X_{\sigma}$ (A = $Sr_{0.63}Ca_{0.27}$, X= F, Cl) (Dai et al., 2001), $AMn_{1-x}Cu_xO_{3-\delta}$ (A = $La_{0.8}Ba_{0.2}$) (Dai et al., 2001) $La_{1-x}Sr_xFeO_{3-\delta}X_{\sigma}$ (X=F, CI) (Dai et al., 2000) and $YBa_2Cu_3O_{7-\delta}X_{\sigma}$ (X = F, Cl). (Dai et al., 2001). Also, they investigated the catalytic performance and characterization of these halo-oxide perovskites for the oxidative dehydrogenation of ethane (ODE) to ethene.

In this part of the thesis, we synthesized $PbVO_3CI$ by using hydrothermal methode. By using DFT approximation methodes (HSE06, GGA, and LDA), the band gap energy of the $PbVO_3CI$ powder was calculated. We showed that the $PbVO_3CI$ is as semiconductor. We tried to answer the question “is the $PbVO_3CI$ structure perovskite?” in the light of the literature. Probably, this structure can be a new halo-oxide perovskite when considering Dai’s studies related to halo-oxide perovskites. We discussed the Born and Phono criteria of the $PbVO_3CI$ structure as well.

The $PbVO_3CI$ can be promising a new halo-oxide perovskite for fuel cell studies and solid membrane for SOFC, or catalyst, and so on. The catalytic activity, photocathode, photoanode, membrane property for SOFCs, and electronic structure of the $PbVO_3CI$ are required to investigate. So, this structure can be intensively studied for next academic research.

Now, here, we will discussed below headlines;

- Synthesis and Characterization of $PbVO_3Cl$
- Result and Discussion
- Born and Phonon criteria for the $PbVO_3CI$
- Is the $PbVO_3CI$ a perovskite?

4.7.1.Synthesis and Characterization of $PbVO_3Cl$

$PbVO_3Cl$ sample was first synthesized, and its crystal structure was determined by Şahin and Eanes M. For synthesis, in the presence of 1.66 M boric acid, $NaVO_3$ and $PbCl_2$ as reagents were used in the ratio 0.5:1 (w/w), respectively. The mixture was placed at 170°C in the oven. Yellow color crystals were obtained. $PbVO_3Cl$ product was yielded by approximately 55-60 %.

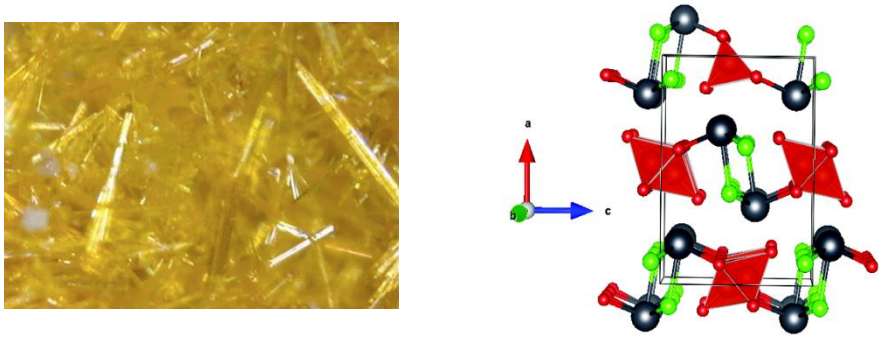

a. **b.**

Figure 4.64. **a.** Photo of the $PbVO_3CI$ product (Şahin, 2004). **b.** Crystal Structure of $PbVO_3Cl$; (Gray: Pb, Blue: V, Red: O, Green: Cl (Theoretical Construction of Crystalline Structureof $PbVO_3Cl$ was drawn with Vesta software, a = 10.022(2) Å, b = 5.288(1) Å, c = 7.171(1) Å 1).

Figure 4.64 represents (a) photo of the $PbVO_3CI$ and (b) crystal structure of the $PbVO_3CI$. The $PbVO_3CI$ product is yellow color and needle-like shape.

4.7.2. Result and Discussion

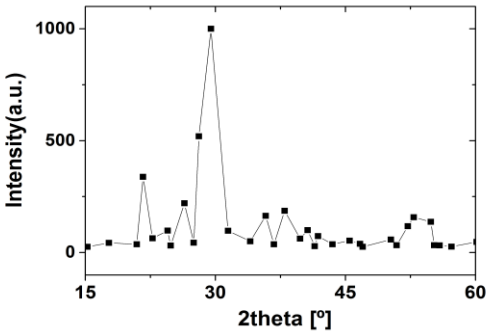

Figure 4.65. XRD of the $PbVO_3CI$.

The characteristic XRD peaks of the $PbVO_3CI$ are indicated in Figure 4.65. The $PbVO_3CI$ was determined and graphed by using High Score Software program. Between 5^o -70^o 2θ was scanned to determine XRD of the $PbVO_3CI$. Emirdağ-Eanes and Sahin indicated, in 2007, that the $PbVO_3CI$ is orthorhombic structure and is in the *Pnma* space group. Also they determined all the lattice parameters of this structure and bond lengthes of Pb-O, Pb-CI, and V-O. Moreover, the TGA analysis showed that the decompose temperature of the $PbVO_3CI$ is around 480^oC. It was indicated major weight loss, 368-510^oC, comes from chloride element (Sahin and Eanes, 2007).

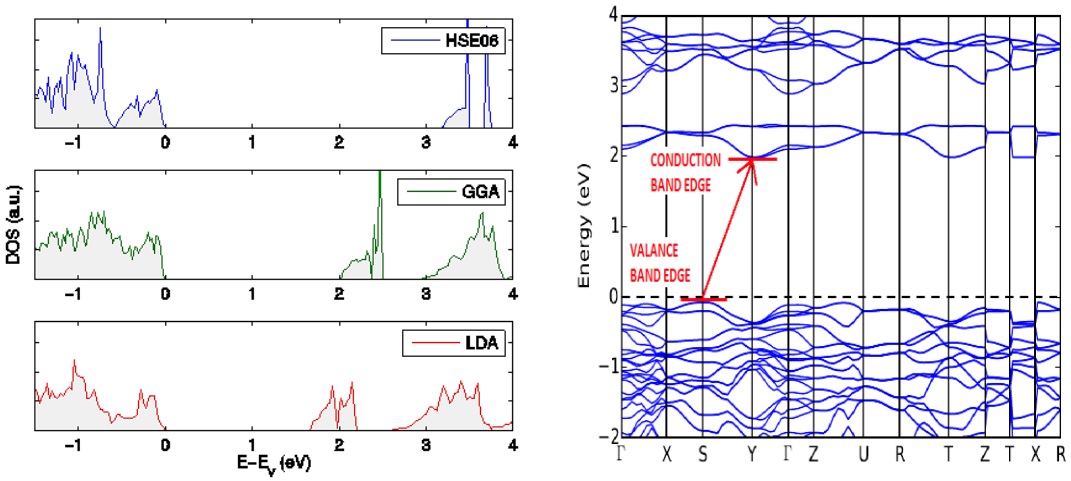

a. **b.**

Figure 4.66. a. Electronic state density of HSE06, GGA, LDA. b. Electronic band structure of GGA.

HSE06, GGA, and LDA approximations in denisty functional theory (DFT) were carried out to determine the optical band of the $PbVO_3Cl$. HSE06, GGA, and LDA represent Heyd-Scuseria-Ernzerhof, generalized gradient, and local density, respectively. The band energy values, by using these estimation methodes, were found to be 1.65 eV (LDA), 2.05 eV (GGA), and 3.18 eV (HSE06) in Figure 4.66.a. The methode-band gap energy values are summurized in Table 4.11.

Table 4.11. $PbVO_3CI$ band gap energy values.

Approximation Methodes	Band Gap Energy (eV)
LDA	1.65
GGA	2.05
HSE06	3.18

HSE06, a hybrid approach to approximation band gap energy, brough about an increase in the energy gap, as seen in Figure 4.66.b. When considering the band gap energy values, HSE06 has a larger band gap than the other approximations. $\Gamma - X - S - Y - \Gamma - Z - U - R - T - Z|Y - T|U - X|S - R$ express high symmetry group points in the orthorhombic lattice parameters (see Figure 4.66.b). It is seen in Figure 4.66.b that between the valence band and conduction band gap energy is around 2.05eV. In Figure 4.66.b., a region in which there are not any signals there demonstrates band gap energy value. On the other hand, a region where there are intens peaks shows conduction band and valence band. The DFT and Raman spectroscopy were used to determine the stability of the $PbVO_3CI$ structure. Analysis of the DFT and Raman was carried out at absolute zero (0 K, theoretical acceptance for the DFT calculation) and room temperature, respectively. At same frequency range, it was found that the DFT spectrum results are 107.4, 119.4, 245.2, 380.3, and 973.1cm^{-1}, while Raman spectroscopy spectrum results are 109, 128.9, 227.8, 349, and 962.2 cm^{-1}, respectively. However, some peaks such as 151.4, 460.3, 495.3, 663.6 and 733.5 cm^{-1} have not been matched in the Raman spectrum, these peaks could only be observed in the DFT spectrum. This has been estimated Raman is not active in the peaks that can be observed in the DFT. In the literature, these differences or shifts in the obtained spectrum data are speculated to come from temperature changes (thermal fluctuation effect (Bouvier et al., 2023) and peak overlapping. Moreover, pressure was found to affect not only crystal structure of a material but also IR/Raman phonon frequencies (Ouahrani et al., 2024). Raman, IR and the DFT are widely utilized to search crystalline materials, lattice dynamic for compounds, phonon, vibration modes, Born criteria. Raman-IR modes, IR active modes, and Raman mode symmetry for some vanadate compounds, such as $NdVO_3$, $TbVO_4$, and $InVO_4$ have profoundly been investigated by Errandonea and Garg (Errandonea and Garg, 2018). Here, the $PbVO_3CI$ will be discussed on Born and Phonon criteria and on whether this structure is perovskite or not. Also, the $PbVO_3CI$ will be addressed whether it is a novel halo-oxide perovskite material.

4.7.2.1. Discussion on the Born and Phonon Criteria for the $PbVO_3CI$

In the thesis, the phonon and Born criteria for the $PbVO_3$ has first been discussed. The $PbVO_3$ is in the class of an orthorhombic-*Pnma* space group. Works conducted on

the orthorhombic structure have indicated that these structure are dynamically and mechanically stable with respect to Born and Phonon criteria. Phonon dispersion criteria is a good way to analysis the stability of thermal and dynamic of a material (Li et al., 2018 and Watt, 1979). Δ-sol (Jain et al., 2016), GLLB-SC (Gritsenko et al., 1995), and GW approximation have been used to improve band-gap energy and to determine the electron structure of a material (Onida et al., 2002). Also some hybrid estimations such as B3LYP and HSE have been developed to accurately predict electron correlation and band gap energies in the semiconductors (Wnag et al., 2021).

Romain and Camilla studied on $Ba_2V_2O_7$, $Sr_2V_2O_7$, Ca_2VO_4Cl, Sr_2VO_4Cl, $Mg_3V_2O_8$, and $Zn_3V_2O_8$ materials by using GGA functional PBE approximation. They found that the band gap energy values of these compounds are 3.23, 3.12, 3.21, 3.54, 3.06, and 2.52 eV, respectively. It can be said that these band energy values are roundly close to HSE06 band gap energy of the $PbVO_3CI$ (Schira and Latouche, 2020).

4.7.2.2. Discussion on Perovskite Material for the $PbVO_3CI$ (is the $PbVO_3CI$ a perovskite?)

Perovskite materials have profoundly been studied for theoretical and experimental researches. Perovskites have various properties such as optoelectronic, electronic, ionic conductivity, piezoelectricity, and ferroelectricty. Perovskite materials are widely used in engineering study and industry because of their a large range of application. Halide perovskite materials offer high performance properties in solar cell applications. Also, due to their flexibility, these materials give a significant opportunity to improve material science. Perovskites can be classified as metals, insulators, and semiconductors (Nouri et al., 2024).

In the literature, $PbVO_3$ (not contain chloride element) structure is in the perovskite class and has been studied by Okos and colleagues. Local spin density approximation (LSDA) calculation studied on $PbVO_3$ structure indicates that Raman frequencies are 190 cm^{-1} (lead motion in the cell), 408 cm^{-1} (cation-oxygen interaction), and 838 cm^{-1} (vanadium-oxygen bond stretching) (Singh, 2006). Raman signals of $PbVO_3$ studied by Okos et al. and the $PbVO_3CI$ are similar, but there are light shifts in the Raman frequencies for the $PbVO_3CI$. These shifts can result from chloride elements that are probably in the cell. Here, the question is whether the $PbVO_3CI$ structure is perovskite

material or not, if perovskite, which class belongs to. In the light of the literature, Dai and colleagues in 2000 and 2001 studied various halo-oxide (halide element + oxygen) perovskites such as $ACuO_{2-\delta}X_{\sigma}$ (A = $Sr_{0.63}Ca_{0.27}$, X= F, Cl) (Dai et al., 2001), $AMn_{1-x}Cu_xO_{3-\delta}$ (A = $La_{0.8}Ba_{0.2}$) (Dai et al., 2001) $La_{1-x}Sr_xFeO_{3-\delta}X_{\sigma}$ (X=F, CI) (Dai et al., 2000) and $YBa_2Cu_3O_{7-\delta}X_{\sigma}$ (X = F, Cl). (Dai et al., 2001). Considering Dai's studies, it can be said that the $PbVO_3CI$ structure matches with ABO_3X (A: Ca, Ba, Sr, and Pb, B: Fe, Co, V, and Ni, X: F, CI) structure, and matches with these compounds in the aspect of the structure. Therefore, it can be suggested that the $PbVO_3CI$ structure is a halo-oxide perovskite class. The $PbVO_3CI$ can also be a novel-halo-oxide perovskite class because, as far as I know, there is no information in the literature that this structure is a perovskite material or is discussed as perovskite. Moreover, we think that the $PbVO_3CI$ structure fits in the rule of the Goldschmidt torelance factor ($0.75<t<1.1$) when $PbVO_3$ studied by Okos et al. is considered. This structure can be a novel halo-oxide material.

4.7.3. Conclution and Future Perspective

$NaVO_3$, $PbCI_2$, and boric acid were used to synthesize $PbVO_3CI$. We showed the $PbVO_3CI$ is semicondutor by using different DFT approximations. The band gap energies of the $PbVO_3CI$ were calculated by using DFT approximations; HSE06, GGA, and LDA. These calculations suggest that the $PbVO_3Cl$ has three possible band gap energies: 1.65 eV, 2.05 and 3.18 eV (see Table 4.11). More research is needed to determine high-efficiency and cost-effective materials. The $PbVO_3Cl$ can be a particularly interesting semiconductor, we discussed its electronic band structure, band gap, and Born-Phonon criteria. The first time, we dealt with its halo-oxide perovskite and we showed that this structure is able to be a new halo-oxide perosvkite type. Next, further research is required to determine its electrochemical properties and catalytic activity. We will investigate the $PbVO_3Cl$ can be used for SOFC as membrane. Photoanode, photocathode, cathode material for batteries, electrochemical performance, water splitting, and photovoltaic will be discussed and investigated for other properties of the $PbVO_3Cl$ in the next studies.

CHAPTER 5

CONCLUSION

In this thesis, advanced energy-related materials were synthesized, characterized, and investigated thier electrochemical properties. These materials were targeted to present a solution for global energy problems. Perovskite materials, here BSCF, silver-doped-BSCF, and novel BSNF, were synthesized and characterized. Also, the electrochemical properties of these materials were investigated. It was shown that the BSCF with doping silver exhibits a better electrochemical property than the BSCF. Moreover, thanks to Goldschmidt tolerance factor (t), these materials were shown in the perovskite class ($0.77<x<1.1$). It is quite obvious that Novel BSNF material is corresponded to the Goldschmidt tolerance factor. Novel BSNF and Ag-doped BSCF materials can be promising for energy applications, especially water splitting (OER-HER), and membrane studies in the solid oxide fuel cells

In the thesis, three ink formulations have been developed to fabricate multi-metal oxides for catalayst, especially water spitting to generate hydrogen gas for energy. Three trials were executed to optimize the inks. Also, for optimaztion of the inks, the viscosity and surface tension were measured. It was shown that “Third trial” was printable ink. This ink were used in the all synthesis of mutli-metal oxides. Binary combination metal oxides on the FTO as substrate were printed by using inkjet printer machine. Among the binary(pseudobinary) combinations, the oxide of the Ni-Fe (%30:%70) showed maximum current density at around 7.5 mA/cm^2. However, the binary combination of the Ni-Cr and the Ni-Cu exhibited minimum current density. It was indicated that the printable inks (3.Trial formulation) abide by the rule of Ohnesorge number ($1<Z<10$).

Nickel hydroxide as cathode material for Ni-based battery was fabricated by using the urea decomposition method. Both alpha-$Ni(OH)_2$ and beta-$Ni(OH)_2$ forms were synthesized and characterized by XRD, SEM, and CV. Cu, Al, Co, and Zn doped beta $Ni(OH)_2$ were measured for their electrochemical properties, then were compared electrochemical performances in terms of current density and capacitance. XRD peaks depicted that alpha form $Ni(OH)_2$ was amorphous structure. Also, the capacity of beta $Ni(OH)_2$ cathode was analyzed by using Battery Tester machine. The capacity of the cathode was measured at different C rate. Moreover, different battery cells have been

done to optimize its capacity and to get maximum performance. Moreover, C rate effect binder effect, and electrolyte effect were profoundly discussed how to affect the capacity of the cell. In the study, NMC622 cathode material for Li-ion battery was synthesized using solid state methode (ball milling) and characterized by ICP-OES, SEM, and XRD. Alsa the capacity study of the NMC622 was done by using battery tester. The NMC622 showed the Coulombic efficiency of over %95. However, it can be said that the synthesized NMC622 active material has exhibited a low specific capacity when considering actual and theoritical value of NMC622 active material. Factors, such as oxygen, impurity, moisture, the cathode of thickness, and roughness affect considerably the capacity of the NMC622. The capacity of the cathode was found around 125 $mA.g^{-1}$, especially at first cycles.

In the last part of thesis, sodium vanadate, boric acid, and lead (II) chloride were used to fabricated $PbVO_3CI$. It was showed that the $PbVO_3CI$ is semiconductor by estimations methode of DFT. Approximation methodes; HSE06, GGA, and LDA were used and the possible bandgap energy values of the $PbVO_3CI$ is 3.18 eV, 2.05 eV, and 1.65 eV, respectively. We discussed Born-Phonon criteria, electronic structure, and halo-oxide perovskite of the $PbVO_3CI$. The $PbVO_3CI$ can be a new halo-oxide perovskite type

Here, nickel hydroxide cathode for Ni-based battery and NMC622 cathode for Li-ion battery were widely discussed and done optimization studies. Perovskite materials (BSCF, Ag-BSCF, and novel BSNF) were dicussed their electrochemical properties and their Goldschmidt tolerance factors were calculated. The printable ink formulations were developed and their viscosity and surface tension were discussed for optimization studies. Binary multimetal oxides were synthesized using the developed printable inks for catalyst studies. Also, the various properties of the $PbVO_3CI$ were widely discussed. Some of its properties, such as halo-oxide perovskite and Born-Phonon were first dealt with in the thesis. We suggest that he synthesized materials in the thesis are able to have a promising future for energy application studies. In future perspective studies, energy devices (SOFC, solar cells, etc) will be developed to show the usability of the synthesized materials in this thesis, the properties of the materials will be profoundly researched.

REFERENCES

Abbas, S.; Iqbal, M.; Kim, S. H.; Khan, H. A.; Jung, K.-D. Facile Synthesis of Alfa-Nickel Hydroxide by an Ultrasound Assisted Method and Its Application in Ener gy Storage Devices **2019**, *474*, 218-226. DOI:10.1016/j.apsusc.2018.03.036.

Abramavicius, D.; Valkunas, L. Artificial Photosynthesis. *Advances in botanical research* **2016**, 129–167. DOI: 10.1016/bs.abr.2016.04.001.

Ahmad, S.; Kazim, S.; GrätzelM.; Wiley-Vch. *Perovskite Solar Cells: Materials, Processes, and Devices*; Weinheim Wiley-Vch, 2022.

Ahmadrezaei, M.; Muchtar A.; Muhamad, N.; Tan, C. Y.; Edy Herianto Majlan. Electrochemical and Microstructural Characteristics of Nanoperovskite Oxides Ba0.2Sr0.8Co0.8Fe0.2O3−δ (BSCF) for Solid Oxide Fuel Cells. *Ceramics International* **2013**, *39*(1), 439–444. DOI: 10.1016/j.ceramint.2012.06.045.

Alibabaei, L.; Luo, H.; House, R. L.; Hoertz, P. G.; Lopez, R.; Meyer, T. J. Applications of Metal Oxide Materials in Dye Sensitized Photoelectrosynthesis Cells for Making Solar Fuels: Let the Molecules Do the Work. *Journal of Materials Chemistry A* **2013**, *1* (13), 4133–4133. DOI: 10.1039/c2ta00935h.

Almeida, J. R.; Moura, M. N.; Barrada, R. V.; Sartori, E. M.; Tereza, M.; Aparecida, S.; Maria; Freitas, M. B. J. G.; Brandão, G. P. Composition Analysis of the Cathode Active Material of Spent Li-Ion Batteries Leached in Citric Acid Solution: A Study to Monitor and Assist Recycling Processes. *Science of The Total Environment* **2019**, *685*, 589–595. DOI: 10.1016/j.scitotenv.2019.05.243.

Althurthi, S. B.; Rajashekara, K.; Debnath, T. Comparison of EV Fast Charging Protocols and Impact of Sinusoidal Half-Wave Fast Charging Methods on Lithium-Ion Cells. *World Electric Vehicle Journal* **2024**, *15* (2), 54-54. DOI: 10.3390/wevj15 020054.

Arifin, K.; Majlan, E. H.; Wan Daud, W. R.; Kassim, M. B. Bimetallic Complexes in Artificial Photosynthesis for Hydrogen Production: A Review. *International Journal of Hydrogen Energy* **2012**, *37* (4), 3066–3087. DOI: 10.1016/j.ijhydene. 2011.11.052.

Assirey, E. A. R. Perovskite Synthesis, Properties and Their Related Biochemical and Industrial Application. *Saudi Pharmaceutical Journal* **2019**, *27* (6), 817–829. DOI: 10.1016/j.jsps.2019.05.003.

Bachmeier, A. S. J. L. *Metalloenzymes as Inspirational Electrocatalysts for Artificial Photosynthesis : From Mechanism to Model Devices*; Springer: Cham, Switzerland, 2017.

Baeck, S. H.; Jaramillo, T. F.; Brändli, C.; McFarland, E. W. Combinatorial Electrochemical Synthesis and Characterization of Tungsten-Based Mixed-Metal Oxides. *Journal of Combinatorial Chemistry* **2002**, *4* (6), 563–568. DOI: 10.1021/cc020014w.

Baird, S. G.; Sparks, T. D. What Is a Minimal Working Example for a Self-Driving Laboratory? *Matter* **2022**, *5* (12), 4170–4178. DOI: 10.1016/j.matt.2022.11.007.

Bak, S.-M.; Hu, E.; Zhou, Y.-N.; Yu, X.; Senanayake, S. D.; Cho, S.-J.; Kim, K. S.; Kyung Yoon Chung; Yang, X.-Q.; Nam, K.-W. Structural Changes and Thermal Stability of Charged $LiNi_xMn_yCo_zO_2$ Cathode Materials Studied by Combined *in Situ* Time-Resolved XRD and Mass Spectroscopy. *ACS Applied Materials & Interfaces* **2014**, *6* (24), 22594–22601. DOI: 10.1021/am506712c.

Bastakoti, B. P.; Huang, H.-S.; Chen, L.-C.; Wu, K. C.-W. .; Yamauchi, Y. Block Copolymer Assisted Synthesis of Porous α-Ni(OH)2 Microflowers with High Surface Areas as Electrochemical Pseudocapacitor Materials. *Chemical Communications* **2012**, *48* (73), 9150. DOI: 10.1039/c2cc32945j.

Bode, H.; Dehmelt, K.; Witte, J. Zur Kenntnis Der Nickelhydroxidelektrode—I.Über Das Nickel (II)-Hydroxidhydrat. *Electrochimica Acta* **1966**, *11* (8), 1079–1087. DOI: 10.1016/0013-4686(66)80045-2.

Boiko, D. A.; MacKnight, R.; Kline, B.; Gomes, G. Autonomous Chemical Research with Large Language Models. *Nature* **2023**, *624* (7992), 570–578. DOI: 10.1038/s41586-023-06792-0.

Bouvier, P.; Alireza Sasani; Bousquet, E.; Mael Guennou; Joaquim Agostinho Moreira. Lattice Dynamics and Raman Spectrum of Supertetragonal PbVO3. *Journal of Physics and Chemistry of Solids* **2023**, *173*, 111092–111092. DOI:10.1016/j.jpcs.2022.111092.

Bruce, P. G.; Freunberger, S. A.; Hardwick, L. J.; Tarascon, J.-M. Li–O2 and Li–S Batteries with High Energy Storage. *Nature Materials* **2011**, *11* (1), 19–29. DOI: 10.1038/nmat3191.

Chang, L.; Yang, W.; Cai, K.; Bi, X.; Wei, A.; Yang, R.; Liu, J. A Review on Nickel-Rich Nickel–Cobalt–Manganese Ternary Cathode Materials $LiNi_{0.6}Co_{0.2}Mn_{0.2}O_2$ for Lithium-Ion Batteries: Performance Enhancement by Modification. *Materials Horizons* **2023**, *10* (11), 4776–4826. DOI: 10.1039/d3mh01151h.

Chen, L.; Shaw, L. L. Recent Advances in Lithium–Sulfur Batteries. *Journal of Power Sources* **2014**, *267*, 770–783. DOI: 10.1016/j.jpowsour.2014.05.111.

Chen, Z.; Xu, C.; Zhao, F.; Xi, S.; Li, W.; Huang, M.; Cai, B.; Gu, M.; Wang, H.-L.; Xiang, X.-D. High-Performance Oxygen Evolution Reaction Electrocatalysts Discovered via High-Throughput Aerogel Synthesis. *ACS Catalysis* **2022**, *13* (1), 601–611. DOI: 10.1021/acscatal.2c03684.

Chiku, M.; Yihan, T.; Higuchi, E.; Inoue, H. Manganese Oxides as Positive Electrode Materials for Rechargeable Aluminum Batteries. *Journal of Alloys and Compounds* **2023**, *969*, 172430–172430. DOI: 10.1016/j.jallcom.2023.172430.

Cho, I.; Ju, Y. Text Mining Method to Identify Artificial Intelligence Technologies for the Semiconductor Industry in Korea. *World Patent Information* **2023**, *74*, 102212–102212. DOI: 10.1016/j.wpi.2023.102212.

Chou, L. Y. T.; Ming, K.; Chan, W. C. W. Strategies for the Intracellular Delivery of Nanoparticles. *Chem. Soc. Rev.* **2011**, *40* (1), 233–245. DOI: 10.1039/c0cs00003e.

Cogdell, R. J.; Brotosudarmo, T. H.; Gardiner, A. T.; Sanchez, P. M.; Cronin, L. Artificial Photosynthesis – Solar Fuels: Current Status and Future Prospects. *Biofuels* **2010**, *1* (6), 861–876. DOI: 10.4155/bfs.10.62.

Compton, R. G.; Enno Kätelhön; Laborda, E.; Ward, K. R. *Understanding Voltammetry*; World Scientific, 2020.

Dahlin, G. R.; Strøm, K. E. *Lithium Batteries : Research, Technology, and Applications*; Nova Science Publishers: New York, 2010.

Dai, H. X.; Au, C. T.; Chan, Y.; Hui, K. C.; Leung, Y. L. Halide-Doped Perovskite-Type AMn1−XCuxO3−δ (a = La0.8Ba0.2) Catalysts for Ethane-Selective Oxidation to Ethene. *Applied Catalysis A General* **2001**, *213* (1), 91–102. DOI: 10.1016/s0926-860x(00)00880-2.

Dai, H. X.; He, H.; Ng, C. F.; Au, C. T. Halo-Oxide ACuO2−ΔXσ (A=Sr0.63Ca0.27, X=F, Cl) Catalysts Active and Durable for Ethane Selective Oxidation to Ethene. *Journal of Molecular Catalysis A Chemical* **2001**, *171* (1-2), 217–227. DOI: 10.1016/s1381-1169(01)00105-4.

Dai, H. X.; Ng, C. F.; Au, C. T. Perovskite-Type Halo-Oxide La1−XSrxFeO3−ΔXσ (X=F, Cl) Catalysts Selective for the Oxidation of Ethane to Ethene. *Journal of Catalysis* **2000**, *189* (1), 52–62. DOI: 10.1006/jcat.1999.2677.

Dell, R.; D A J Rand; Society, R. *Understanding Batteries*; Royal Society Of Chemistry: Cambridge, 2001.

Desilvestro,J.; Corrigan, D. A.; Weaver, M. J. Characterization of Redox States of Nickel Hydroxide Film Electrodes by in Situ Surface Raman Spectroscopy. *Journal of The Electrochemical Society* **1988**, *135* (4), 885–892. DOI:10.1149/1.2095818.

Diao, W.; Xing, Y.; Saxena, S.; Pecht, M. Evaluation of Present Accelerated Temperature Testing and Modeling of Batteries. *Applied Sciences* **2018**, *8* (10), 1786. https://doi.org/10.3390/app8101786.

Dickinson, E. J. F.; Wain, A. J. The Butler-Volmer Equation in Electrochemical Theory: Origins, Value, and Practical Application. *Journal of Electroanalytical Chemistry* **2020**, *872*, 114145. DOI: 10.1016/j.jelechem.2020.114145.

Ding, M.; Guo, Z.; Zhou, L.; Fang, X.; Zhang, L.; Zeng, L.; Xie, L.; Zhao, H. One-Dimensional Zinc Oxide Nanomaterials for Application in High-Performance Advanced Optoelectronic Devices.*Crystals* **2018**, *8* (5), 223. DOI:10.3390/cryst 8050223.

Doyle, R. L.; Godwin, I. J.; Brandon, M. P.; Lyons, M. E. G. Redox and Electrochemical Water Splitting Catalytic Properties of Hydrated Metal Oxide Modified Electrodes. *Physical Chemistry Chemical Physics* **2013**, *15* (33), 13737. DOI: 10 .1039/c3cp51213d.

Ekawati, K. D. R.; Sholikah, A. P.; Yudha, C. S.; Widiyandari, H.; Purwanto, A. Comparative Study of NCA Cathode Material Synthesis Methods towards Their Structure Characteristics. *2018 5th International Conference on Electric Vehicular Technology (ICEVT)* **2018**. DOI: 10.1109/icevt.2018.8628433.

El Idrissi, A.; El ouardi, M.; Ait Ahsaine, H.; BaQais, A.; Saadi, M.; Arab, M. Current Advances on Nanostructured Oxide Photoelectrocatalysts for Water Splitting: A Comprehensive Review. *Surfaces and Interfaces* **2024**, *45*, 103850–103850. DOI: 10.1016/j.surfin.2024.103850.

Elong, K.; Kasim, M. F.; Azahidi, A.; Osman, Z. LiNi0.3Mn0.3Co0.3O2 (NMC 111) Cathode Material Synthesize via Combustion Method: Effect of Combustion Fuel on Structure, Morphology and Their Electrochemical Performances. *Materials Today Proceedings* **2023**. DOI: 10.1016/j.matpr.2023.02.283.

Errandonea, D.; Garg, A. B. Recent Progress on the Characterization of the High-Pressure Behaviour of AVO4 Orthovanadates. **2018**, *97*, 123–169. DOI:10.1016/j.pmats ci.2018.04.004.

Fierro, J. L. G. *Metal Oxides*; CRC Press, 2005.

Fu, W.; Ricciardulli, A. G.; Akkerman, Q. A.; John, R. A.; Tavakoli, M. M.; Essig, S.; Kovalenko, M. V.; Saliba, M. Stability of Perovskite Materials and Devices. *Materials Today* **2022**, *58*, 275–296. DOI: 10.1016/j.mattod.2022.06.020.

Fujiwara, H.; Collins, R. W.; Springerlink (Online Service. *Spectroscopic Ellipsometry for Photovoltaics : Volume 2: Applications and Optical Data of Solar Cell Materials*; Springer International Publishing: Cham, 2018.

Garcia, J. C.; Bareño, J.; Yan, J.; Chen, G.; Hauser, A.; Croy, J. R.; Iddir, H. Surface Structure, Morphology, and Stability of Li(Ni1/3Mn1/3Co1/3)O2 Cathode Material. *The Journal of Physical Chemistry C* **2017**, *121* (15), 8290-8299. DOI: 10.1021/acs.jpcc.7b00896.

Gautam, M.; Sandeep Kanade; Kale, B. B. Electrochemical Energy Storage and Conversion Applications of Graphene Oxide: A Review. *Energy & Fuels* **2023**, *37* (22), 17134–17160. DOI:10.1021/acs.energyfuels.3c02933.

Ghatak, K.; Basu, S.; Das, T.; Sharma, V.; Kumar, H.; Datta, D. Effect of Cobalt Content on the Electrochemical Properties and Structural Stability of NCA Type Cathode Materials. *Physical Chemistry Chemical Physics* **2018**, *20* (35), 22805–22817. DOI: 10.1039/c8cp03237h.

Ginley, D. S.; Cahen, D. *Fundamentals of Materials for Energy and Environmental Sustainability*; Cambridge University Press ; [S.L: Cambridge, 2012.

Godinho, M. Isabel.; Catarino, M. Alice.; da Silva Pereira, M. I.; Mendonça, M. H.; Costa, F. M. Effect of the Partial Replacement of Fe by Ni And/or Mn on the Electrocatalytic Activity for Oxygen Evolution of the CoFe2O4 Spinel Oxide Electrode. *Electrochimica Acta* **2002**, *47* (27), 4307–4314. DOI: 10.1016/s0013-4686(02)00434-6.

Goldstein, J. I.; Newbury, D. E.; Michael, J. R.; Ritchie, N. W.; Scott, J. H. J.; Joy, D. C. *Scanning Electron Microscopy and X-Ray Microanalysis.*; Springer-Verlag New York: S.L., 2018.

Gong, M.; Dai, H. A Mini Review of NiFe-Based Materials as Highly Active Oxygen Evolution Reaction Electrocatalysts. *Nano Research* **2014**, *8* (1), 23–39. DOI: 10.1007/s12274-014-0591-z.

Goodenough, J. B.; Mizuchima, K. Electrochemical Cell with New Fast Ion Conductors, US 4302518, November 24, 1981.

Greenberg, J. *X-Ray Diffraction Imaging*; CRC Press, 2018.

Gritsenko, O.; van Leeuwen, R.; van Lenthe, E.; Baerends, E. J. Self-Consistent Approximation to the Kohn-Sham Exchange Potential. *Physical Review A* **1995**, *51* (3), 1944–1954. DOI: 10.1103/physreva.51.1944.

Guevarra, D.; Haber, J. A.; Wang, Y.; Zhou, L.; Kan, K.; Richter, M. H.; Gregoire, J. M. High Throughput Discovery of Complex Metal Oxide Electrocatalysts for the Oxygen Reduction Reaction. *Electrocatalysis* **2021**, *13* (1), 1–10. DOI: 10.1007/s12678-021-00694-3.

Guo, Z.; Liaw, B. Y.; Qiu, X.; Gao, L.; Zhang, C. Optimal Charging Method for Lithium Ion Batteries Using a Universal Voltage Protocol Accommodating Aging. *Journal of Power Sources* **2015**, *274*, 957–964. DOI: 10.1016/j.jpowsour.2014.10.185.

Harunsani, M. H. *Characterisation of Mixed-Metal Oxides Prepared by Hydrothermal Synthesis*; 2013.

Hu, W.-K.; Noréus, D. Alpha Nickel Hydroxides as Lightweight Nickel Electrode Materials for Alkaline Rechargeable Cells. *Chemistry of Materials* **2003**, *15* (4), 974–978. DOI: 10.1021/cm021312z.

Huang, X.; Li, Y.; Acharya, A. B.; Sui, X.; Meng, J.; Teodorescu, R.; Stroe, D.-I. A Review of Pulsed Current Technique for Lithium-Ion Batteries. *Energies* **2020**, *13* (10), 2458. DOI: 10.3390/en13102458.

Huang, X.; Zhou, R.; Xin, L.; Yang, X.; Cheng, J.; Yan, J. Experimental Research and Multi-Physical Modeling Progress of Zinc-Nickel Single Flow Battery: A Critical Review. *Advances in Applied Energy* **2023**, *12*, 100154–100154. DOI: 10.1016/j.adapen.2023.100154.

Ihalainen, M.; Miika Kortelainen; Arunas Mesceriakovas; Tommi Karhunen; Sara-Maaria Mesceriakove; Lindberg, D.; Jari T.T. Leskinen; Timo Kankaanpää; Jorma Jokiniemi; Lähde, A. Synthesis of Solid NMC622 Particles by Spray Drying, Post-Annealing and Lithiation. *Advanced Powder Technology* **2023**, *34* (10), 104187–104187. DOI: 10.1016/j.apt.2023.104187.

Ilhan, T. *Synthesizing Cation Doped Stable Alpha Nickel Hydroxide Having Low Self Discharge Rate by Chemical Precipitation* ; YÖK: Türkiye, 2022; Vol. 720769.

Ito, Y.; Nyce, M.; Plivelich, R.; Klein, M.; Steingart, D.; Banerjee, S. Zinc Morphology in Zinc–Nickel Flow Assisted Batteries and Impact on Performance. *Journal of Power Sources* **2011**, *196* (4), 2340–2345. DOI:10.1016/j.jpowsour. 201 0.09 .0 65.

Jain, A.; Shin, Y.; Persson, K. A. Computational Predictions of Energy Materials Using Density Functional Theory. *Nature Reviews Materials* **2016**, *1* (1), 1–13. DOI: 10.1038/natrevmats.2015.4.

Jawad, N. H.; Yahya, A. A.; Al-Shathr, A. R.; Salih, H. G.; Rashid, K. T.; Al-Saadi, S.; AbdulRazak, A. A.; Salih, I. K.; Zrelli, A.; Alsalhy, Q. F. Fuel Cell Types, Properties of Membrane, and Operating Conditions: A Review. *Sustainability* **2022**, *14* (21), 14653. DOI:10.3390/su142114653.

Jiang, H.; Zhao, T.; Li, C.; Ma, J. Hierarchical Self-Assembly of Ultrathin Nickel Hydroxide Nanoflakes for High-Performance Supercapacitors. *Journal of Materials Chemistry* **2011**, *21* (11), 3818. DOI:10.1039/c0jm03830j.

Jiang, Z.; Chen, S.; Wei, C.; Zhang, Z.; Wu, Z.; Luo, Q.; Ming, L.; Zhang, L.; Yu, C. Enabling Superior Electrochemical Performance of NCA Cathode in Li5.5PS4.5Cl1.5-Based Solid-State Batteries with a Dual-Electrolyte Layer. *Chinese Chemical Letters* **2024**, *35* (4), 0108561–108561. DOI: 10.1016/j.cclet. 2023.108561.

Joachim, H. H.; Rees, D. H. The Nicomachean Ethics, *Ethics* **1952**, *62* (4), 300–301. DOI: 10.1086/290853.

Kakavandi, B.; Moradi, M.; Hasanvandian, F.; Bahadoran, A.; Mohebolkhames, E.; Golshan, M.; Ganachari, S.; Aminabhavi, T. M. Visible Light-Assisted S-Scheme P- and N-Type Semiconductors Anchored onto Graphene for Increased Photocatalytic H2 Production via Water Splitting. *Chemical engineering journal (1996. Print)* **2024**, 150399–150399. DOI: 10.1016/j.cej.2024.150399.

Kannan, K.; Chanda, D.; Mikiyas Mekete Meshesha; Yang, B. Impressive Efficiency of Zinc Oxide-Manganese Oxide/MAX Composite in Two-Electrode System for Photovoltaic-Electrolyzer Water Splitting. *Colloids and Surfaces A Physicochemical and Engineering Aspects* **2024**, *689*, 133599–133599. DOI: 10.1016/j.colsurfa.2024.133599.

Keil, P.; Jossen, A. Charging Protocols for Lithium-Ion Batteries and Their Impact on Cycle Life—an Experimental Study with Different 18650 High-Power Cells. *Journal of Energy Storage* **2016**, *6*, 25–141. DOI: 10.1016/j.est.2016.02.005.

Kiehne, H. A. *Battery Technology Handbook*; Marcel Dekker: New York, 2003.

Kim, K.-B.; Nam, K.-W. A Study of the Preparation of NiO_x Electrode via Electrochemical Route for Supercapacitor Applications and Their Charge Storage Mechanism. *Journal of The Electrochemical Society* **2002**, *149* (3), A346. DOI: 10.1149/1.1449951.

Konarova, M.; Aslam, W.; Ge, L.; Ma, Q.; Tang, F.; Rudolph, V.; Beltramini, J. Enabling Process Intensification by 3 D Printing of Catalytic Structures. **2017**, *9* (21), 4132–4138. DOI: 10.1002/cctc.201700829.

Kudo, A.; Miseki, Y. Heterogeneous Photocatalyst Materials for Water Splitting. *Chem. Soc. Rev.* **2009**, *38* (1), 253–278. DOI: 10.1039/b800489g.

Lawson, S.; Li, X.; Thakkar, H.; Rownaghi, A. A.; Rezaei, F. Recent Advances in 3D Printing of Structured Materials for Adsorption and Catalysis Applications. *Chemical Reviews* **2021**, *121* (10), 6246–6291. DOI: 10.10 21/acs .chemrev .1c0 0060.

Lee, J. W.; Ko, J. M.; Kim, J.-D. Hierarchical Microspheres Based on α-$Ni(OH)_2$ Nanosheets Intercalated with Different Anions: Synthesis, Anion Exchange, and Effect of Intercalated Anions on Electrochemical Capacitance. *Journal of Physical Chemistry C* **2011**, *115* (39), 19445–19454. DOI: 10.1021/jp206379h.

Lee, M. *X-Ray Diffraction for Materials Research*; CRC Press, 2017.

Lesch, A.; Cortés-Salazar, F.; Victor Costa Bassetto; Amstutz, V.; Girault, H. H. Inkjet Printing Meets Electrochemical Energy Conversion. *Chimia* **2015**, *69* (5), 284–284. DOI: 10.2533/chimia.2015.284.

Li, H.; Li, J.; Ma, X.; Dahn, J. R. Synthesis of Single Crystal $LiNi_{0.6}Mn_{0.2}Co_{0.2}O_2$with Enhanced Electrochemical Performance for Lithium Ion Batteries. *Journal of The Electrochemical Society* **2018**, *165* (5), A1038–A1045. DOI:10.1149 /2.09 518 0 5jes.

Li, J.; Luo, F.; Tian, X.; Lei, Y.; Yuan, H.; Xiao, D. A Facile Approach to Synthesis Coral-like Nanoporous β-Ni(OH) 2 and Its Supercapacitor Application. *Journal of power sources* **2013**, *243*, 721–727. DOI: 10.1016/j.jpowsour.2013.05.172.

Li, P.; Wang, S.; Wang, S. Unravelling the Synergistic Promotion Effect of Simultaneous Doping Fe and Cr into Cu-Based Spinel Oxide on Methanol Steam Reforming. *International Journal of Hydrogen Energy* **2023**, *48* (49), 18731–18743. DOI: 10.1016/j.ijhydene.2023.01.283.

Li, P.; Xu, H.; Zhang, Y.; Li, Z.; Zheng, S.; Bai, Y. The Effects of al and Ba on the Colour Performance of Chromic Oxide Green Pigment. *Dyes and Pigments* **2009**, *80* (3), 287–291. DOI: 10.1016/j.dyepig.2008.07.016.

Li, Q.; He, Z.; Cao, Q. Theoretical Study of the R3c-To-Pnma Phase Transition in BiAlO3. *Computational Materials Science* **2018**, *152*, 211–216. DOI: 10.1016/j.commatsci.2018.05.053.

Li, T.; Yuan, X.-Z.; Zhang, L.; Song, D.; Shi, K.; Bock, C. Degradation Mechanisms and Mitigation Strategies of Nickel-Rich NMC-Based Lithium-Ion Batteries. *Electrochemical Energy Reviews* **2019**, *3* (1), 43–80. DOI:10.1007/s41918-019-00053-3.

Li, W.; Jaka Sunarso; Yang, Y.; Chen, Y.; Ge, C.; Wang, W.; Guo, Y.; Ran, R.; Zhou, W. Strategies for Improving Oxygen Ionic Conducting in Perovskite Oxides and Their Practical Applications. *Energy Reviews* **2024**, *3* (4), 100085–100085. DOI: 10.1016/j.enrev.2024.100085.

Li, X.; Abdo-Alslam Alwakwak; Rezaei, F.; Rownaghi, A. A. Synthesis of Cr, Cu, Ni, and Y-Doped 3D-Printed ZSM-5 Monoliths and Their Catalytic Performance for *N*-Hexane Cracking. *ACS Applied Energy Materials* **2018**, *1* (6), 2740–2748. DOI: 10.1021/acsaem.8b00412.

Linden, D.; Reddy, T. *Handbook of Batteries*; McGraw-Hill Professional, 2002.

Linden, D. Batteries and Fuel cells. In *Standard Handbook of Electronic Engineering*. McGraw-Hill. 2005.

Liu, B.; Wu, T.; Ma, F.; Zhong, C.; Hu, W. Long-Life and Highly Utilized Zinc Anode for Aqueous Batteries Enabled by Electrolyte Additives with Synergistic Effects. *ACS Applied Materials & Interfaces* **2022**, *14* (16),18431–18438. DOI: 10.1021/acsami.2c00949.

Liu, B.; Wang, X. Y.; Yuan, H. T.; Zhang, Y. S.; Song, D. Y.; Zhou, Z. X. Physical and Electrochemical Characteristics of Aluminium-substituted Nickel Hydroxide. Journal of Applied Electrochemistry **1999**, 29, 853-858.

Liu, C.; Nan, J.; Zuo, X.; Xiao, X.; Shu, D. Synthesis and Electrochemical Characteristics of an Orthorhombic LiMnO2 Cathode Material Modified with Poly(Vinyl-Pyrrolidone) for Lithium Ion Batteries. *International Journal of Electrochemical Science* **2012**, *7* (8), 7152–7164. DOI: 10.1016/s1452-3981(23)15775-0.

Liu, M.; Wang, P.; Zhang, W.; He, H.; He, G.; Xu, S.; Yao, L.; Miller, T. S. Strategies for PH Regulation in Aqueous Zinc Ion Batteries. *Energy Storage Materials* **2024**, *67*, 103248. DOI: 10.1016/j.ensm.2024.103248.

Liu, Q.; Song, Y.; Li, R.; Houfu Lv; Feng, W.; Shen, Y.; Zhang, X.; Wang, G.; Bao, X. A Vanadium-Doped BSCF Perovskite for CO2 Electrolysis in Solid Oxide Electrolysis Cells. *International Journal of Hydrogen Energy* **2021**, *46* (38), 19814–19821. DOI: 10.1016/j.ijhydene.2021.03.134.

Liu, X.; Shen, Y.; Yang, R.; Zou, S.; Ji, X.; Shi, L.; Zhang, Y.; Liu, D.; Xiao, L.; Zheng, X.; Li, S.; Fan, J.; Stucky, G. D. Inkjet Printing Assisted Synthesis of Multicomponent Mesoporous Metal Oxides for Ultrafast Catalyst Exploration. *Nano Letters* **2012**, *12* (11), 5733–5739. DOI: 10.1021/nl302992q.

Liu, Y.; Zhang, X.; Jiang, Y.; Zhang, M.; Ma, Y. Critical Role of Empty In-Gap States in the Photocatalytic Water Splitting on Carbon Nitride Nanosheets. *Applied Surface Science*.**2024**, *644*, 158806–158806. DOI: 10.1016/j.apsusc.2023.158806.

Mabbott, G. A. Electroanalytical Chemistry: Principles, Best practices, and Case Studies. John Wiley & Sons. 2020.

Magzoub, F.; Li, X.; Al-Darwish, J.; Rezaei, F.; Rownaghi, A. A. 3D-Printed ZSM-5 Monoliths with Metal Dopants for Methanol Conversion in the Presence and Absence of Carbon Dioxide. *Applied Catalysis B: Environmental* **2019**, *245*, 486–495. DOI: 10.1016/j.apcatb.2019.01.008.

Maleki, H.; Bertola, V. Recent Advances and Prospects of Inkjet Printing in Heterogeneous Catalysis. *Catalysis Science.& Technology* **2020**, *10* (10), 3140–3159. DOI: 10.1039/d0cy00040j.

Mavis, B.; Akinc, M. Three-Component Layer Double Hydroxides by Urea Precipitation: Structural Stability and Electrochemistry. *Journal of Power Sources* **2004**, *134* (2), 308–317. DOI: 10.1016/j.jpowsour.2004.03.056.

McAuliffe, R. D.; Kamm, G. E.; McDermott, M. J.; Hermann, R. P.; Neyanel Vasquez-Garcia; Sacci, R. L.; Persson, K. A.; Chapman, K. W.; Veith, G. M. Direct Mechanochemical Synthesis, Phase Stability, and Electrochemical Performance of α-$NaFeO_2$. *Inorganic Chemistry* **2023**, *62* (8), 3358–3367. DOI: 10.1021/acs.inorgchem.2c03286.

McCrory, C. C. L.; Jung, S.; Peters, J. C.; Jaramillo, T. F. Benchmarking Heterogeneous Electrocatalysts for the Oxygen Evolution Reaction. *Journal of the American Chemical.Society* **2013**, *135* (45), 16977–16987. DOI: 10.1021/ja407115p.

Miao, L.; Wang, J.; Zhang, P. Review on Manganese Dioxide for Catalytic Oxidation of Airborne Formaldehyde. *Applied Surface Science* **2019**, *466*, 441–453. DOI: 10.1016/j.apsusc.2018.10.031.

Milewski, J.; Świrski, K.; Santarelli, M.; & Leone, P. Advanced Methods of Solid Oxide Fuel Cell Modeling. Springer Science & Business Media. 2011.

Monem, M. A.; Trad, K.; Omar, N.; Hegazy, O.; Mantels, B.; Mulder, G.; Van, P.; Van Mierlo, J.; Lithium-Ion Batteries: Evaluation Study of Different Charging Methodologies Based on Aging Process. *Applied Energy* **2015**, *152*, 143–155. DOI: 10.1016/j.apenergy.2015.02.064.

Morioka, Y.; Narukawa, S.; Itou, T. State-of-The-Art of Alkaline Rechargeable Batteries. *Journal of Power Sources* **2001**, *100* (1-2), 107–116. DOI:10.1016/s0378-7753 (01)00888-6.

Mushtaq, M.; P. Uma Sathyakam; R. Vijayaraghavan. Performance, Comprehension and Applications of Hematite-Based Photoanodes in PEC Water Splitting. *Next Materials* **2024**, *3*, 100159–100159. DOI: 10.1016/j.nxmate.2024.100159.

Müller,P.; Störmer, H.; Meffert, M.; Dieterle, L.; Niedrig, C.; Wagner, S. F.; Ivers-Tiffée, E.; Gerthsen, D. Secondary Phase Formation in $Ba_{0.5}Sr_{0.5}Co_{0.8}Fe_{0.2}O_{3-d}$ Studied by Electron Microscopy. *Chemistry of Materials* **2013**, *25* (4), 564–573. DOI: 10.1021/cm303670m.

Nainggolan, I.; Martina, S. J.; Alva, S.; Li, B.; Nasution, T. I.; Sembiring, A.; Duha, A. S.; Saisa, S.; Rahman, R.; Asrosa, R.; Sensitivity of Chitosan/Reduced Graphene Oxide/Manganese Dioxide Modified Electrodes for Cholesterol Detection Using Cyclic Voltammetry. *South African Journal of Chemical Engineering* **2024**, *48*, 329–336. DOI: 10.1016/j.sajce.2024.03.009.

Nanda, J.; Augustyn, V. *Transition Metal Oxides for Electrochemical Energy Storage*; John Wiley & Sons, 2022.

Neamen, D. A. Semiconductor Physics and Devices: Basic Principles. McGraw-Hill, 2003.

Nouri, T.; Khelfaoui, F.; Amara, K.; Belkharroubi, F.; Al-Douri, Y.; Odeh, A. A.; Al-Samarai, R. A. A First-Principles Investigation of Structural, Mechanical, Electronic and Magnetic Properties of CsMgO3 Perovskite. *Chemical physics* **2024**, 112391–112391. DOI: 10.1016/j.chemphys.2024.112391.

Oh, P.; Ko, M.; Myeong, S.; Kim, Y.; Cho, J. A Novel Surface Treatment Method and New Insight into Discharge Voltage Deterioration for High-Performance 0.4Li2MnO3-0.6LiNi1/3Co1/3Mn1/3O2Cathode Materials. *Advanced Energy Materials* **2014**, *4* (16), 1400631. DOI: 10.1002/aenm.201400631.

Okos, A.; Colin, C.; Darie, C.; Raita, O.; Bordet, P.; Pop, A. Structure and Magnetic Properties of the Layered Perovskite PbVO3. *Journal of Alloys and Compounds* **2014**, *602*, 265–268. DOI: 10.1016/j.jallcom.2014.02.144.

Onida, G.; Reining, L.; Rubio, A. Electronic Excitations: Density-Functional versus Many-Body Green's-Function Approaches. *Reviews of Modern Physics* **2002**, *74* (2), 601–659. DOI: 10.1103/revmodphys.74.601.

Ōsaka, T.; Datta, M. *Energy Storage Systems for Electronics*; Gordon And Breach Science Publishers: Amsterdam, 2000.

Ouahrani, T. ; Muñoz, A.; Franco, R.; Boufatah, R. M.; Bedrane, Z.; Errandonea, D. High-Pressure Properties of Thallium Orthovanadate from Density-Functional Theory Calculations. *Journal of Alloys and Compounds* **2024**, *978*, 173483–173483. DOI: 10.1016/j.jallcom.2024.173483.

Pan, L.; Zhu, G. *Perovskite Materials - Synthesis, Characterisation, Properties, and Applications*; Intech, 2016.

Park, N.-G.; Grätzel, M.; Miyasaka, T. *Organic-Inorganic Halide Perovskite Photovoltaics*; Springer, 2016.

Patel, P. Hey, Chatbot, Can You Synthesize This Molecule? C&EN Global Enterprise **2024**, 102, 6, 18-20. DOI: 10.1021/cen-10206-feature1.

Pistoia, G. *Battery Operated Devices and Systems (Chapter-2)*; Elsevier, 2008.

Pradhan, S. N.; Pradhan, A.; Dash, B. P.; Sahoo, P. K.; Sahoo, N. K.; Naik, B. Artificial Photosynthesis Using Ultrathin 2D Materials. *Materials Today: Proceedings* **2022**. DOI: 10.1016/j.matpr.2022.06.445.

Qu, J.; Yang, T.; Zhang, P.; Yang, F.; Cai, Y.; Yang, X.; Li, C. M.; Hu, J. Artificial Photosynthesis Platform of 2D/2D MXene/Crystalline Covalent Organic Frameworks Heterostructure for Efficient Photoenzymatic CO2 Reduction. *Applied Catalysis B Environment and Energy* **2024**, *348*, 123827–123827. DOI: 10.1016/j.apcatb.2024.123827.

Rachadel, P. L.; Motuzas, J.; Machado, R. A.; Hotza, D.; Diniz, C. Influence of Porous Structures on O_2 Flux of BSCF Asymmetric Membranes. *Separation and Purification Technology* **2017**, *175*, 164–169. DOI:10.1016/j.seppur.2016.10.053.

Ramakrishnappa, T.; Sureshkumar, K.; Prakash, H. R.; Pandurangappa, M. Nickel Oxy Hydroxide Impregnated Glassy Carbon Spheres Composite Modified BPPG Electrode: Robust Electrochemical Interface for Sulfide Sensing. *Inorganic Chemistry Communications* **2024**, *164*, 112377–112377. DOI:10.1016/j.inoche. 2024.112377.

Reeve, C. *Practices of Reason*; Oxford University Press, USA, 1992.

Ren, D.; Shen, Y.; Yang, Y.; Shen, L.; Levin, B. D. A.; Yu, Y.; Muller, D. A.; Abruña, H. D. Systematic Optimization of Battery Materials: Key Parameter Optimization for the Scalable Synthesis of Uniform, High-Energy, and High Stability $LiNi_{0.6}Mn_{0.2}Co_{0.2}O_2$ Cathode Material for Lithium-Ion Batteries. *ACS Applied Materials & Interfaces* **2017**, *9* (41), 35811–35819. DOI: 10.1021/acsami7b10155.

Ren, J.; Zhu, H.; Fang, Y.; Li, W.; Lan, S.; Wei, S.; Yin, Z.; Tang, Y.; Ren, Y.; Liu, Q. Typical Cathode Materials for Lithium-Ion and Sodium-Ion Batteries: From Structural Design to Performance Optimization. **2023**, *2* (3), 339–377. DOI: 10.1002/cnl2.62.

Rodrigues, L.; Montez, C.; Moraes, R.; Portugal, P.; Vasques, F. A Temperature-Dependent Battery Model for Wireless Sensor Networks. *Sensors* **2017**, *17* (2), 422. DOI: 10.3390/s17020422.

Root, M. *The TAB Battery Book : An In-Depth Guide to Construction, Design, and Use*; New York Mcgraw Hill Professional, 2011.

Sahin, A.; Emirdag-Eanes, M. Crystal Structure of Lead(II) Trioxovanadate(v) Chloride, Pb[VO3]Cl. *Zeitschrift für Kristallographie - New Crystal Structures* **2007**, *222* (3), 159–160. DOI: 10.1524/ncrs.2007.0065.

Saikia, D.; Betal, A.; Bera, J.; Sahu, S. Progress and Challenges of Halide Perovskite-Based Solar Cell- a Brief Review. *Materials science in semiconductor processing* **2022**, *150*, 106953–106953. DOI: 10.1016/j.mssp.2022.106953.

Saleh, F. S.; Reid, O. O.; Bradley Easton, E. Determining Electrochemically Active Surface Area in PEM Fuel Cell Electrodes with Electrochemical Impedance Spectroscopy and Its Application to Catalyst Durability. *Electrochimica Acta* **2013**, *114*, 278–284. DOI: 10.1016/j.electacta.2013.10.050.

Sánchez, A.; Shalan, A. E.; Rosales, M.; Ruiz, I.; Javier, F. Screen-Printed Nickel Hydroxide Electrodes: Semiconducting, Electrocatalytic, and Electrochromic Properties. *Journal of Electroanalytical Chemistry* **2023**, *928*, 117052–117052. DOI: 10.1016/j.jelechem.2022.117052.

Sankir, N. D.; Sankir, M. *Photoelectrochemical Solar Cells*; John Wiley & Sons, 2018.

Schira, R.; Latouche, C. DFT and Hybrid-DFT Calculations on the Electronic Properties of Vanadate Materials: Theory Meets Experiments. *New Journal of Chemistry* **2020**, *44* (27), 11602–11607. DOI: 10.1039/d0nj02316g.

Scrosati, B. *Advances in lithium-ion batteries*. Springer. 2002.

Shangguan, E.; Zhang, H.; Wu, C.; Cai, X.; Wang, Z.; Wang, M.; Li, L.; Wang, G.; Li, Q.; Li, J. CoAl-Layered Double Hydroxide Nanosheets-Coated Spherical Nickel Hydroxide Cathode Materials with Enhanced High-Rate and Cycling Performance for Alkaline Nickel-Based Secondary Batteries. *Electrochimica Acta* **2020**, *330*, 135198. DOI: 10.1016/j.electacta.2019.135198.

Sharaf, O. Z.; Orhan, M. F. An Overview of Fuel Cell Technology: Fundamentals and Applications. *Renewable and Sustainable Energy Reviews* **2014**, *32*, 810–853. DOI: 10.1016/j.rser.2014.01.012.

Shen, P. K.; Wang, C.-Y.; Jiang, S. P.; Sun, X.; Zhang, J. *Electrochemical Energy*; CRC Press, 2018.

Shukla, A. K.; Venugopalan, S.; Hariprakash, B. Nickel-Based Rechargeable Batteries. *Journal of Power Sources* **2001**, *100* (1-2), 125–148. DOI:10.1016/s0378-7753 (01)00890-4.

Shutthanandan, V.; Nandasiri, M. I.; Zheng, J.; Engelhard, M. H.; Xu, W.; Thevuthasan, S.; Vijayakumar, M. Applications of XPS in the Characterization of Battery Materials. **2019**, *231*, 2–10. DOI: 10.1016/j.elspec.2018.05.005.

Singh, D. J. Electronic Structure and Bond Competition in the Polar MagnetPbVO3. *Physical Review B* **2006**, *73* (9). DOI: 10.1103/physrevb.73.094102.

Singh, P.; Dudeja, V.; Panwar, A. K. Electrochemical Performance of NCA Based Cathodes for Variable Thickness of Electrode through Modelling and Simulation. *Materials Today: Proceedings* **2022**, *62* 3742–3748. DOI:10.1016/j.matpr.202 2.04.446.

Snyder, C. *The effects of charge/discharge rate on capacity fade of lithium ion batteries*. Rensselaer Polytechnic Institute. 2016.

Srinivasan, V.; Weidner, J. W. Capacitance Studies of Cobalt Oxide Films Formed via Electrochemical Precipitation. *Journal of Power Sources* **2002**, *108* (1-2), 15–20. DOI: 10.1016/s0378-7753(01)01012-6.

Subhashini, P. V. C. K.; V. D. Rajesh, K. V. D. Doped BSCF Cathode Materials for Low-Temperature Solid Oxide Fuel Cell Applications-A Short Review. *Materials Today: Proceedings* **2022**, *78*, 520–523. DOI:10.1016/j.matpr.2022.11.212.

Suh-Cem, P.; Anderson, M. A.; Chapman, T. W. Novel Electrode Materials for Thin-Film Ultracapacitors: Comparison of Electrochemical Properties of Sol-Gel-Derived and Electrodeposited Manganese Dioxide. *Journal of The Electrochemical Society* **2000**, *147* (2), 444–444. DOI: 10.1149/1.1393216.

Sun, G.; Jia, S.; Shi, J.; Luo, Y.; Jiang, Z.; Yuan, X. Energy Storage Efficiency in Artificial Photosynthesis – an Evaluation Method in Engineering Perspective. *Energy Conversion and Management* **2023**, *292*, 117352. DOI:10.1016/j.encon man.2023.117352.

Sun, J.; Cao, X.; Zhou, H. Advanced Single-Crystal Layered Ni-Rich Cathode Materials for Next-Generation High-Energy-Density and Long-Life Li-Ion Batteries. *Physical Review Materials* **2022**, *6* (7). DOI: 10.1103/physrevmaterials.6.070201.

Şahin, A; İzmir Yüksek Teknoloji Enstitüsü. *Hydrothermal Synthesis and Characterization of Transition Metal Oxides*; 2004.

Tang, W.; Li, W.; Li, D.; Liu, G.; Wu, X.; Chen, Y. Synergistic Effects in Porous Mn–Co Mixed Oxide Nanorods Enhance Catalytic Deep Oxidation of Benzene. *Catalysis Letters* **2014**, *144* (11), 1900–1910. DOI: 10.1007/s10562-014-1340-3.

Tao, Y.; Jinfei, C.; Tingting, Y.; Zaijun, L. Template-Free Synthesis of α-Ni(OH) 2 Hollow Microspheres with Flower-like Morphology for High-Performance Supercapacitors. *Materials Research Bulletin* **2014**, *60*, 612–620. DOI: 10.1016/ j.materresbull.2014.09.031.

Tsais, P.-J. .; Chan, L. I. Nickel-Based Batteries: Materials and Chemistry. *Electricity*

Transmission, Distribution and Storage Systems **2013**, 309–397. DOI: 10.1533/9780857097378.3.309.

Tsipis, E. V.; Agarkov, D. A.; Borisov, Yu. A.; Kiseleva, S. V.; Tarasenko, A. B.; Bredikhin, S. I.; Kharton, V. V. Waste Gas Utilization Potential for Solid Oxide Fuel Cells: A Brief Review. *Renewable and Sustainable Energy Reviews* **2023**, *188*, 113880. DOI: 10.1016/j.rser.2023.113880.

Ul-Hamid, A. *A Beginners' Guide to Scanning Electron Microscopy*; Cham Springer International Publishing, 2018.

Van de Krol, R.; Grätzel, M. *Photoelectrochemical hydrogen production* (Vol. 90). New York: Springer. 2012.

Wang, J.; Cao, Z.; Zhu, X.; Yang, W. Improving Intermediate-Temperature Stability of BSCF by Constructing High Entropy Perovskites. *Journal of Membrane Science Letters* **2022**, *2* (2), 100026–100026. DOI: 10.1016/j.memlet.2022.100026.

Wang, J.; Zhu, Y.; Cao, Z.; Zhu, X.; Yang, W. Oxygen Transport Kinetics of BSCF-Based High Entropy Perovskite Membranes. *Separation and Purification Technology* **2023**, *309*, 123093–123093. DOI: 10.1016/j.seppur.2023.123093.

Wang, S-Y.; Wu, N-L. Operating Characteristics of Aqueous Magnetite Electrochemical Capacitors. *Journal of Applied Electrochemistry* **2003**, *33* (3/4), 345–348. DOI: 10.1023/a:1024193028297.

Wang, X. Y.; Yan, J.; Zhang, Y. S.; Yuan, H. T.; Song, D. Y. Cyclic Voltammetric Studies of Pasted Nickel Hydroxide Electrode Microencapsulated by Cobalt. *Journal of applied electrochemistry* **1998,** 28, 1377-1382.

Wang, Y.; Gai, S.; Li, C.; He, F.; Zhang, M.; Yan, Y.; Yang, P. Controlled Synthesis and Enhanced Supercapacitor Performance of Uniform Pompon-like β-Ni(OH)2 Hollow Microspheres. *Electrochimica Acta* **2013**, *90*, 673–681. DOI: 10.1016/j.electacta.2012.11.136.

Wang, Y.; Shi, J.; Gu, X.; Deutschmann, O.; Shi, Y.; Cai, N. Toward Mobility of Solid Oxide Fuel Cells. *Progress in Energy and Combustion Science* **2024**, *102*, 101141–101141. DOI: 10.1016/j.pecs.2023.101141.

Watt, J. P. Hashin-Shtrikman bounds on the effective elastic moduli of polycrystals with orthorhombic symmetry. *Journal of Applied Physics* **1979**, *50*(10), 6290-6295.

Winter, M.; Brodd, R. J. What Are Batteries, Fuel Cells, and Supercapacitors? *Chemical Reviews* **2004**, *104* (10), 4245–4270. DOI: 10.1021/cr020730k.

Woodhouse, M.; Parkinson, B. A. Combinatorial Approaches for the Identification and Optimization of Oxide Semiconductors for Efficient Solar Photoelectrolysis. *Chemical Society Reviews* **2009**, *38* (1), 197–210. DOI: 10.1039/b719545c.

Wu, J.; Cao, J.; Han, W.-Q.; Janotti, A.; Kim, H.-C. *Functional Metal Oxide Nanostructures*; Springer Science & Business Media, 2011.

Wu, Y. *Lithium-Ion Batteries*; CRC Press, 2015.

Xiang, C.; Suram, S. K.; Haber, J. A.; Guevarra, D. W.; Soedarmadji, E.; Jin, J.; Gregoire, J. M. High-Throughput Bubble Screening Method for Combinatorial Discovery of Electrocatalysts for Water Splitting. *ACS Combinatorial Science* **2014**, *16* (2), 47–52. DOI: 10.1021/co400151h.

Xu, H.-B.; Zhang, Y.; Li, Z.-H.; Zheng, S.-L.; Wang, Z.-K.; Qi, T.; Li, H.-Q. Development of a New Cleaner Production Process for Producing Chromic Oxide from Chromite Ore. *Journal of Cleaner Production* **2006**, *14* (2), 211–219. DOI: 10.1016/j.jclepro.2004.09.001.

Yacobi, B. G. *Semiconductor Materials: An Introduction to Basic Principles*. Springer Science & Business Media. 2003.

Yang, C.; Zhu, Q.; Sadakane, M.; Zhang, Z.; Li, Y.; Ueda, W. Vanadium-Enhanced Intramolecular Redox Property of a Transition-Metal Oxide Molecular Wire. *Inorganic*.*Chemistry*.**2020**,.*59*.(22),.16557–16566. DOI: 10.1021/acs.Inorgchem .0c02485.

Yang, X.; Wang, Z.; Li, G.; Zhou, Y.; Sun, C.; Bi, L. Sc-Doped Ba0.5Sr0.5Co0.8Fe0.2O3-δ Cathodes for Protonic Ceramic Fuel Cells. *Ceramics International*. **2024**. DOI: 10.1016/j.ceramint.2024.03.085

Yesuraj, J.; Ramesh, M.; Kim, K.; Biswas, K. Fundamental Aspects of Perovskite Oxides as an Emerging Material for Supercapacitor Applications and Its Anion Intercalation Mechanism - Review. *Journal of Energy Storage* **2024**, *78*, 109968–109968. DOI: 10.1016/j.est.2023.109968.

Younas, M.; Aziz; Khan, K.; Nabi, I.; Ullah, Z.; Humayun, M.; Hou, J. Application of Manganese Oxide-Based Materials for Arsenic Removal: A Review. *Science of the total environment* **2024**, *918*, 170269–170269. DOI:10.1016/j.scitotenv.202 4.170269.

Yusoff, F.; Aziz, A.; Mohamed, N.; Ab Ghani, S. Synthesis and Characterizations of BSCF at Different PH as Future Cathode Materials for Fuel Cell. *International Journal of Electrochemical Science* **2013**, *8* (8), 10672–10687. DOI: 10.1016/s1452-3981(23)13139-7.

Zhang, B.; Sun, L. Artificial Photosynthesis: Opportunities and Challenges of Molecular Catalysts. *Chemical Society Reviews* **2019**, *48* (7), 2216–2264. DOI: 10.1039/c8cs00897c.

Zhang, J.; Ding, Y.; Shi, H.; Shao, P.; Yuan, X.; Hu, X.; Zhang, Q.; Zhang, H.; Luo, D.; Wang, C.; Yang, L.; Luo, X. Selective Recycling of Lithium from Spent LiNixCoyMn1-x-YO2 Cathode via Constructing a Synergistic Leaching Environment. *Journal of environmental management* **2024**, *352*, 120021–120021.

DOI: 10.1016/j.jenvman.2024.120021.

Zhang, J.; Lei, Z.; Wang, J.; Yanna NuLi; Yang, J. Surface Modification of $Li_{1.2}Ni_{0.13}Mn_{0.54}Co_{0.13}O_2$ by Hydrazine Vapor as Cathode Material for Lithium-Ion Batteries. *ACS Applied Materials & Interfaces* **2015**, *7* (29), 15821–15829. DOI: 10.1021/acsami.5b02937.

Zhang, Y.; Qin, Z.; Wang, G.; Zhu, H.; Dong, M.; Li, S.; Wu, Z.; Li, Z.; Wu, Z.; Zhang, J.; Hu, T.; Fan, W.; Wang, J. Catalytic Performance of MnOx–NiO Composite Oxide in Lean Methane Combustion at Low Temperature. *Applied Catalysis B: Environmental* **2013**, *129*, 172–181. DOI: 10.1016/j.apcatb.2012.09.021.

Zhao, X.; Karakaya, C.; Qian, M.; Zou, R.; Zhang, W.; Lu, Z.; Maiti, D.; Samanta, A.; Wan, W.; Liu, X.; Tiplea, A.; Li, Y.; Cui, S.; Wang, C.; Lei, H.; Bankston, S.; Yilmaz, S.; Chen, J. G.; Ozcan, S. 3D Printing Synthesis of Catalysts. *Materials today sustainability* **2024**, *26*, 100746–100746. DOI: 10.1016/j.mtsust.2024.100746.

Zhou, G.; Tian, H.; Jin, Y.; Tao, X.; Liu, B.; Zhang, R.; Seh, Z. W.; Zhuo, D.; Liu, Y.; Sun, J.; Zhao, J.; Zu, C.; Wu, D. S.; Zhang, Q.; Cui, Y. Catalytic Oxidation of Li_2S on the Surface of Metal Sulfides for Li−S Batteries. *Proceedings of the National Academy of Sciences* **2017**, *114* (5), 840–845. DOI: 10.1073/pnas.1615837114.

Zhu, C.; Chen, Z.; Gong, W.; Li, H.; Liu, X.; Gan, X.; Yang, G.; Di, J.; Cui, Y. Direct Detection of Self-Reconstruction-Accelerated Oxygen Evolution Activity in MoCoNi Hydroxides. *Applied Surface Science* **2022**, *605*, 154669–154669. DOI: 10.1016/j.apsusc.2022.154669.

Zimmerman, A. H. *Nickel-Hydrogen Batteries : Principles and Practice*; Aerospace Press ; Reston, Va: El Segundo, Calif., 2009.

Zybert, M.; Ronduda, H.; Ostrowski, A.; Sobczak, K.; Dariusz Moszyński; Wioletta Raróg-Pilecka; Bartosz Hamankiewicz; Wieczorek, W. Structural Analysis and Electrochemical Investigation of Dual-Doped NMC622 Cathode Material: Effect of Sodium and Neodymium on the Performance in Li-Ion Batteries. *Energy Reports* **2023**, *10*, 1238–1248. DOI: 10.1016/j.egyr.2023.07.061.

CURRICULUM VITAE
(CV)

He graduated from the University of Sakarya with the highest-ranked student BSc from the chemistry department. He started his master's degree at the University of Sakarya. Then, he was accepted as a research assistant at İzmir Institute of Technology in 2017, and also he continues his doctorate studies at the same institute. He published four articles: two papers during his master term and two during his PhD.

Experience

Research Asistant at Izmir Instittute of Technology (2017 - …)
Turkish Armed Forces (TAF, TSK) 2014-2015: Analyst of Food and Control Laboratory Education Center : Teacher (2012-2013).
Researcher at Ni-Cat Battery INC (2020-….)

Publishes

1. https://doi.org/10.1016/j.ssc.2024.115645
2. https://doi.org/10.1007/s10800-020-01457-6
3. https://doi.org/10.1016/j.jlumin.2016.05.011
4. https://doi.org/10.1016/j.poly.2014.10.014